Université Mohamed Boudiaf - M'sila

FACULTE DE TECHNOLOGIE

DEPARTEMENT DE GENIE ELECTRIQUE

Numéro de série :……..

Numéro d'inscription :……

Thèse

Présentée pour l'obtention du diplôme de :

MASTER

Spécialité : Commande Electrique

THEME :

Super Twisting Sliding Mode Control for PV-Battery Integrated DC Microgrids

Proposé et dirigé par :

Dr. Ghadbane Houssam Eddine

Pr. CHEBABHI Ali

Présenté par :

Fenniche Abdennour

Soutenu le : /06/2025

Devant le jury composé de :

Pr. Barkat Said	Université Mohamed Boudiaf de M'sila	Président
Dr. Ghadbane Houssam Eddine	Université Mohamed Boudiaf de M'sila	Rapporteur
Pr. CHEBABHI Ali	Université Mohamed Boudiaf de M'sila	Co-Rapporteur
Dr. Djeriou Salim	Université Mohamed Boudiaf de M'sila	Examinateur

Année Universitaire : 2024 / 2025

Regards and gratitude:

First and foremost, we are grateful to God for guiding and allowing us to finish this study.

Firstly, I would like to express my gratitude to my supervisors,Dr. Ghadbane Houssem Eddine and Pr. Chebabhi Ali, for their invaluable support and guidance throughout this work, for his tremendous efforts and valuable time, and for his ongoing consultations that allowed me to fully comprehend the thesis topic.

We appreciate the discussion committee members' willingness to read, consider, and respond to this letter. We also want to express our profound gratitude to everyone who assisted, supported, and encouraged me whether it was in words or deeds, or even just by smiling and who motivated me to finish this work. Additionally, I want to sincerely thank my parents for their unwavering support and encouragement from the start of my academic journey to the present.

Abstract

This research addresses the control of a battrey energy storage system integrated with a photovoltaic (PV) source within a DC microgrid, focusing on voltage stabilization and disturbance rejection. Accurate modeling of both the PV generator and battery system was conducted, laying the groundwork for control design and system analysis.

A conventional Proportional-Integral (PI) controller was implemented as a baseline. While it performed adequately under steady conditions, it lacked robustness during transient disturbances and rapid system changes. To overcome these limitations, a Super-Twisting Sliding Mode Control (ST-SMC) strategy was introduced, known for its fast convergence and reduced chattering effects.

The comparative analysis revealed that the super-twisting control significantly improved voltage regulation and system resilience against disturbances and load variations. The hybrid storage system, under this advanced controller, exhibited superior dynamic response and operational stability.

In conclusion, the study emphasizes the necessity of combining accurate system modeling with robust control techniques for reliable renewable energy integration. Future work could focus on real-time implementation, hardware-in-the-loop testing, and the inclusion of additional renewable sources such as wind energy or supercapacitors.

Keywords: Photovoltaic source (PV); Battrey energy storage system; DC microgrid; Super-Twisting Sliding Mode Control (ST-SMC); Disturbance rejection, voltage stability, power balance, roubustness to system uncertainties.

يتناول هذا البحث موضوع التحكم في نظام تخزين طاقة هجين يعتمد على الطاقة الشمسية ومتكامل ضمن شبكة كهربائية مصغرة بالتيار المستمر (DC microgrid)، مع التركيز على تحقيق استقرار الجهد ورفض الاضطرابات. تم نمذجة نظام الخلايا الكهروضوئية (PV) ونظام البطاريات بدقة، مما شكّل الأساس لتطوير استراتيجيات التحكم.

تم استخدام متحكم تقليدي من نوع Proportional-Integral (PI) كمرجع أولي للأداء، وقد أظهر كفاءة مقبولة في ظروف التشغيل المستقرة، لكنه فشل في التعامل مع الاضطرابات السريعة والتغيرات المفاجئة. للتغلب على هذه القيود، تم اقتراح تقنية التحكم بالانزلاق من الدرجة الثانية (Super-Twisting Sliding Mode Control)، المعروفة بقدرتها على تحقيق الاستقرار بسرعة .

أظهرت نتائج المقارنة بين الطريقتين أن التحكم الفائق الالتواء يوفر أداءً متفوقًا من حيث تنظيم الجهد واستجابة النظام للاضطرابات، مما يساهم في تعزيز موثوقية وكفاءة الشبكة المصغرة. تؤكد نتائج البحث أهمية استخدام تقنيات تحكم متقدمة لضمان التكامل الفعّال لمصادر الطاقة المتجددة في الأنظمة اللامركزية. ويُقترح في الأعمال المستقبلية تجربة التنفيذ العملي في الوقت الحقيقي، وتوسيع الدراسة لتشمل مصادر طاقة متجددة إضافية.

الكلمات المفتاحية:

المصدر الكهروضوئي(PV) ؛ نظام تخزين الطاقة بالبطاريات؛ الشبكة الكهربائية المستقلة ذات التيار المستمر (DC Microgrid)؛ التحكم الانزلاقي بطريقة السوبر تويستينغ(ST-SMC) ؛ رفض الاضطرابات؛ استقرار الجهد؛ توازن القدرة؛ المتانة ضد عدم اليقين في النظام.

General Introduction:

The transition to sustainable energy solutions has become a central objective in the development of modern electrical power systems. Driven by growing environmental concerns, dwindling fossil fuel reserves, and international policy commitments to reduce greenhouse gas emissions, renewable energy sources are increasingly integrated into national and local energy infrastructures. Among these, solar photovoltaic (PV) systems are one of the most promising technologies, primarily due to their inexhaustible nature, scalability, and minimal environmental impact during operation. However, the widespread deployment of PV systems presents various technical challenges, particularly when integrated into decentralized and autonomous power networks, such as DC microgrids [1].

DC microgrids have gained traction as a viable architecture for decentralized energy systems, particularly in areas with unreliable grid access or in remote locations. Compared to AC microgrids, DC systems offer numerous advantages, including higher efficiency due to the elimination of synchronization requirements and reactive power losses, better compatibility with renewable energy sources and modern DC loads (e.g., LED lighting, electric vehicles, and power electronics), and simplified control mechanisms. Moreover, the reduced need for complex power conversion stages enables more straightforward system integration and reduced overall energy losses. Nonetheless, the benefits of DC microgrids are offset by new challenges, primarily stemming from the intermittent and variable nature of renewable energy sources like solar PV [2].

Solar PV generation is highly dependent on environmental conditions, including solar irradiance and ambient temperature, both of which are subject to rapid fluctuations. As a result, PV systems often produce power that is not perfectly matched with instantaneous load demands, leading to voltage instability, power imbalance, and reduced power quality in the microgrid. These issues are particularly pronounced during transient load events, sudden changes in irradiance (e.g., due to cloud coverage),

or grid faults. The inherently unsteady nature of solar energy necessitates the use of complementary technologies to ensure system reliability and consistent power delivery.

One promising solution to this problem is the incorporation of hybrid energy storage systems (HESS). These systems typically combine batteries with supercapacitors or other storage technologies to provide both energy and power balancing capabilities. Batteries are well-suited for longer-duration energy storage and load shifting, while supercapacitors or other fast-response storage devices can address short-term transients and rapid fluctuations. Together, they enhance the dynamic response of the system, reduce stress on the PV generation unit, and contribute to maintaining voltage stability. By acting as buffers between supply and demand, HESS units play a pivotal role in ensuring the reliability, resilience, and operational efficiency of DC microgrids.

However, the effective integration of PV systems and hybrid storage units depends critically on the control strategies employed. The primary goal of these control mechanisms is to manage the energy flow between the PV generator, the energy storage units, and the loads, while ensuring voltage regulation, load balancing, and system stability under various operating conditions. Traditional Proportional-Integral (PI) controllers remain popular due to their ease of implementation and acceptable performance in systems with relatively predictable and linear behavior. PI controllers are often employed in industrial settings because of their simplicity, well-understood tuning procedures, and minimal computational burden.

Despite these advantages, PI controllers exhibit limitations in complex and dynamically changing systems. Their performance deteriorates under significant disturbances or in the presence of system nonlinearities, time-varying parameters, and model uncertainties. They often struggle to maintain tight control over system variables during rapid transients or abrupt changes in load demand or generation. As the complexity and variability of modern power systems increase, there is a growing need for more advanced control methodologies capable of ensuring robustness, fast transient response, and enhanced disturbance rejection [3].

To address these limitations, nonlinear and robust control strategies have been proposed and investigated in recent years. Among these, sliding mode control (SMC)

and its higher-order variants, such as super-twisting control, have attracted significant interest. These methods offer several advantages, including strong robustness against system uncertainties, fast convergence to desired states, and effective handling of nonlinearities. In particular, the super-twisting sliding mode controller is a second-order method that alleviates the chattering phenomenon typical of classical SMC while preserving its desirable robustness and finite-time convergence properties. Its application in power electronics and energy systems has demonstrated promising results in improving voltage regulation and disturbance rejection performance.

This research aims to investigate and compare two control strategies—PI control and super-twisting sliding mode control—applied to a PV-battery-based DC microgrid system. The study is structured as follows: Chapter 1 focuses on the mathematical modeling of the PV generator, including its electrical characteristics and dynamic behavior under varying irradiance conditions. Chapter 2 presents the model of the battery storage system, capturing its charging and discharging dynamics, state-of-charge constraints, and interface with the DC bus. In Chapter 3, a conventional PI controller is designed and implemented to regulate the DC bus voltage and manage power flows. Chapter 4 introduces the design and application of the super-twisting sliding mode controller, emphasizing its enhanced performance under disturbance conditions and system uncertainties.

The main objective of this study is to assess the effectiveness of each control strategy in maintaining voltage stability and rejecting disturbances in the DC microgrid. By conducting comparative simulations and performance evaluations under varying operating conditions, this research contributes to identifying the most suitable control technique for enhancing the reliability, robustness, and efficiency of PV-based decentralized energy systems. The insights gained from this work are expected to support the development of resilient and intelligent control architectures for next-generation DC microgrids that increasingly rely on renewable and distributed energy resources.

Chapter I

Modeling of a photovoltaic generator

I.1. Introduction:

Helielectricity, which deals with the direct transformation of solar energy into electrical energy, appeared in 1930 with cuprous oxide cells and then selenium, but it was only from 1954, with the realization of the first selenium photoelectric cells in the laboratories of the Bell Telephone Company, that we foresee the possibility of supplying energy. Very quickly used to power space vehicles, their development and rapid progress were motivated by the conquest of space. But, for both technical and economic reasons, this new source of electrical energy has been slow to establish itself outside the space field.

However, during the 80s, terrestrial photovoltaic technology progressed steadily through the installation of several power plants of a few megawatts, and even became familiar to consumers through many low-power products using it: watches, calculators, radio and weather beacons, pumps and solar refrigerators [4].

Currently, the power value of a photovoltaic module is from a few Watt peaks to a few tens of Watt peaks. To obtain higher powers, it is necessary to associate in series and / or in parallel several modules thus forming the photovoltaic generator.

This chapter will be devoted in its first part to the general principles of photovoltaic conversion, photovoltaic cells, modules and generators photovoltaics. The second part will be dedicated to the mathematical modeling of the solar source which seems an essential step. The influence of radiation, temperature and contact resistance on the performance of the photovoltaic module are also considered.

I.1.2. Sun and radiation

I.1.2.1. Sun

The sun produces a huge amount of energy, which leaves its surface in the form of electromagnetic radiation with a spectrum ranging from 0.25 m (ultraviolet) to 40 m (infrared). This energy represents a major source of energy in the future. Despite the considerable distance of the earth from the sun (150,106 km), the Earth's layer receives an amount of energy of 180,106 GW.

I.1.2.2. Radiation

The sun radiates a power of 16.1015 kWh per year on the earth, in all wavelengths of the visible light spectrum. Light energy from the sun is the basis of most of the available forms of energy: chemical, thermal, hydraulic, electrical energies. For example, fossil fuels, such as coal, natural gas and oil, were formed as a result of storage of solar energy by organisms, over a long period of time. In fact, nuclear energy is the only one that does not come from solar energy.

The latter is essential to maintain the light and thermal conditions necessary for life on Earth. For example, photosynthesis uses this energy to provide chlorophyll plants with organic matter. Sixty percent of the solar energy that reaches the earth is reflected by the atmosphere; 11% is reflected by the soil and vegetation; 16% maintains, by evaporation, the water cycle, which produces rain, mountain and river water [5].

I.2. General information about semiconductors :

I.2.1. Constitution of a PN diode :

When an N-type doped semiconductor material (electron-rich) is brought into intimate contact with another P-type doped semiconductor material (electron-poor), the PN junction between the two media will be the site of an upheaval. In this narrow zone, the excess electrons in the N part diffuse into the P part. Thus, in the N zone, a positively charged region is created near the junction (where electrons are missing).

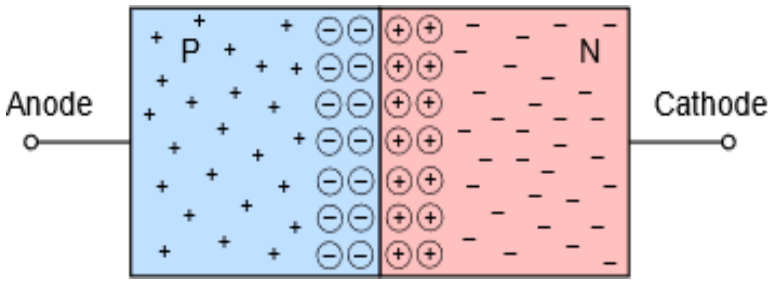

Fig. I.1 :*Creation of the transition zone in a PN junction .*

Symmetrically in the P zone, a negatively charged region is created (where there is an excess of electrons) (Fig. I.1). At equilibrium, between these two positively and negatively charged zones (depletion zone: space charge zone), an electric field directed from the P region to the N region has therefore been created and a potential difference VD appears. This electric field is fundamental for the operation of solar cells.

I.2.2. I-V characteristic of the PN diode:

The mobile electrons in the semiconductor can come either from the N region (majority carriers) or from the P region (minority carriers). The behavior of these two types of carriers can be demonstrated by applying a variable DC voltage V to the terminals of the diode (in the dark) and by closing the circuit on a resistor.

If this additional voltage V is positive, the potential difference between the N and P zones is reduced and the majority charge carriers will be able more easily

cross the space charge zone thus giving rise to a current I d directed from the region P to the N region, intense because due to the majorities. This current Id increases with the temperature of the junction and with the applied voltage V. If this additional voltage V is negative, the potential difference between the N and P zones is increased and only the minority charge carriers will be able to cross the zone of space charge giving rise to a current I 0 directed from the N region to the P region, low because due to the minorities. This current I 0 increases with the temperature of the junction.

At too high negative values of the applied voltage, V the junction snaps by avalanche effect and it is destroyed.

I.2.3. Light absorption

In a semiconductor material, for an electron bound to its atom and participating in chemical bonds (valence band), to become free and mobile (conduction band) in a possible electric field, it is necessary, among other conditions, to transfer a minimum energy to it, for example by absorption of photons or by raising the temperature. All the photons of the solar spectrum can be absorbed by the electrons, but not all of them give rise to a promotion of electrons towards the conduction band.

In the case of silicon, only photons with a wavelength of less than 1.1 µm can be usefully absorbed, the others only give rise to an increase in temperature.

I.2.4. Electron-hole pairs

Only the electron-hole pairs generated near the depletion zone or within it will be able to be separated by the intense electric field that prevails there and produce an electric current that must be collected by making the front and rear contacts (Fig. I.2).

This photovoltaic current is directly proportional to the intensity of the illumination and is directed from the N region to the P region, it is denoted I ph [6].

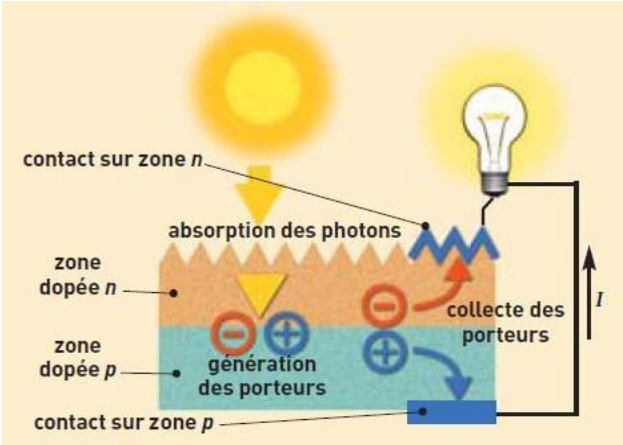

***Fig.I.2**: Absorption of light and transfer of energy from photons to electrons.*

I.3. Photovoltaic cells:

To obtain a photovoltaic cell, it is necessary to produce a diode structure, that is to say to produce a P-N type junction in a silicon material doped in volume with an element such as boron which makes it positive (P zone) and counter-doped in a zone

surface with phosphorus which makes it negative (N zone). The electric field which prevails at the junction of these two differently doped zones separates the electric charges photo-generated by sunlight (electron-hole pairs) and ensures their evacuation from the crystal (the electrons by the cathode and the holes by the anode) under a voltage of the order of 0.5 V and a direct current of the order of 30 mA for each cm 2 of sensor under a maximum sunshine of 1 kW/ m 2.

Then the structure of a solar cell is similar to that of a P-N junction, the current under darkness in such a structure is given by the formula :

$$I_d(V) = I_0(e^{\frac{qV}{nKT}} - 1) \quad \text{(I.1)}$$

Where :

q: The charge of the electron ($q = 1.6\times10^{-19}C$).

k: Boltzmann's constant ($k = 1.381\times10^{23}J/K$).

T: The effective temperature of the cell in kelvin.

I_0: The reverse saturation current of the P-N junction. It has two components :

- the diffusion current of the minority carriers, constituted by the electrons of the P region and the holes of the N region which manage to reach the space charge zone by diffusion ;

- the thermal generation current due to the electron-hole pairs created thermally in the space charge zone.

The factor n, between 1 and 2, representing the coefficient of ideality of the P-N junction, makes it possible to take into account the different components of the direct current circulating in the P-N junction :

- the components due to the recombinations in the N and P regions constitute the currents of the diffusion of the electrons and the holes (n=1) ;

- the component due to the recombinations in the space charge zone constitutes the recombination current of the junction (n=2).

I. 3.1. Principle of operation of a photovoltaic cell:

Under illumination, the electron-hole pairs photo-generated in the space charge zone (ZCE) are instantaneously separated by the electric field prevailing there (Fig. I.3). The positive charge holes are accelerated towards the P zone, the negative charge electrons towards the N zone. Holes and electrons then become the majority: this is the generation photocurrent. In parallel, the minority carriers, holes generated on the N side and electrons generated on the P side, create a concentration gradient and diffuse into the material. If they reach the ECZ without recombining, the electric field makes them cross the depletion zone in order to reach the region where they become the majority: this is the diffusion photocurrent. The presence of ohmic contact ensures the collection of the carriers hence the creation of a photogenated current I ph [7][8].

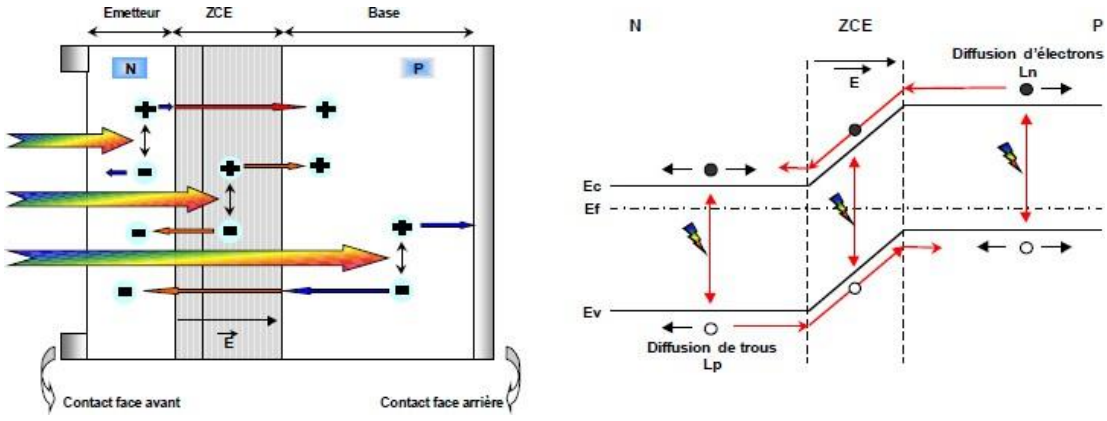

***Fig.I.3**: Structure and diagram of the bands of a photovoltaic cell under illumination.*

I.3.2. Different types of photovoltaic cells:

There are different types of solar cells (or photovoltaic cells), and each type of cell has its own efficiency and cost. However, whatever their type, their efficiency remains quite low: from 8 to 23% of the energy they receive. The main types of cells currently in use are [5]:

- Monocrystalline cells: these are the ones with the best yield (12- 16%; up to 23% in the laboratory), but also the ones with the highest impact, due to complicated manufacturing ;

- Polycrystalline cells: their design being easier, their manufacturing cost is less important, however their yield is lower: 11% - 13% (18% in the laboratory) ;

- Amorphous cells: they have a low yield (8% - 10%; 13% in the laboratory), but require only very small thicknesses of silicon and have a low cost. They are commonly used in small consumer products such as solar calculators or watches.

I.4. Model of a photovoltaic cell:

A solar cell is represented in the literature by several models, each of them is governed by a mathematical expression between the current and the voltage according to the technological parameters of the cell.

I.4.1. Single-diode model:

It is possible to combine the diode d_{1_cell} and the diode d_{2_cell} of the two-diode model in a single d_{cell} diode. By taking the coefficient of ideality n between n1 and n2 we obtain the one-diode model of Fig.I.5. [9].

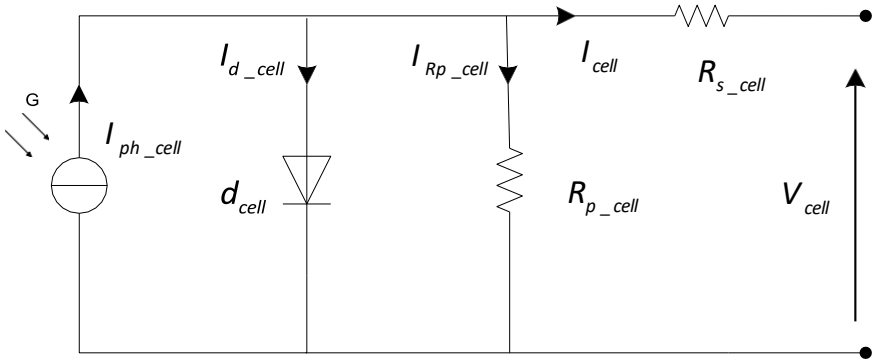

***Fig.I.4**: Equivalent circuit of the model to a diode of a photovoltaic cell.*

By the application of the law of nodes we find :

$$I_{cell} = I_{ph\_cell} - I_{d\_cell} - I_{Rp\_cell} \quad \text{(I.2)}$$

With :

$$I_{d\_cell} = I_0 \left(e^{\frac{V_{cell} + R_{s\_cell} I_{cell}}{nKT/q}} - 1 \right) \quad \text{(I.3)}$$

Where :

I_0: The reverse saturation current of the diode d_{cell} .

So the current of the cell is given by the following equation :

$$I_{cell} = I_{ph\_cell} - I_0\left(e^{\frac{V_{cell}+R_{s\_cell}I_{cell}}{nKT/q}} - 1\right) - \frac{V_{cell}+R_{s\_cell}I_{cell}}{R_{p\_cell}} \quad \text{(I.4)}$$

I.4.2. Two-diode model :

The equivalent circuit of the two-diode model is given in Fig.I.5. This model is the closest to the real behavior of the solar cell, because it takes into account the mechanism of transport of electric charges inside the cell (two diodes). The two-diode model is composed of two exponentials. The first takes into account the diffusion phenomenon, while the second exponential corresponds to the recombination phenomenon, in the depletion region [9][10].

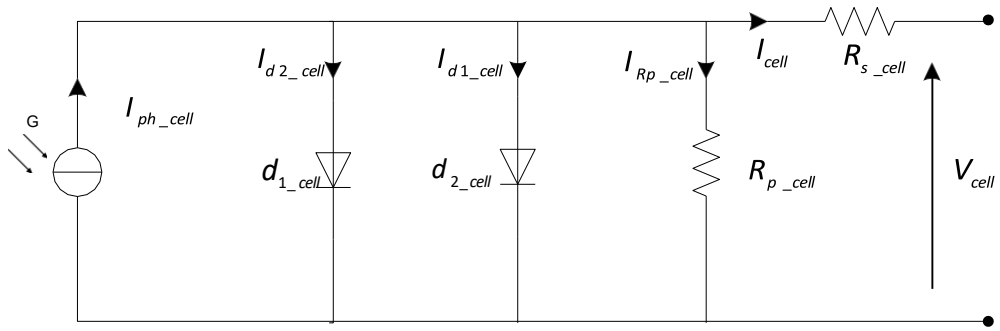

***Fig.I.5**: Equivalent circuit of the two-diode model of a photovoltaic cell.*

Current generator:

It delivers the current I_{ph_cell} corresponding to the photogenerated current in the cell.

series resistor R_{s_cell}

It takes into account the resistivity specific to the contacts between the different constituent regions of the cell, namely the emitter, the base and the metal contacts.

Parallel resistance R_{p_cell}

Also known as short-circuit resistance. It translates the existence of shunts through the transmitter.

Diode d_{1_cell}

Models the diffusion of the carriers in the base and the emitter. Its influence will be all the greater the longer the diffusion length of the material.

Diode d_{2_cell}

Models the generation/recombination of the carriers in the space charge zone [8].

By applying the laws of the nodes to the cell shown in Fig.I.5. we can describe the mathematical model of the photovoltaic cell.

The current supplied to a cell is given by :

$$I_{cell} = I_{ph\_cell} - I_{d1\_cell} - I_{d2\_cell} - I_{Rp\_cell} \quad \text{(I.5)}$$

With :

$$\begin{cases} I_{d1_{-cell}} = I_{01}\left(e^{\frac{V_{cell}+R_{s_{-cell}}I_{cell}}{n_1 kT/q}} - 1\right) \\ I_{d2_{-cell}} = I_{02}\left(e^{\frac{V_{cell}+R_{s_{-cell}}I_{cell}}{n_2 kT/q}} - 1\right) \\ I_{R_{p_{-cell}}} = \frac{V_{cell}+R_{s_{-cell}}I_{cell}}{R_{p_{-cell}}} \end{cases} \quad \text{(I.6)}$$

The current within the photovoltaic cell is therefore modalized by the following relationship :

$$I_{cell} = I_{ph\_cell} - I_{01}\left(e^{\frac{V_{cell}+R_{s_{-cell}}I_{cell}}{\frac{n_1 kT}{q}}} - 1\right) - I_{02}\left(e^{\frac{V_{cell}+R_{s_{-cell}}I_{cell}}{\frac{n_2 kT}{q}}} - 1\right) - \frac{V_{cell}+R_{s_{-cell}}I_{cell}}{R_{p_{-cell}}} \quad \text{(I.7)}$$

With :

I_{cell}: The current supplied by the cell.

I_{01}: The reverse saturation current of the diode d_{1_cell} .

I_{02}: The reverse saturation current of the diode d_{2_cell} .

q: The electron charge ($q = 1.6\times10^{-19}C$).

k: Boltzmann's constant ($k = 1.381\times10^{23}J/K$).

n1= 1 and n2= 2: The coefficients of ideality of the PN junction.

T: The effective temperature of the cell in kelvin.

I.4.3. Model with ohmic losses :

I.4.3.1 Current model :

If we assume that the parallel resistance is infinite ($R_p = \infty$) , we obtain the model with ohmic losses of Fig. I.6. This model is usually the most used in the design but in case a very high precision is required the model with two diodes in parallel is often used [10].

In this case the cell current is given by the following equation :

$$I_{cell} = I_{ph\_cell} - I_0 \left(e^{\frac{V_{cell} + R_{s\_cell} I_{cell}}{nKT/q}} - 1 \right) \quad \text{(I.8)}$$

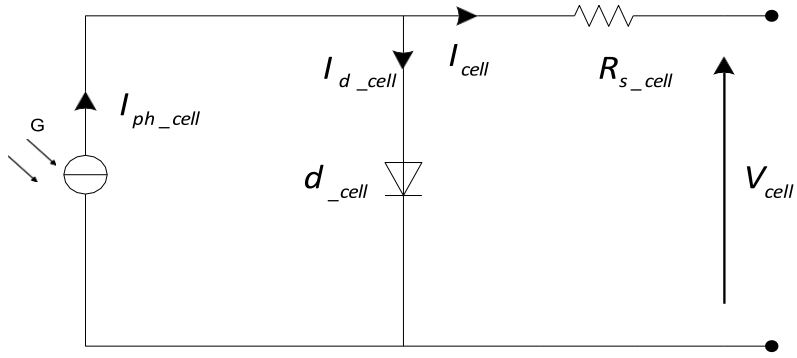

Fig.I.6: *Equivalent circuit of the model with ohmic losses of a photovoltaic cell.*

I.4.3.2 Voltage model:

The voltage model of the cell shown in Fig.I.6. can be deduced from equation (I.8), which results :

$$V_{cell} = \frac{nKT}{q} ln \left(\frac{I_{ph_{cell}} - I_{cell} + I_0}{I_0} \right) - R_{s_{cell}} I_{cell} \quad \text{(I.9)}$$

1.5.Calculation of the current of a cell under the temperature reference conditions T_{ref} and irradiation G_0 :

1.5.1. Calculation of the saturation current at T_{ref} :

The reverse saturation current of the diode is calculated in the point where the current of the cell is equal to zero ($I_{cell} = 0$) while the no-load voltage of the cell (V_{oc_cell}) is equal to the open circuit voltage of the module given by the manufacturer (V_{oc_module}) divided by the number of cells in series (N_s) so :

$$\begin{cases} V_{cell} = V_{oc\_cell} = \frac{V_{oc\_module}}{N_s} \\ I_{ph\_cell} = I_{sc\_cell} \mid_{T_{ref}} \end{cases} \quad \text{(I.10)}$$

Where $I_{sc\_module}|_T$ represent the short circuit current of the module given by the manufacturer. The saturation current at T_{ref} is expressed from (I.8) and (I.10) by :

$$I_0|_{T_{ref}} = \frac{I_{sc\_cell}|_{T_{ref}}}{\left(e^{\frac{V_{oc\_cell}}{nKT_{ref}/q}} - 1\right)} \quad (I.11)$$

1.5.2. Calculation of the series resistance to T_{ref} :

The series resistance of the cell is calculated in the point where ($V_{cell} = V_{oc\_cell} = \frac{V_{oc\_module}}{N_s}$) by evaluating the slope of the I-V curve in the point V_{oc_module} . By differentiating the equation (I.8) and then rearranging it in terms of R_{s_cell} [9] [11].

The differentiation of the equation (I.8), gives :

$$dI_{cell} = 0 - I_0|_{T_{ref}} \frac{dV_{cell} + R_{s\_cell} dI_{cell}}{nKT_{ref}/q} \left(e^{\frac{V_{cell} + R_{s\_cell} I_{cell}}{nKT_{ref}/q}}\right) \quad (I.12)$$

So from equation (I.12), the series resistance is written as :

$$R_{s\_cell} = \frac{nKT_{ref}/q}{\left(e^{\frac{V_{cell} + R_{s\_cell} I_{cell}}{nKT_{ref}/q}}\right)} - \frac{dV_{cell}}{dI_{cell}} \quad (I.13)$$

Then, by evaluating the equation (I.13) in an open circuit defined by: $V_{cell} = V_{oc\_cell}$ and $I_{cell} = 0$ we find:

$$R_{s\_cell} = \frac{nKT_{ref}/q}{\left(e^{\frac{V_{oc\_cell}}{nKT_{ref}/q}}\right) I_0|_{T_{ref}}} - \frac{dV_{cell}}{dI_{cell}}|_{V_{oc\_cell}} \quad (I.14)$$

Where $\frac{dV_{cell}}{dI_{cell}}|_{V_{oc\_cell}}$ is the slope of the I-V curve in the point $V_{cell} = V_{oc\_cell}$ (calculate from the I-V curve in the module data sheet (datasheet) then divide by the number of cells in series).

$\frac{dV_{cell}}{dI_{cell}}|_{V_{oc\_cell}} = \frac{\frac{dV_{module}}{dI_{module}}|_{V_{module}}}{N_s}$ and the value $\frac{dV_{module}}{dI_{module}}|_{V_{module}}$ is given by the manufacturer.

I.6. Calculation of the current of a cell at a temperature T **and an irradiation** G **Some :**

The previous equations are valid only for an optimal operating mode. To generalize our modeling for different illuminations and temperatures, we use the model that moves the reference curve to new locations.

I.6.1. Calculation of the short-circuit current at any temperature and irradiation:

- The variation of the short-circuit current of a cell as a function of the temperature is given by [11] [12] [13] [14]:

$$I_{sc\_cell}|_T = I_{sc\_cell}|_{T_{ref}}\left[1 + a\left(T - T_{ref}\right)\right] \quad \text{(I.15)}$$

With :

$I_{sc\_cell}|_{T_{ref}} = \frac{I_{sc\_module}|_{T_{ref}}}{N_p}$ where the value of $I_{sc\_module}|_{T_{ref}}$ is given by the manufacturer. The current $I_{sc\_module}|_{T_{ref}}$ is measured under the irradiance of 1 kW/m^2 and a temperature T_{ref} = 298 K , (25° C).

a: The coefficient of variation of the current as a function of temperature.

T_{ref}: The reference temperature, 298K.

T: The current temperature of the cell in Kelvin.

- The variation of the short-circuit current of a cell ($I_{sc\_cell} = \frac{I_{sc\_module}}{N_p}$) is proportional to the intensity of the irradiation in accordance with the following relationship:

$$I_{sc\_cell}|_G = I_{sc\_cell}|_{G_0}\frac{G}{G_0} \quad \text{(I.16)}$$

With :

G: The current solar irradiation in kW/m2 .

G_0: The standard solar irradiation: G_0 = 1kW/m2

$I_{sc\_cell}|_{G_0}$: The short-circuit current under the reference conditions (T_{ref}, G_0) .

Then from (I.15) and (I.16) the variation of the short-circuit current as a function of any temperature and irradiation is expressed by :

$$I_{sc\_cell}|_{T,G} = I_{sc\_cell}|_{T_{ref},G0}\frac{G}{G_0}\left[1 + a\left(T - T_{ref}\right)\right] \quad \text{(I.17)}$$

I.6.2. Calculation of the saturation current at any temperature:

The variation of the reverse current of the diode is calculated by [9] [13] [14] [15]:

$$I_0\,|_T = I_0\,|_{T_{ref}}\left(\frac{T}{T_{ref}}\right)^3 e^{\frac{-qEg}{nk}\left(\frac{1}{T}-\frac{1}{T_{ref}}\right)} \quad \text{(I.18)}$$

With :

Eg: The width of the forbidden band.

($I_0|T_{ref}$): The reverse current to T_{ref}; given by equation (I.11)

Finally, to calculate the current of the cell it is necessary to solve the equation (I.8) of the nonlinear characteristic, for this we use the Newton method described by :

$$x_{n+1} = x_n - \frac{f(x_n)}{f'(x_n)} \quad \text{(I.19)}$$

Where :

$f'(x)$: The driving of the function $f(xn)$.

$x\,n$: The current value of x .

x_{n+1}: The next value of x .

By applying Newton's method on equation (I.8), he comes :

$$\begin{cases} f(I_{cell}) = I_{sc\_cell}|_T - I_{0_{cell}}|_T\left(e^{\frac{V_{cell}+R_{s\_cell}I_{cell}}{nKT/q}} - 1\right) - I_{cell} \\ f'(I_{cell}) = 0 - I_0\,|_T\frac{R_{s\_cell}}{nKT/q}\left(e^{\frac{V_{cell}+R_{s\_cell}I_{cell}}{nKT/q}}\right) - 1 \end{cases} \quad \text{(I.20)}$$

The application of Newton's method described by (I.19) makes it possible to calculate the value of the current at any temperature and irradiation (T , G) for each iteration (j), so:

$$I_{cell}[j] - \frac{I_{sc_{cell}}|_{T,G} - I_0|_T \left(e^{\frac{V_{cell}[j]+R_{s\_cell}I_{cell}[j]}{nKT/q}} - 1 \right) - I_{cell}[j]}{-I_0|_T \frac{R_{s_{cell}}}{nKT/q} \left(e^{\frac{V_{cell}[j]+R_{s\_cell}I_{cell}[j]}{nKT/q}} \right) - 1} \quad \text{(I.21)}$$

I.7. Characteristics of a photovoltaic cell :

The main characteristic of the solar cell is the I-V characteristic which shows how a photovoltaic cell will respond to all possible charges under a particular set of sunshine and temperature conditions as shown in Figure (I.7) [5].

There are three important points in this curve:

- The optimal operating point at which the cell provides its maximum power (point 5) ;

- The point where the voltage is equal to zero and the current is at maximum (short circuit current, point 4) ;

- The point where the current is equal to zero and the voltage is at maximum (open circuit voltage, point 1).

Also the I-V characteristic can be divided into three ranges:

- A range where the cell is considered as a voltage source (1-2) ;

- A range where the cell is considered as a current source (3-4) ;

- A range where neither the voltage nor the current are constant (2-3).

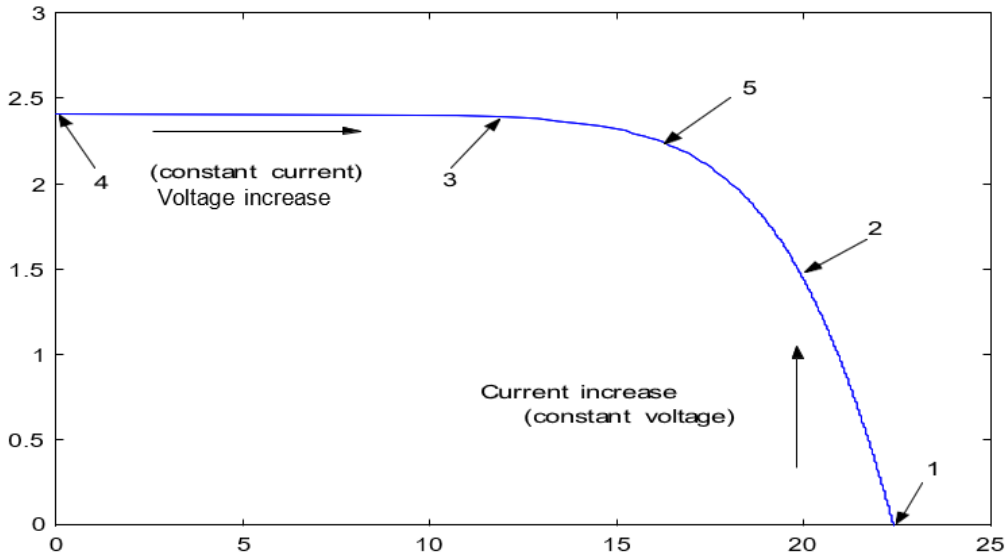

***Fig. I.7**: Typical I-V characteristic of a solar cell.*

I.7.1. Open circuit voltage:

If a solar cell is placed under a constant light source, without any receiver at its terminals, it will produce a DC voltage called open circuit voltage V oc _ cell (it varies slightly with technology and illumination). This value corresponds to the cut-off voltage of a diode, which confirms the fact that a solar cell can be assimilated to a P-N junction. To obtain a higher voltage at the output of the module, it will be necessary to associate the cells in series.

I.7.2. Short circuit current :

Unlike the previous case, if a cell is placed in short-circuit, it will deliver a maximum current at zero voltage; this current is called short-circuit current. The photocurrent provided by the cell is proportional to the light intensity and to the surface of the panel used. Thus, the higher these two parameters will be, the greater the intensity produced will be. As for the voltage, it will be necessary to associate the cells in parallel to significantly increase the value of the intensity at the output of the module.

I.7.3. Power-Voltage Characteristic :

The maximum power delivered by the cell P_{max_cell} is the point of corded to (V_{mp_cell} , I_{mp_cell}) is given by the product between voltage and current as this is indicated by the following formula:

$$P_{\max\_cell} = V_{mp\_cell} \times I_{mp\_cell} \quad \text{(I.22)}$$

I.7.4. Form factor of a PV cell :

The form factor is identified by the ratio of the maximum power to the product of the short-circuit current and the open circuit voltage [5] :

$$FF = \frac{P_{\max\_cell}}{V_{oc\_cell} \times I_{oc\_cell}} \quad \text{(I.23)}$$

I.7.5. efficiency :

The efficiency is the ratio between the maximum power and the power of the incident luminous flux (the surface S of the cell multiplied by the illumination G) [16].

$$n_{pv} = \frac{P_{max\_cell}}{S \times G} \quad \text{(I.24)}$$

Where S: the effective area in m^2 .

I.8. Grouping of cells :

I.8.1. Grouping of cells in series :

By adding identical cells in series as shown in Figure (I.8), the current of the branch remains the same but the voltage increases in proportion to the number of cells in series [17].

I.8.2. Grouping of cells in parallel :

By adding identical cells in parallel as shown in Figure (I.9), the voltage of the branch is equal to the voltage of each cell and the intensity increases proportionally to the number of cells in parallel in the branch.

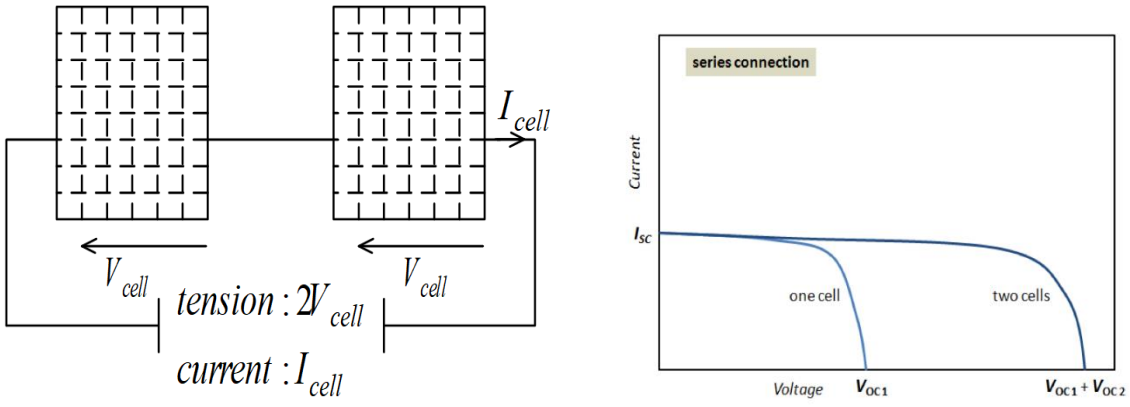

***Fig.I.8**: Cells connected in series with their current-voltage characteristic.*

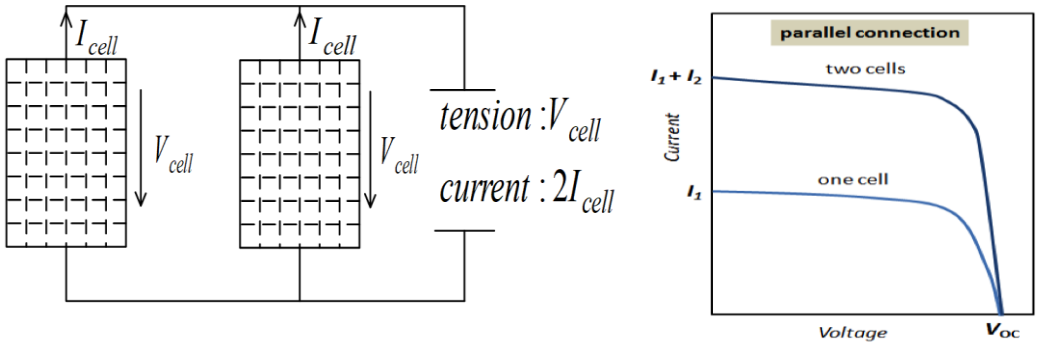

***Fig.1.9**: Cells connected in parallel with their current-voltage characteristic.*

I.9. Photovoltaic module (panel):

A module represented by Fig. (I.10) consists of a set of elementary photovoltaic cells mounted in series and/or in parallel in order to obtain desired electrical characteristics such as power, short-circuit current or open-circuit voltage.

***Fig.I.10**: Photovoltaic module.*

I.9.1. Modeling of the photovoltaic module:

I.9.1.1. Current model :

The model developed for a cell can be understood in the case of connecting the cells in series and in parallel in order to obtain the model of a photovoltaic module (assuming that all these cells are identical inside the module) [18]. Figure (I.11) shows the equivalent model of a photovoltaic module.

If we consider that the photovoltaic module contains N s cells in series and Np cells

in parallel, the current model of the module is based on the following equation [18]:

$$I_{Module} = I_{ph\_Module} - I_{d\_Module} \tag{I.25}$$

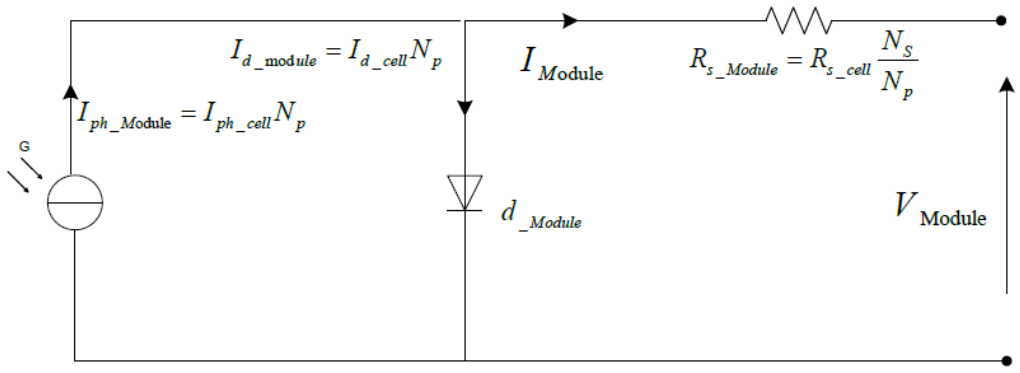

Fig.I.11: *Equivalent circuit of the model of a photovoltaic module (panel).*

With :

$$\begin{cases} I_{ph\_Module} = I_{ph\_cell} N_p = I_{sc\_cell}\,|_T\, N_p \\ I_{d\_Module} = I_{d\_cell} N_p = I_0|_T \left(e^{\frac{V_{cell} + R_{s\_cell} I_{cell}}{nKT/q}} - 1 \right) N_p \end{cases} \tag{I.26}$$

Then the current model of a photovoltaic module is written as:

$$I_{Module} = I_{ph\_Module} - N_p I_0|_T \left(e^{\frac{V_{cell} + R_{s\_cell} I_{cell}}{nKT/q}} - 1 \right) \tag{I.27}$$

I.9.1.2. Model in tension :

The voltage model of the module shown in Figure (I.11) can be deduced from equation (I.27) by observing the following changes :

$$\begin{cases} V_{cell} = \frac{V_{Module}}{N_S} \\ I_{cell} = \frac{I_{Module}}{N_p} \end{cases} \tag{I.28}$$

By replacing equation (I.28) in equation (I.27), the voltage of the photovoltaic module can be deduced as follows:

$$V_{Module} = N_S \left[nKT/q \; ln \left(\frac{I_{ph\_Module} - I_{Module}}{N_p I_0|_T} \right) \right] - R_{s\_module} \frac{I_{Module}}{N_S} \tag{I.29}$$

Where R_{s_Module} represents the serial resistance of the module ($R_{s\_Module} = R_{s\_cell} \frac{N_S}{N_p}$)

For our case, based on the voltage model of the cell described by (I.9), it is possible to calculate directly the module voltage at any temperature T:

$$V_{Module} = N_S V_{cell} = N_S \left[{}^{nKT}/_{q} \, ln\left(\frac{I_{ph\_cell}|_T - I_{cell} + I_0|_T}{I_0|_T} \right) \right] - R_{s\_cell}|_T I_{cell} \qquad \text{(I.30)}$$

I.10. Electrical characteristics of a photovoltaic module :

In our work we have adopted the BP SX 150 photovoltaic module from BP Solaire. BP Solaire's SX series provides cost-effective photovoltaic power for general use by direct exploitation of direct current loads, or alternating current loads on systems equipped with inverters. The module is composed of 72 multi crystalline silicone solar cells connected in series to produce a maximum power of 150W.

The electrical characteristics of this photovoltaic module are given by the manufacturer (BP Solar's SX series) in Table (I.1).

Electrical Characteristics[1]

	SX 150	SX 140[2]
Maximum power (P_{max})[3]	150W	140W
Voltage at P_{max} (V_{mp})	34.5V	34.0V
Current at P_{max} (I_{mp})	4.35A	4.11A
Warranted minimum P_{max}	140W	130W
Short-circuit current (I_{sc})	4.75A	4.5A
Open-circuit voltage (V_{oc})	43.5V	42.8V
Temperature coefficient of I_{sc}	(0.065±0.015)%/°C	
Temperature coefficient of voltage	-(160±20)mV/°C	
Temperature coefficient of power	-(0.5±0.05)%/°C	
NOCT[5]	47±2°C	
Maximum series fuse rating	20A (U version) 15A (S, L versions)	
Maximum system voltage	600V (U.S. NEC rating) 1000V[4] (TÜV Rheinland rating)	

Table I.1: Electrical characteristics of the photovoltaic module BP SX 150.

The current-voltage characteristic illustrated in Figure (I.12) describes the behavior of the photovoltaic module under the influence of specific weather conditions (illumination level G=1000 and ambient temperature T=25°C.) [17].

The I-V curve of the photovoltaic module passes through three important points which are :

- The short-circuit current I_{sc_Module} in C.

- The open circuit voltage V_{oc_Module} in S.

- The maximum power P_{max} in M.

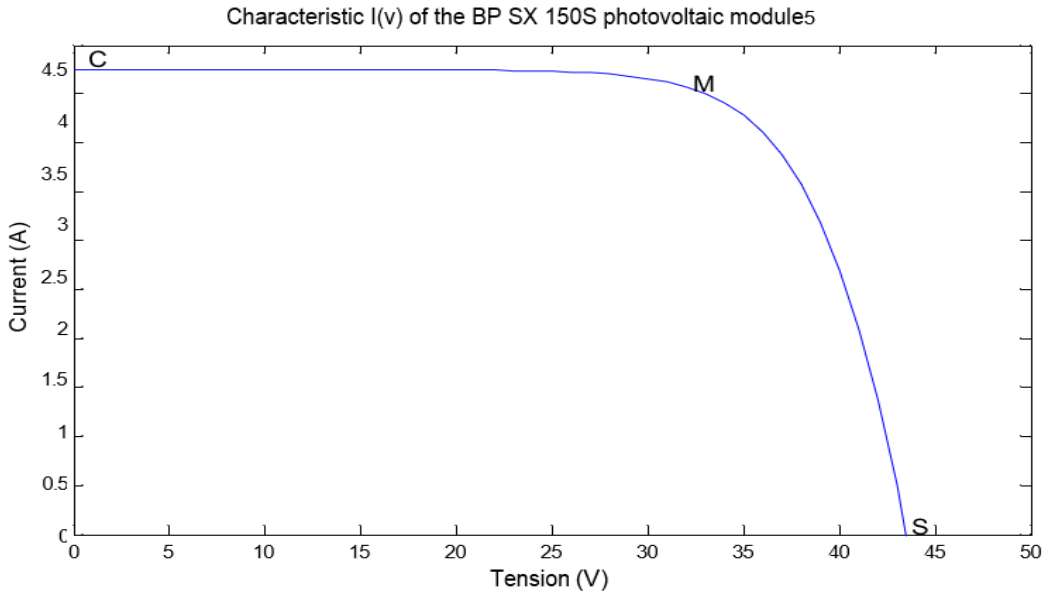

***Fig. I.12**: I-V characteristic of a photovoltaic module.*

I.10.1. Influence of sunlight on I_{sc_Module} ,V_{oc_Module} and P_{max} :

Figs. (I.13) and (I.14) represent the variations of the current and of the power as a function of the voltage for different levels of illumination at a constant maintained temperature. It should be noted that the value of the short-circuit current is directly proportional to the intensity of the radiation [9]. On the other hand, the open circuit voltage does not vary in the same proportions, it remains almost identical even at low illumination [19].

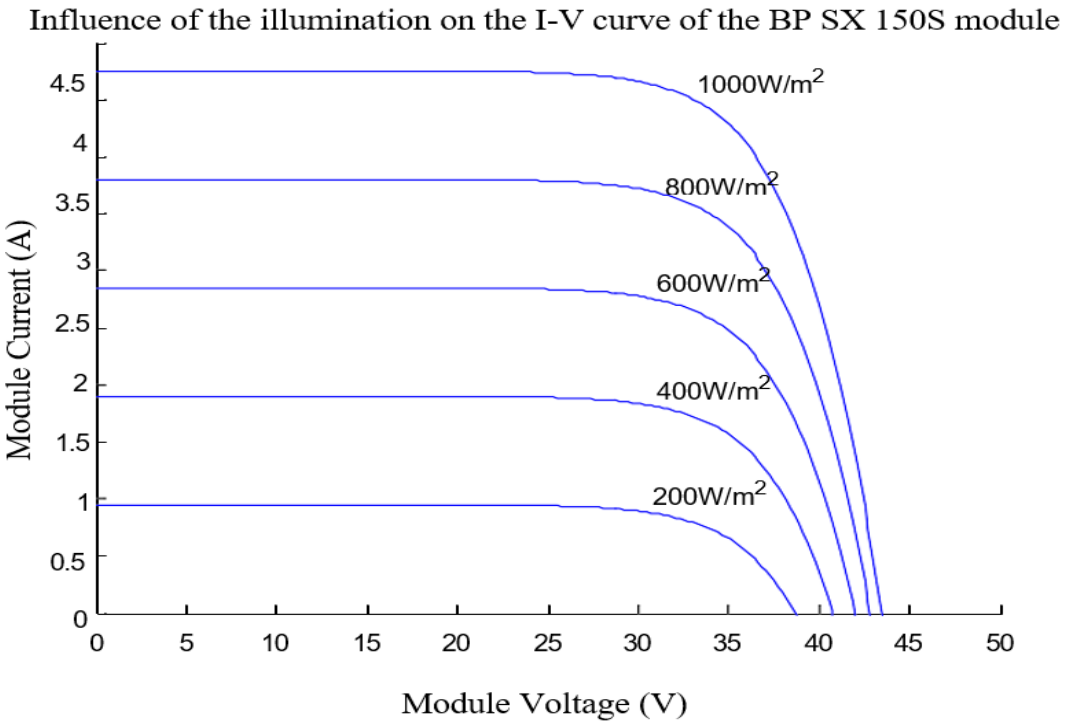

Fig.I.13: *I-V curves of a panel with various sun exposure.*

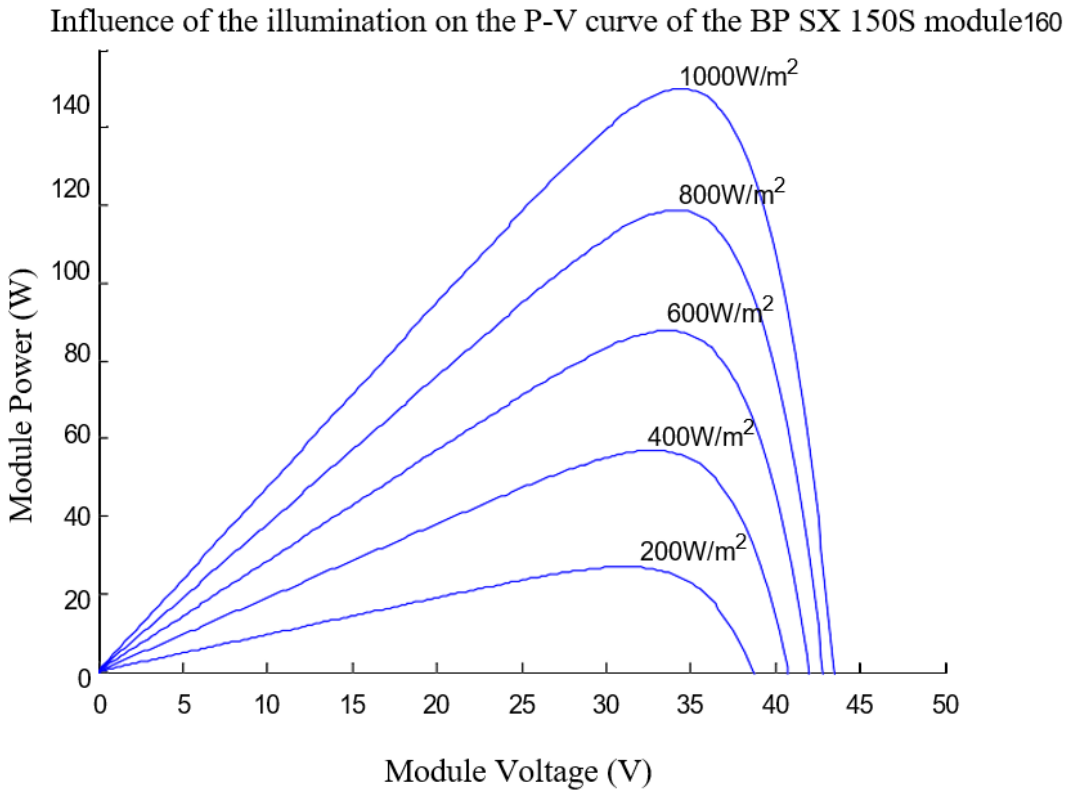

Fig. I.14*: P-V curves of a photovoltaic module with various sun exposures.*

I.10.2. Influence of temperature on I_{sc_Module} ,V_{oc_Module} and P_{max}

Figs. (I.15) and (I.16) show the curves I-V, P-V for different operating temperatures of the photovoltaic module at a constant irradiation. We note that the temperature has a negligible influence on the value of the short-circuit current. On the other hand, the open-circuit voltage drops quite sharply when the temperature rises (This decrease is of the order of 2 mV per degree [4]).

The increase in temperature also results in a decrease in the maximum available power (this variation is of the order of 0.35% per degree [4]). Therefore, when dimensioning an installation, it is imperative to take into account the variation in the temperature of the site.

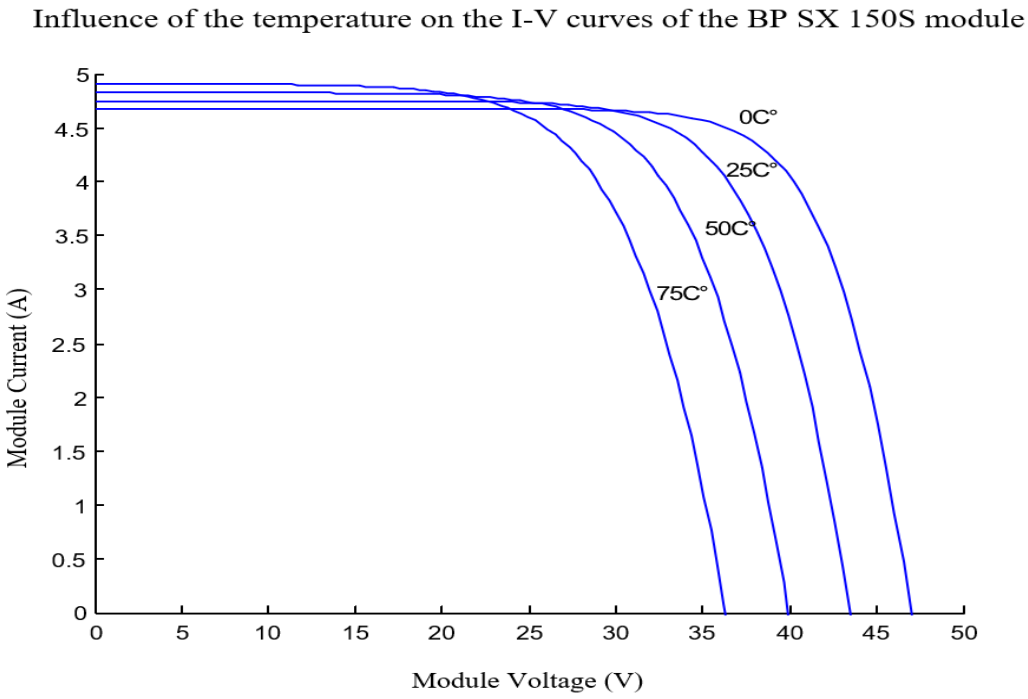

***Fig. I.15**: I-V curves of a photovoltaic module for different temperatures at G=1000 W/m².*

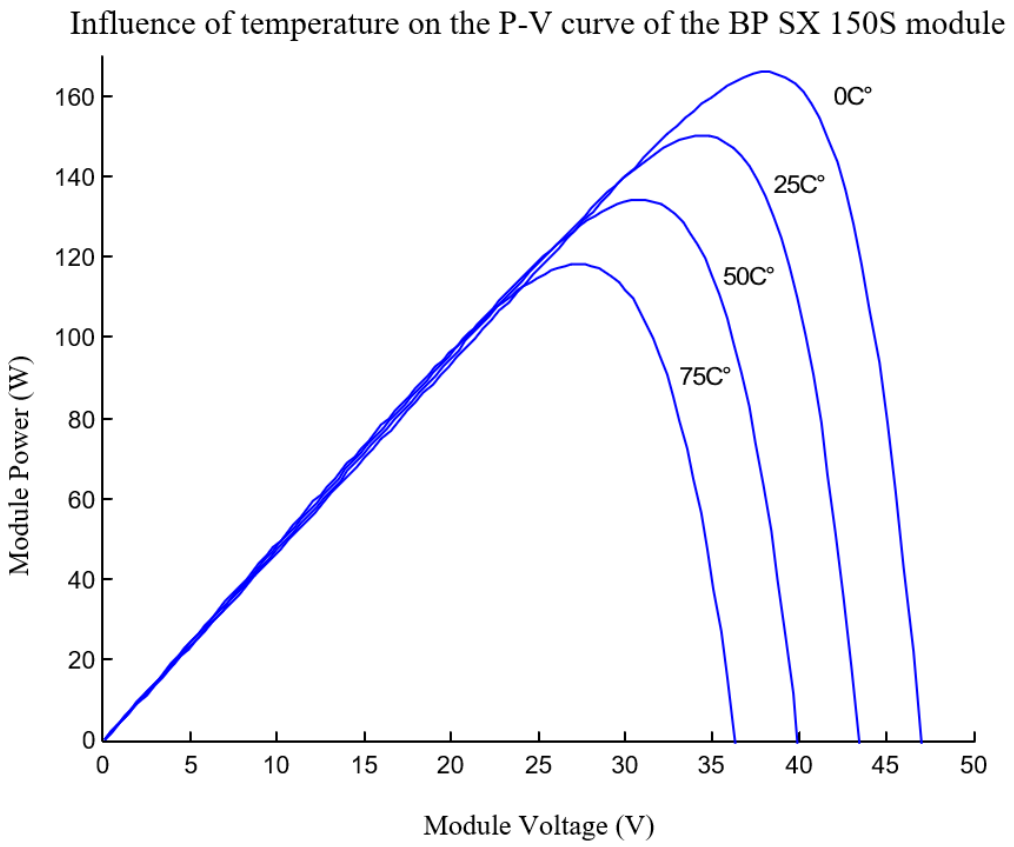

***Fig. I.16**: P(V) curves of a photovoltaic module for different temperatures at G=1000 W/m².*

I.10.3. Influence of series resistance :

Fig. (I.17) shows the influence of the series resistance on the I-V curve of the photovoltaic module, this influence resulting in a decrease in the slope of the I-V curve and a decrease in power produced by the power module as shown in Fig. (1.18).

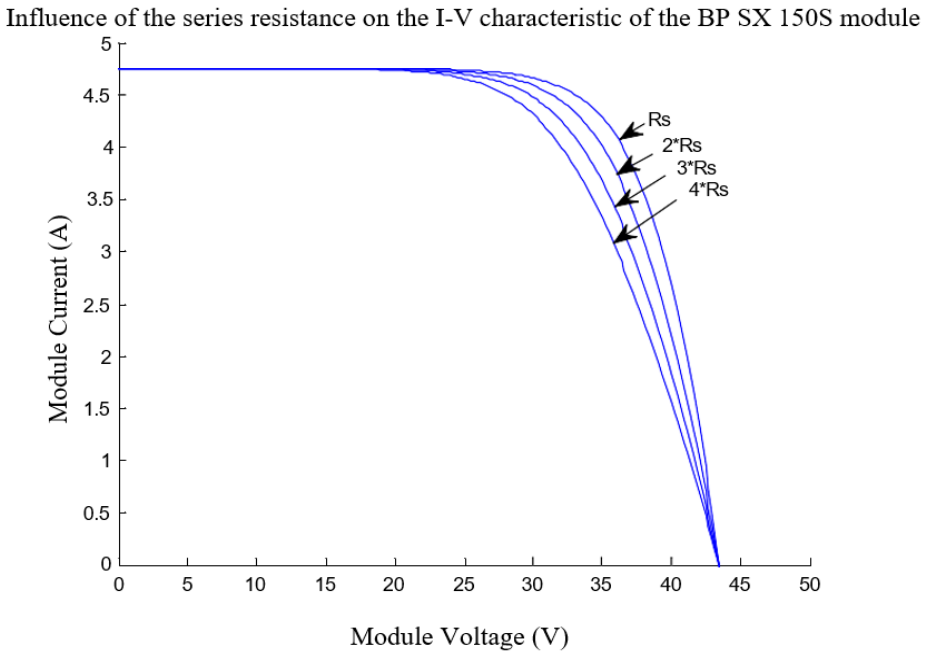

***Fig. I.17**: Influence of the series resistance on the I-V characteristic of the photovoltaic module .*

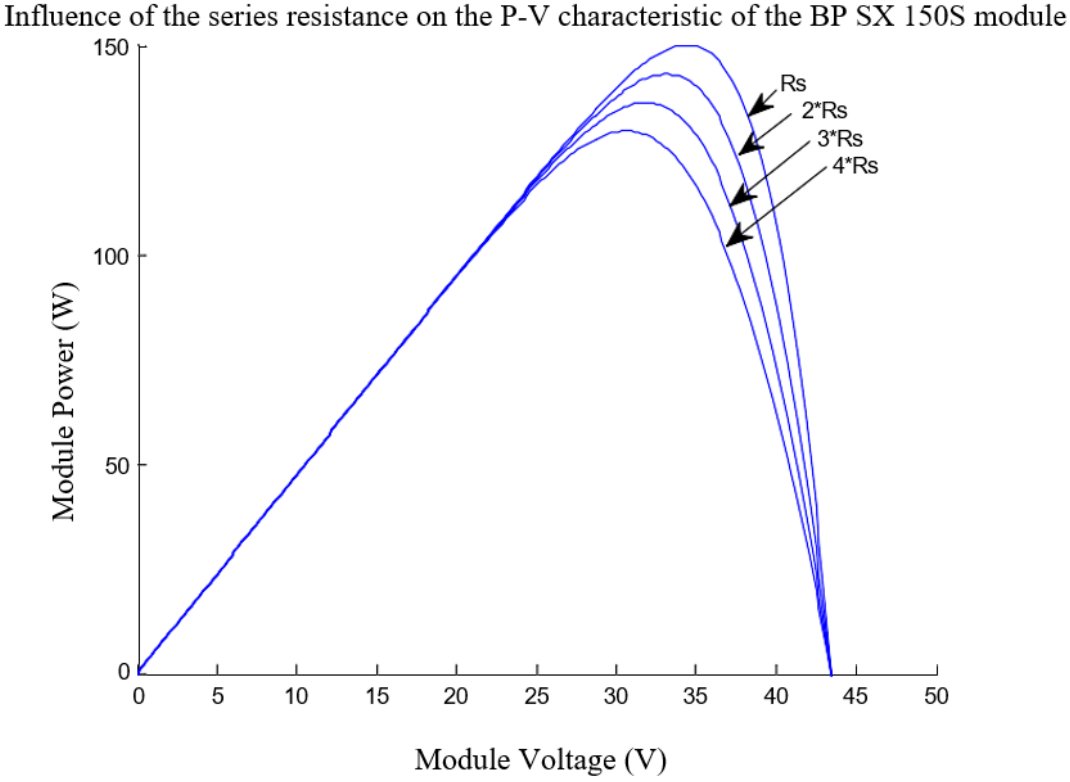

***Fig. I.18:** Influence of the series resistance on the P-V characteristic of the photovoltaic module.*

I.11. Photovoltaic generator :

I.11.1. Constitution of a photovoltaic generator :

To obtain higher powers, it is necessary to associate several modules in series and / or in parallel as shown in Figure (I.19). The operating curve of a series-parallel association of the modules is a curve similar to the curve of the base cell, with of course different electrical parameters. Note here that, similarly for the cells, it will be necessary to associate in series and in parallel only identical modules [20].

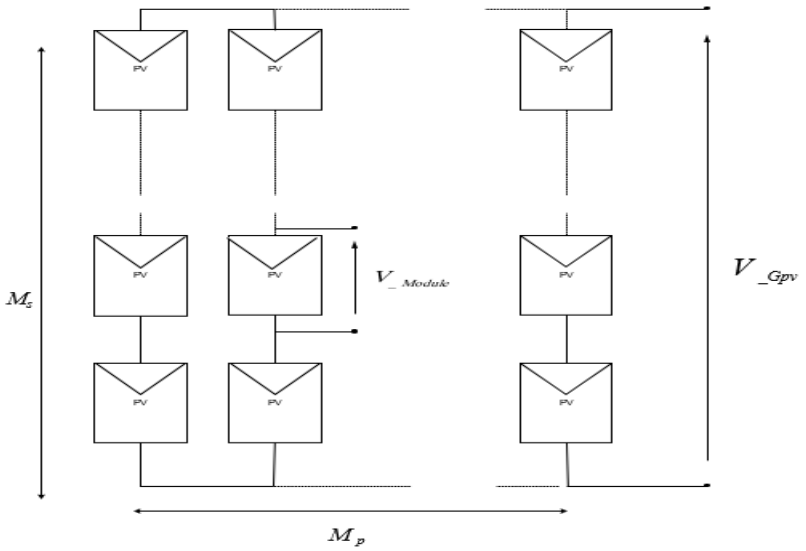

Fig.I.19: *Photovoltaic modules connected in series and in parallel.*

Fig.I.20*: Grouping of photovoltaic modules.*

I.11.2. Modeling of a photovoltaic generator :

I.11.2.1. Current model :

The model of a photovoltaic generator (GPV) can be represented by the equivalent circuit of Fig. (I.21) [13] [18] [21] [22].

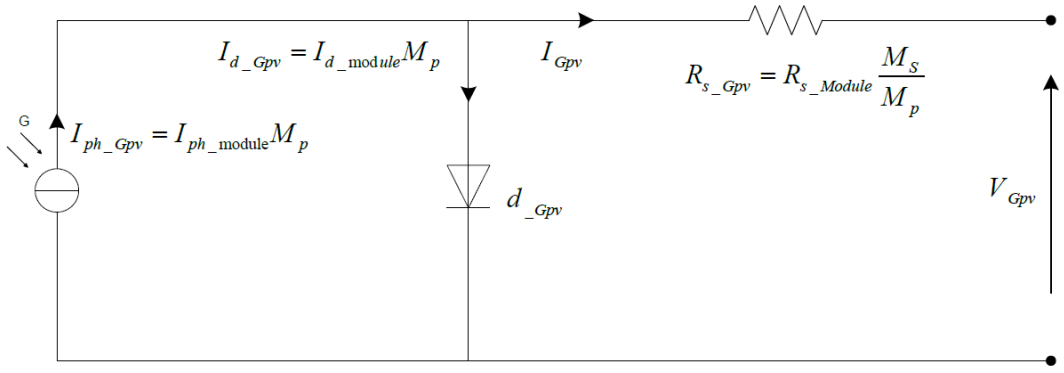

Fig.I.21: *Equivalent circuit of the model of a photovoltaic generator.*

If it is assumed that the photovoltaic generator contains M_s modules in series and M_p modules in parallel, and each module contains N_s cells in series and N_p cells in parallel, then the mathematical model can be developed in the same way as the photovoltaic module.

Indeed, the current delivered by the photovoltaic generator is given by :

$$I_{Gpv} = I_{ph\_Gpv} - I_{d\_Gpv} \tag{I.31}$$

The relationships between the magnitudes of the generator and those of the module are :

$$\begin{cases} I_{ph\_Gpv} = I_{ph\_Module} M_p \\ I_{d\_Gpv} = I_{d\_Module} M_p \end{cases} \tag{I.32}$$

On the other hand, the relations between the quantities of the module and those of the cell are expressed by the equation (I.26).

Substituting (I.26) in (I.32) we find :

$$\begin{cases} I_{ph\_Gpv} = I_{sc\_cell}\,|_T N_p M_p \\ I_{d\_Gpv} = I_0|_T \left(e^{\frac{V_{cell} + R_{S\_cell} I_{cell}}{nKT/q}} - 1 \right) N_p M_p \end{cases} \tag{I.33}$$

By replacing the first and the second equation of (I.33) in (I.31), we obtain the mathematical model of photovoltaic generator :

$$I_{Gpv} = I_{sc\_cell}\,|_T (N_p M_p) - (N_p M_p)\, I_0|_T \left(e^{\frac{V_{cell} + R_{S\_cell} I_{cell}}{nKT/q}} - 1 \right) \tag{I.34}$$

I.11.2.2. Voltage model :

The generator voltage model shown in Figure (I.21) can be deduced from equation (I. 34) by observing the following changes :

$$\begin{cases} V_{cell} = \frac{V_{Module}}{N_S} = \frac{V_{Gpv}}{N_S M_S} \\ I_{cell} = \frac{I_{Module}}{N_p} = \frac{I_{Gpv}}{N_p M_p} \end{cases} \quad (I.35)$$

By replacing (I.35) in (I.34), we obtain :

$$I_{Gpv} = I_{sc\_cell}\,|_T(N_p M_p) - (N_p M_p)\, I_0|_T \left(e^{\frac{\frac{V_{Gpv}}{N_S M_S} + R_{s\_cell}\frac{I_{Gpv}}{N_p M_p}}{nKT/q}} - 1 \right) \quad (I.36)$$

Which leads to:

$$V_{Gpv} = \left[(N_s M_s)\, nKT/q\; ln\left(\frac{I_{sc\_cell}|_T(N_p M_p) - I_{Gpv}}{I_0|_T(N_p \times M_p)} + 1 \right) - R_{s\_Gpv} I_{Gpv} \right] \quad (I.37)$$

Where R_{s_Gpv} represents the generator series resistor with ($R_{s\_Gpv} = R_{s\_Module}\frac{M_s}{M_p}$)

I.12. Conventional protections for a photovoltaic generator :

When we design a photovoltaic installation, we must ensure the electrical protection of this installation in order to increase its service life by avoiding in particular destructive failures related to the association of the cells and their operation in case of shading. For this, two types of protections are conventionally used in current installations:

- protection in case of parallel connection of photovoltaic modules to avoid negative currents in the photovoltaic generator (anti-return diode) ;

- protection during the series connection of photovoltaic modules making it possible not to lose the entire chain (bypass diode) and avoid hot spots.

Fig. (I.22) shows the schematic conventionally adopted for the protection of the elementary GPV [5].

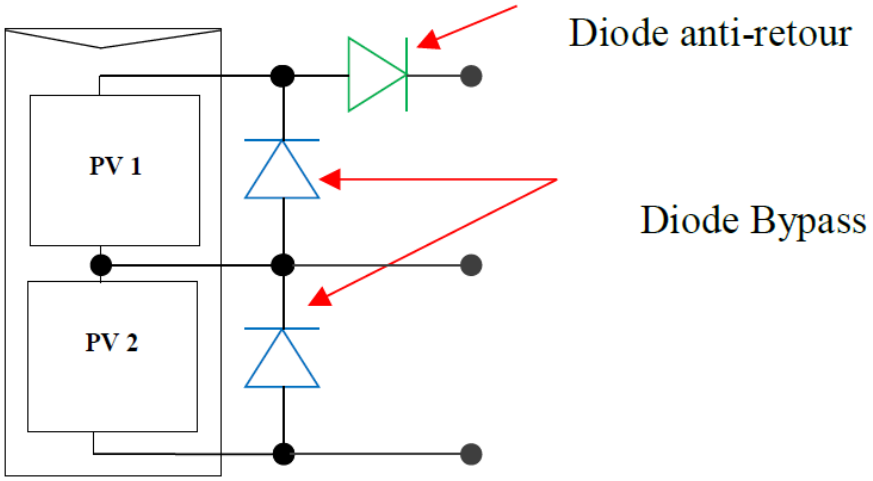

***Fig.I.22**: Schematization of an elementary photovoltaic generator with bypass diodes and anti-reverse diode.*

I.13. Conclusion :

Photovoltaic solar energy comes from the direct transformation of part of the solar radiation into electrical energy. This energy conversion is carried out by the photovoltaic cell based on a physical phenomenon called the photovoltaic effect. The voltage generated can vary depending on the material used to manufacture the cell.

The association of several cells in series and / or in parallel gives rise to a photovoltaic module. The modules can also be connected in series and/or in parallel to build the photovoltaic generator in order to increase the voltage and the intensity of use.

In this chapter we have represented the principle of photovoltaic conversion, the modulization of a cell, a photovoltaic module and a photovoltaic generator.

We have also presented the influence of climatic conditions (solar irradiation, degree of temperature) and the influence of the series resistance on the I-V and P-V curves of the photovoltaic module.

Chapter II

Modeling a battery

II.1.Description of battery

An integral component of the hybrid system, batteries provide the ideal assistance for power delivery and support FCs in the event of an unexpected load [23]. These electrochemical devices fall into two categories: main batteries, which are non-rechargeable, and secondary batteries, which are rechargeable [24]. For the latter, electrical energy can be transformed into chemical energy while charging, and the chemical energy can be transformed back into electric energy when discharging [25]. These batteries, which include lead-acid, lithium-ion, and sodium-sulfur batteries, are used to store and supply electricity to and from renewable energy and clean energy-based power systems. They should also be dependable, long-lasting, and safe [26].

The term "cell" refers to batteries made up of a single electrochemical cell. To achieve the required voltage and storage capacity, these cells can thus be put together in parallel or series to create batteries [24].

II.2.Components of battery

- **Negative and positive electrodes**

The redox processes take place between the two electrodes [27]. Additionally, the positive electrode is made of metal oxides, whereas the negative electrode is made of a mixture of carbon-based compounds.

- **Electrolyte**

The electrolyte, which can be a liquid, polymeric, or solid, permits ions to pass through and flow only. Liquid electrolytes are currently the most widely used for a variety of purposes [28].

- **Separator**

In cases where the electrolyte is liquid, separator insulation—a microporous membrane that allows only ions to flow—must be placed between the electrodes to

prevent internal short circuits [27],[29]. Cylindrical, pouch, or prismatic cells are examples of many battery forms [30], as shown in Figure (II.1).

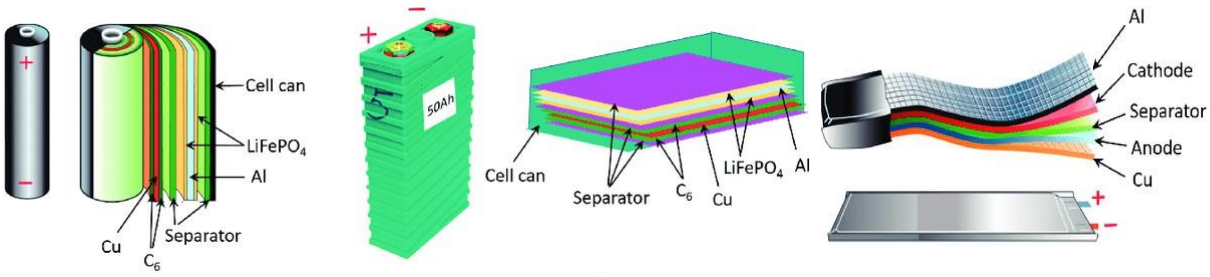

(a) (b) (c)

Fig.II.1: *Representation of the shape and components of various Li-ion battery configurations.Cylindrical (a), prismatic (b), and pouch cell (c) [31].*

II.3. Classification of batteries

Depending on the materials used for electrodes one can find many promising batteries technologies [32] [33] [34] , as described in Table (II.1).

Type	Lithium-ion	Lead-acid	Nickel-cadmium	Nickel-metal
Negative electrode	*Graphite*	*Pb*	*Cd*	*MH*
Positive electrode	$LiCoO_2$	PbO_2	$Ni(OH)_2$	$Ni(OH)_2$
Electrolyte	*Organic*	H_2SO_4	*KOH*	*KOH*
Nominal voltage (V)	3.6	2	1.25	1.25
Energy density (Wh/Kg)	110-160	30-50	45-80	60-120
Power density (W/Kg)	1800	180	150	250-1000
Overcharge tolerance	Very low	High	Moderate	Low
Self-discharge rate	Very low	Low	Moderate	High
Operating temperature (°C)	-20 to 60	-20 to 60	-40 to 60	-20 to 60
Number of cycle life	500-1000	200-300	1500	300-500

Table II.1: *Classifications of battery.*

II.4. Lithium-ion battery (Li-ion battery)

The lithium-ion battery is the best commercially available battery in terms of power density because of lithium's lightweight and fast response [35]. It has three layers, negative and positive electrodes, and electrolyte, and it works similarly to a capacitor.

As seen in Figure (II.2), graphite is commonly utilized as an intercalation material of lithium (LiC6) at the negative electrode. To put it another way, graphite, one of the allotropic forms of carbon, has a hexagonal shape, making it the most thermodynamically stable phase. It also creates planar layers that enable the wedgeing and storage of lithium between the layers. Intercalation is the technical word for this [33].

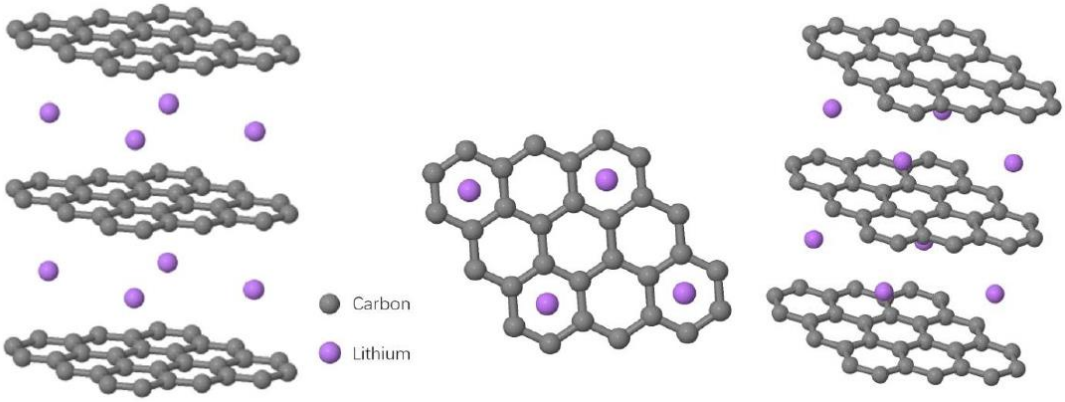

***Fig.II.2**: Representation of Li-ion battery negative electrode [60].*

There are three primary types of positive electrode materials. Lamellar transition metal oxides, metal oxides with polyanionic structure (found in olivine-like structural materials, iron phosphates), and oxides of spinal structure are the most researched [33]. According to the latter, the most often utilized positive electrode material in commercial and rechargeable lithium batteries is LiCoO2 (lithium cobalt oxide) [36]. As seen in Figure (II.3), this material has a lamellar structure with a rhombohedral crystalline mesh made of oxygen atoms with alternating layers of cobalt and lithium ions [37]. This shape makes it simple to incorporate lithium ions into the matrix.

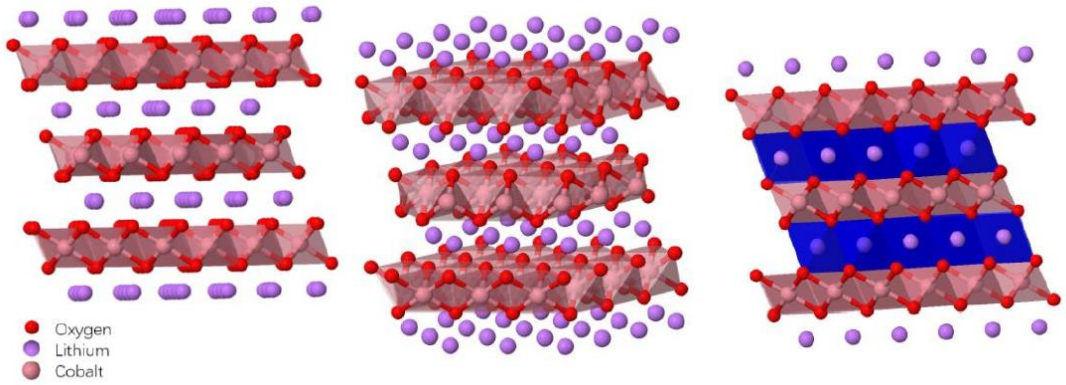

***Fig.II.3**: Representation of Li-ion battery positive electrode [38].*

There is a conductive copper layer added to graphite [39] and a conductive aluminum layer adjacent to the cobalt oxide [40] since graphite and cobalt peroxide materials are not good at spreading or collecting electrons. We refer to these two levels as collectors.

Lithium salts can also be dissolved in organic (non-aqueous) solvents to produce an electrolyte [28]. Since it provides a good balance between ionic conductivity, stability, and cost, lithium hexafluorophosphate (LiPF6) is the most commonly used salt on an industrial scale [41]. Other salts are abbreviated as lithium hexafluoro arsenic (LiAsF6), lithium perchlorate (LiClO4), and lithium tetrafluoroborate (LiBF4). The most often utilized solvents are ethylene carbonate (EC) and propylene carbonate (PC) shortened solvents. Diethyl carbonate (DEC) and dimethyl carbonate (DMC) were co-solvents. The commonly utilized composition, designated "LP30" [33], is based on LiPF6 dissolved in a mixture of ethylene carbonate (EC) and dimethyl carbonate (DMC), as shown in Figure (1.8 (a)).

Li+ ions bind to the oxygen atoms of the DMC, forming and breaking bonds in fractions of a second, and are aggregated in ion pairs with PF-6. Li+ is therefore mostly coordinated with polarizable carbonyl groups. According to Figure (1.8 (b) and (c)), the presence of a Li+ ion that is coordinated with a carbonyl group will cause the associated EC or DMC molecule with its carbonyl group to be oriented slightly towards the next layer [42].

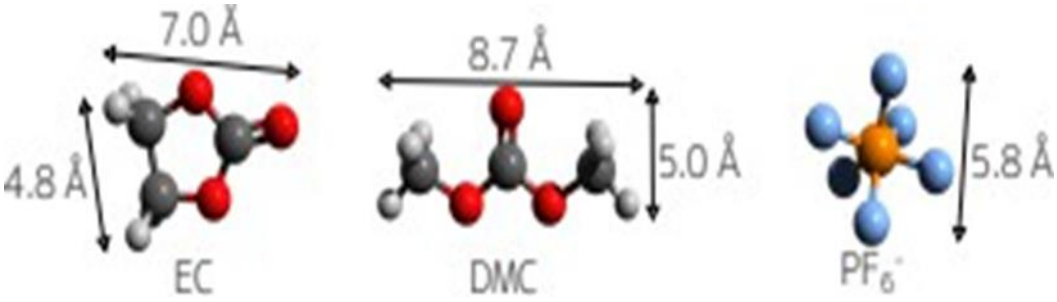

(a) Sketches of the molecules of the individual species comprising the investigated LiPF6 in EC: DMC electrolyte solution, the arrows indicate the molecular size, and include the molecules' van-der-Waals radii [42].

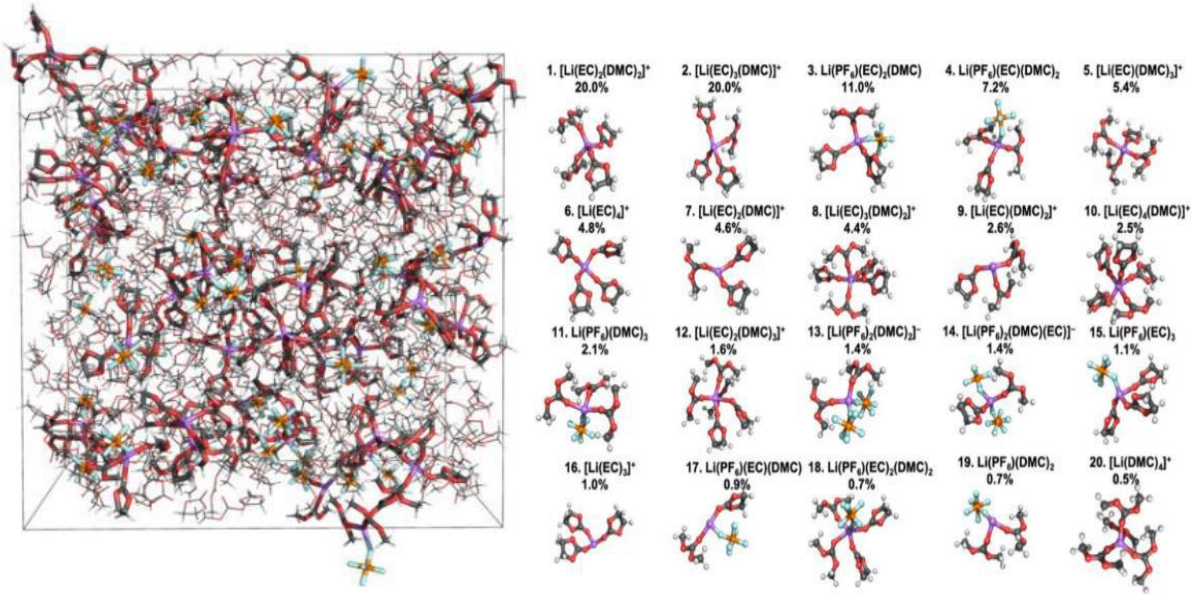

(b) the overall structure of LP30 [43]. (c) the 20 most common Li+ 1st solvation shell structures, and Li+ probabilities (in percentages) [43].

***Fig.II.4**: Representation of Li-ion battery electrolyte.*

The principal contributors to the (Li+) ion transport: are purple: Li; orange: P; cyan: F; red: O; grey: C; white: H.

Since the electrolyte is an organic solvent, it contains a crucial component for ensuring its high safety, known as the plastic separator; more precisely, polyethylene (PE) is the most prevalent material in Li-ion batteries [44].

II.4.1.Operating principle of the Li-on battery

The following describes the Li-ion battery's [28] working principle in detail:

According to the subsequent oxidation reaction shown in equation (II.1), during discharge (use), the negative electrode will release electrons to the external circuit through

an electrochemical oxidation reaction. This process also causes the deintercalation of lithium ions from the graphitic planes.

$$Li_xC_6 \longrightarrow 6C + xLi^+ + xe^- \quad \text{(II.1)}$$

According to the subsequent reduction reaction seen in equation (II.2), Li+ ions are thus generated with the electrode negative during the discharge process, then moved from one electrode to another through the ionic conductive electrolyte and consumed by the positive electrode via an insertion reaction.

$$Li_{1-x}CoO_2 + xLi^+ + xe^- \rightarrow LiCoO_2 \quad \text{(II.2)}$$

Because an external generator is used to impose an opposite current during the charge, the opposite phenomenon—oxidation to the positive electrode (lithium extraction) and reduction to the negative electrode (lithium insertion) will occur. Equation (II.3) describes the general equation for this process.

$$Li_xC_6 + Li_{1-x}CoO_2 \underset{Charge}{\overset{Discharge}{\rightleftharpoons}} LiCoO_2 + 6\,C \quad \text{(II.3)}$$

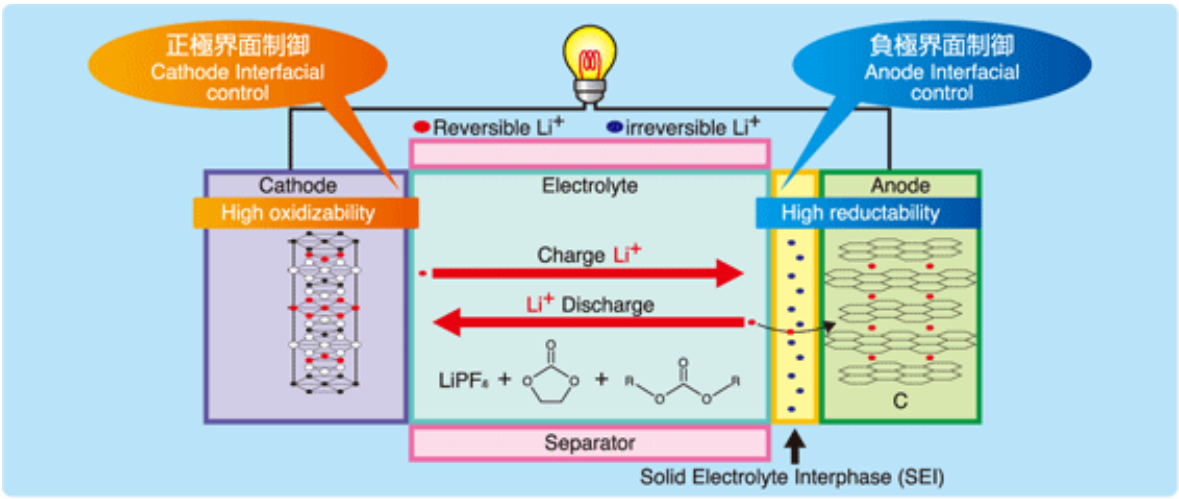

***Fig.II.5**: Operation of the Li-ion battery [45].*

II.4.2.Advantages and limitations of Li-ion batteries

II.4.2.1.Advantages

- High energy density [46].
- Relatively low self-discharge [46].
- Low-down maintenance [46].
- Adequate performance even in low temperatures [48].
- Long longevity of service [47].

II.4.2.2.Limitations

- Expensive to fabricate than other kinds [46].
- Require costly surveillance criteria; utilized to evade explosion when their temperature is too hot [47].

II.5. Mathematical model of battery

The batteries considered for this study are of the Li-ion type because they have been shown to exhibit high energy density and efficiency compared to other battery types (such as lead-acid, NiCd or NiMH); this feature makes them more attractive for automotive or aircraft applications [49].

II.5.1. Li-ion battery voltage

The battery voltage is expressed as :

$$V_{bat} = E_{bat} - R_{int} I_{bat} \quad \text{(II.4)}$$

The open circuit voltage E_{bat} for charge and discharge is expressed as:

$$E_{bat} = \begin{cases} E_0 - K\frac{Q}{Q-it} i^* - K\frac{Q}{Q-it} it + A_0 e^{-Bit} & When\ i^* > 0\ (discharge\ mode) \\ E_0 - K\frac{Q}{0.1Q-it} i^* - K\frac{Q}{Q-it} it + A_0 e^{-Bit} & When\ i^* < 0\ (charge\ mode) \end{cases} \quad \text{(II.5)}$$

- E_0 : is the battery constant voltage (V).
- K : is the polarization constant $V/(Ah)$.
- Q : is the battery capacity (Ah).
- i^*: is the filtered battery current (A),
- it : is the actual battery charge (Ah).
- A_0 : is the exponential zone amplitude (V).
- B : is the exponential zone time constant inverse $(Ah)^{-1}$.
- R_{int} : is the battery internal resistance (Ω).

The term $K\frac{Q}{Q-it} it$ from equation (II.5) referred as polarization voltage , while The term $K\frac{Q}{Q-it} it$ is the polarization resistance (Pol_{res}).

During charging mode, the battery voltage increases abruptly after being

fully charged, this behavior is represented by modifying the polarization resistance (only during charging) as follows:

$$K\frac{Q}{it-0.1Q} \tag{II.6}$$

The transfer function of the current filter is as follows :

$$G = \frac{1}{6.67s+1} \tag{II.7}$$

Figure (II.6) shows block diagram of the battery model implemented in SPS.

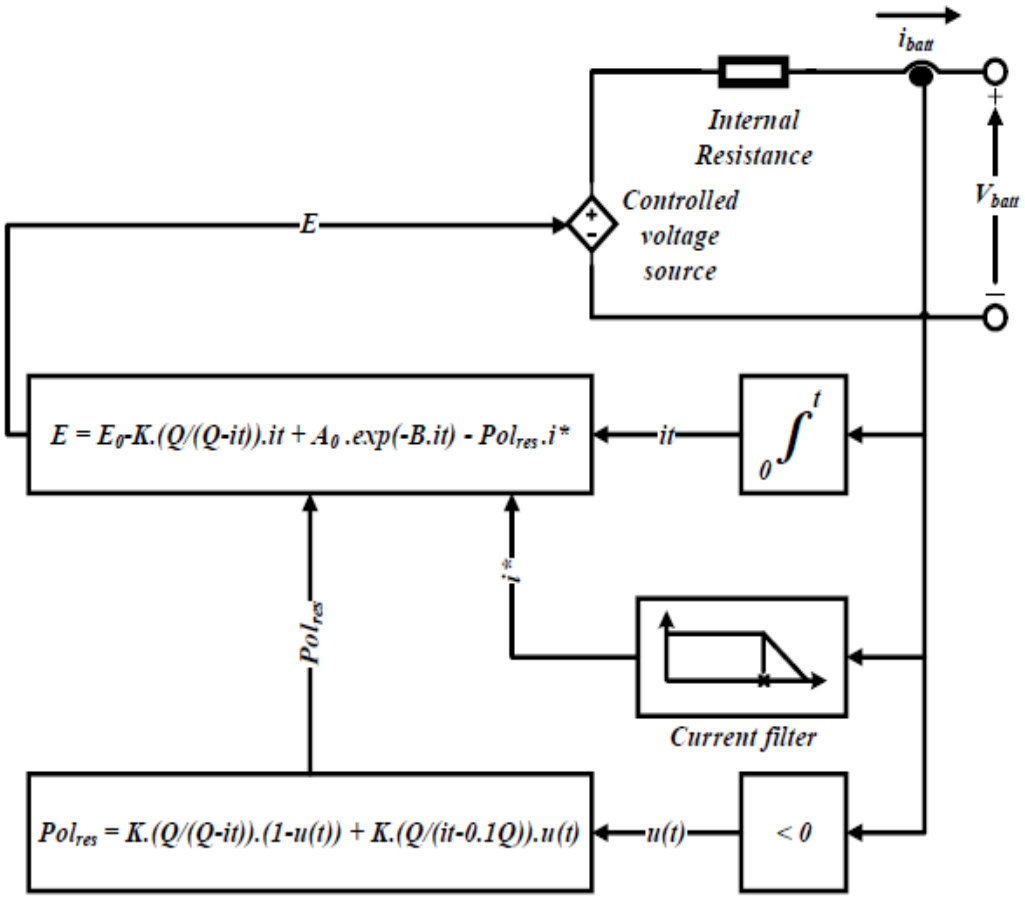

Fig.II.6: *Li-ion battery model [50].*

In mode charge u(t)=1 and in mode discharge u(t)=0.

II.5.2. State of charge

The remaining available capacity in the battery, expressed as a percentage of the rated capacity, is known as the state of charge (SOC), and it is frequently shortened to SOC (State of Charge). This is a crucial feature to understand because it tells us, in percentage terms, the battery load level; the ability to estimate charge status prevents deep discharges or overcharges that could harm batteries [51].

$$soc(\%) = 100(1 - \frac{1}{Q}\int_0^t I_{bat}(t))dt \quad \text{(II.8)}$$

II.6. Conclusion

In this chapter, we have discussed the advantages and limitations of lithium-ion (Li ion) batteries, highlighting their high energy density, long cycle life, and relatively low self-discharge rates. We have also examined the key challenges associated with Li-ion batteries, such as cost, safety concerns, and performance degradation over time.

Additionally, we have presented a mathematical model of a Li-ion battery, emphasizing the importance of understanding battery behavior under varying operating conditions. This model incorporates electrochemical and thermal dynamics, providing insights into the performance and optimization of battery management systems (BMS), and contributing to the efficient design and development of energy storage systems.

Chapter III

Control of a system PV /BATTERY by PI

III.1.Introduction

The current energy transition encourages the development of renewable energy sources, in particular solar energy, which is emerging as a clean, silent and abundant solution. However, the natural intermittency of sunlight poses major challenges in terms of energy regulation and storage [52]. In this context, the integration of a photovoltaic system coupled to a battery not only makes it possible to store the excess energy but also to restore it according to needs [53]. To ensure an effective management of this architecture, it is crucial to adopt a reliable control strategy. The proportional-integral regulator (PI) presents itself as a tool of choice thanks to its simplicity of implementation and its ability to improve the stability of the system while reducing the static error [54]. This study explores the application of the PI regulator to optimize the operation of a PV / battery system, by ensuring an efficient regulation of the voltage or current according to energy requirements [55].

III.2.Power converters modeling

The PV system and the battery are connected to DC-DC converters. This allows voltage conversion (from low voltage to high voltage and vice-versa) as well as full control of the PV system/battery current and DC-bus voltage. The PV system is controlled by a DC-DC boost converter [65]. Similarly, the Li-ion battery is controlled by bidirectional DC-DC buck-boost converters, since during operation they are charging and discharging [57]. The converter operates in boost mode when the battery discharges and it works in Buck mode for it charge [51]. DC-DC converters can be represented by two types of models, which are: the switching models and the average-value models. The switching models are mainly used for design purpose and to investigate types of pulse-width-modulated (PWM) schemes with regards to switching harmonics and losses. These models require small sampling time to observe all the switching actions, which makes the simulation very time consuming [58]. In the averaged model, the power electronic switch and diode are replaced by a combination

of controlled current and voltage sources. This gives the same performance as the detailed circuit model at less time [59].

III.2.1: DC-DC boost converter model and control

III.2.1.1:Model of boost converter

In this subsection, a unidirectional DC-DC boost converter is considered to convert the DC power generated by the PEM fuel cell stack to an output controlled DC power [60]. As illustrated in Figure (III.1), the DC-DC boost converter circuit consists of a semiconductor power switch, diode and inductor to transfer the energy from input to output. Control circuitry is added to the boost converter to handle the energy transfer and to maintain the current and/or voltage in normal operating range [61].

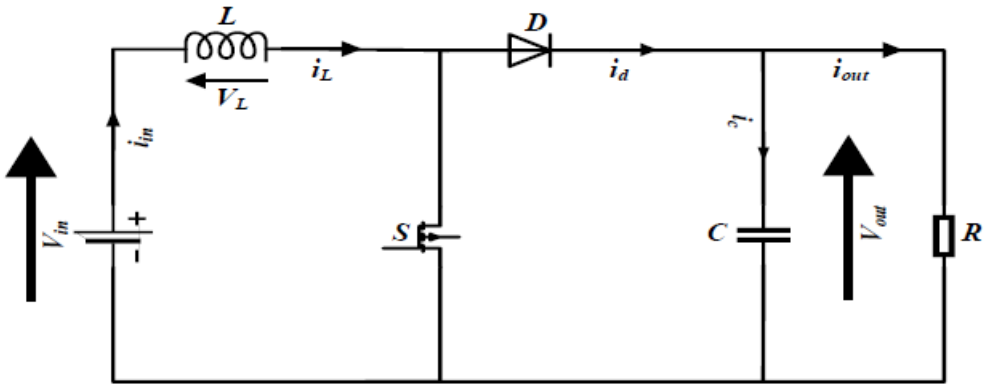

Fig.III.1: *Structure of a classic boost converter.*

There are two ways the DC-DC converter can operate, depending on the form of the inductance's current:

- Discontinuous conduction mode (DCM): the inductance current is periodically canceled.
- Continuous conduction mode (CCM): the inductance current is never cancelled [68].

Kirchhoff's voltage and current rules in continuous mode are used to derive the mathematical model of the DC-DC boost converter that has been used. Based on the switching position function (S=1 (Figure (III.2)) or S=0 (Figure (III.3))).

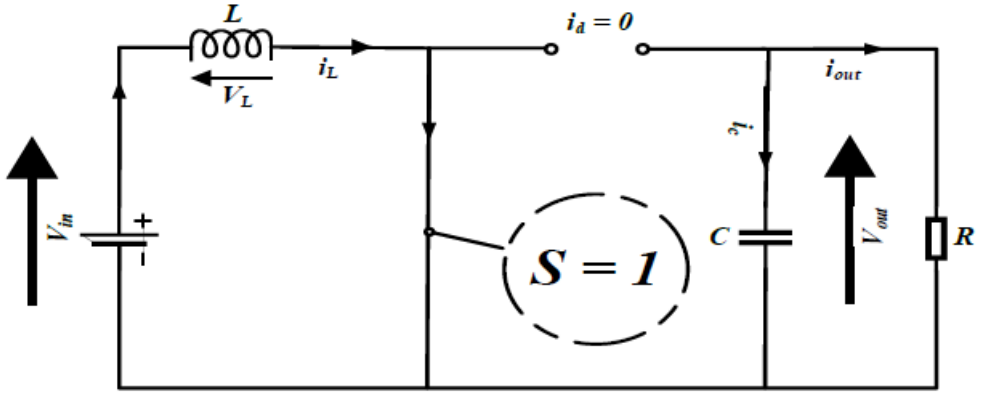

Fig.III.2: *Equivalent circuit of the classic boost converter when the switch is closed.*

When the switch position function is set to S=1, the following equations are obtained [62].

$$V_{in} = V_L = L\frac{di_L}{dt} \quad \text{(III.1)}$$

$$C\frac{dV_{out}}{dt} = -\frac{dV_{out}}{R} \quad \text{(III.2)}$$

$$y = C_1\begin{bmatrix} i_L \\ V_{out} \end{bmatrix} = Ri_c = CR\frac{dV_{out}}{dt} = -V_{out} \quad \text{(III.3)}$$

Using the matrix form, the above equations can be rewritten as:

$$\begin{bmatrix} \frac{di_L}{dt} \\ \frac{dV_{out}}{dt} \end{bmatrix} = \underbrace{\begin{bmatrix} 0 & 0 \\ 0 & \frac{-1}{RC} \end{bmatrix}}_{A_1}\begin{bmatrix} i_L \\ V_{out} \end{bmatrix} + \underbrace{\begin{bmatrix} \frac{1}{L} \\ 0 \end{bmatrix}}_{B_1} V_{in} \quad \text{(III.4)}$$

$$y = \underbrace{[0 \quad -1]}_{C_1}\begin{bmatrix} i_L \\ V_{out} \end{bmatrix} \quad \text{(III.5)}$$

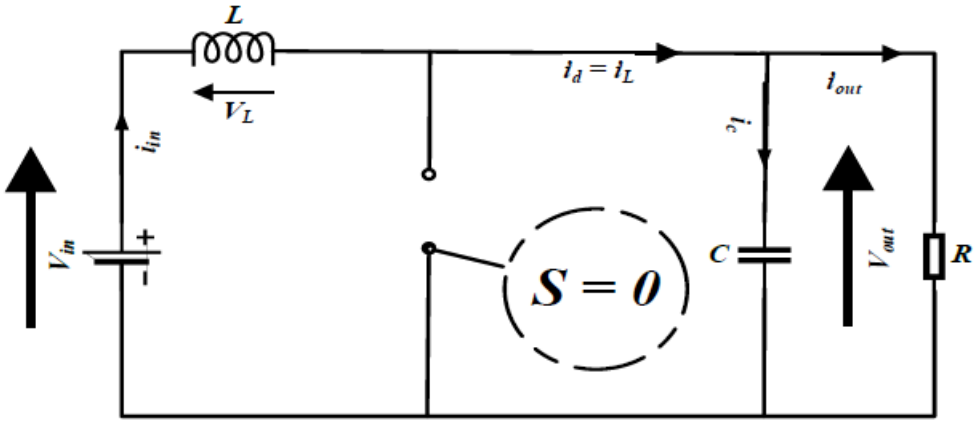

Fig.III.3*: Equivalent circuit of the classic boost converter when the switch is open.*

When the switch position function is set to S=0, the following equations are obtained:

$$\begin{cases} L\frac{di_L}{dt} = V_L = V_{in} - V_{out} \\ C\frac{dV_{out}}{dt} = i_c = i_L - i_{out} \end{cases} \quad \text{(III.6)}$$

$$y = V_{out} = Ri_{out} \quad \text{(III.7)}$$

$$i_{out} = i_L - i_c = i_L - C\frac{dV_{out}}{dt} = \frac{1}{R}V_{out} \quad \text{(III.8)}$$

Using the matrix form, the above equations can be rewritten as:

$$\begin{bmatrix} \frac{di_L}{dt} \\ \frac{dV_{out}}{dt} \end{bmatrix} = \underbrace{\begin{bmatrix} 0 & \frac{-1}{L} \\ \frac{1}{C} & \frac{-1}{RC} \end{bmatrix}}_{A_2} \begin{bmatrix} i_L \\ V_{out} \end{bmatrix} + \underbrace{\begin{bmatrix} \frac{1}{L} \\ 0 \end{bmatrix}}_{B_2} V_{in} \quad \text{(III.9)}$$

$$y = \underbrace{[0 \quad 1]}_{C_2} \begin{bmatrix} i_L \\ V_{out} \end{bmatrix} \quad \text{(III.10)}$$

Assuming the duty ratio of the converter is D ($0 \le D \le 1$), the state space average model can be expressed as:

$$\frac{dy}{dx} = [DA_1 + (1-D)A_2]x + [DB_1 + (1-D)B_2]V_{in} \quad \text{(III.11)}$$

$$y = [C_1 D + C_2(1-D)]x \quad \text{(III.12)}$$

Where $x = \begin{bmatrix} i_L \\ V_{out} \end{bmatrix}$; the detailed model of boost converter is expressed by:

$$\begin{cases} L\frac{di_L}{dt} = V_{in} - (1-D)V_{out} \\ C\frac{dV_{out}}{dt} = (1-D)i_L - i_{out} \end{cases} \quad \text{(III.13)}$$

With

$$i_{out} = \frac{V_{out}}{R}$$

$$y = [0 \quad (1-2D)] \begin{bmatrix} i_L \\ V_{out} \end{bmatrix} \quad \text{(III.14)}$$

To make controller design easier, switching converters which are nonlinear systems need to be linearized. One benefit of such a linearized model is that it is time invariant for a constant duty cycle. Only the DC components of the waveforms are

modeled, and there is no switching or switching ripple to control. To do this, a tiny signal model is obtained by linearizing and perturbing the average model around a quiescent operating point [63].

Introducing small AC perturbation and separation of AC and DC components, it yields:

$$V_{in} = v_{in} + \tilde{V}_{in} \quad \text{(III.15)}$$

$$x = X + \tilde{x} \quad \text{(III.16)}$$

$$D = D + \tilde{d} \quad \text{(III.17)}$$

$$D' = D' - \tilde{d} \rightarrow D' = 1 - D \quad \text{(III.18)}$$

By introducing these perturbations in (2.35), it yields:

$$\tilde{x} = A\tilde{x} + ((A_1 - A_2)x + (B_1 - B_2)V_{in})\tilde{d} + B\tilde{V}_{in} \quad \text{(III.19)}$$

Where :

$$A = A_1 D + A_2 D' \quad \text{(III.20)}$$

$$B = B_1 D + B_2 D' \quad \text{(III.21)}$$

$$A = \begin{bmatrix} 0 & -(1-D) \\ \frac{1-D}{C} & \frac{-1}{RC} \end{bmatrix}; B = \begin{bmatrix} \frac{1}{L} \\ 0 \end{bmatrix} \quad \text{(III.22)}$$

Finally, one can get:

$$\frac{d}{dt}\begin{bmatrix} \tilde{\imath}_L \\ \tilde{V}_{out} \end{bmatrix} = \begin{bmatrix} 0 & \frac{-(1-D)}{L} \\ \frac{1-D}{C} & -\frac{1}{RC} \end{bmatrix}\begin{bmatrix} \tilde{\imath}_L \\ \tilde{V}_{out} \end{bmatrix} + \begin{bmatrix} 0 & \frac{1}{L} \\ -\frac{1}{C} & 0 \end{bmatrix}\begin{bmatrix} i_L \\ V_{out} \end{bmatrix}\tilde{d} + \begin{bmatrix} \frac{1}{L} \\ 0 \end{bmatrix}\tilde{V}_{in} \quad \text{(III.23)}$$

where L, C, R denote the inductance of the input circuit, capacitance of the output filter and the output load resistance, respectively.

A voltage-controlled source at the low voltage side and a current-controlled source at the high voltage side basically replace the switch in the circuit depicted in Figure (III.4), which represents the averaged-value model of the boost converter.

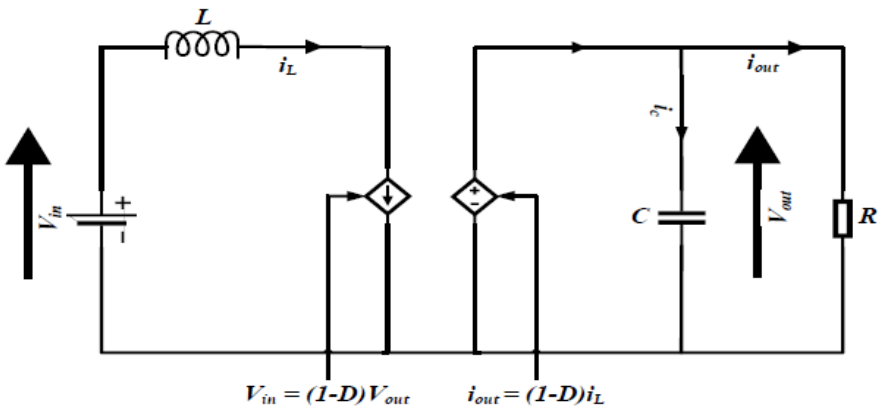

Fig.III.4: *Equivalent circuit of averaged-value boost converter.*

III.2.1.1.a.Sizing of inductance L and the capacitor C

When the switch is closed S=1, the inductance current is given by:

$$i_L(t) = \frac{V_{in}}{L}t + I_{Lmin} \quad \text{(III.24)}$$

The maximum value of the current is calculated by:

$$I_{Lmax} = i_L(DT_s) = \frac{V_{in}}{L}DT_s + I_{Lmin} \quad \text{(III.25)}$$

The current ripple is defined by*:*

$$\Delta i_L = \frac{V_{in}}{L}DT_s \quad \text{(III.26)}$$

When the switch is closed S=0, the inductance current is given by:

$$i_L(t) = -\frac{V_{out}}{L}t + I_{Lmax} \quad \text{(III.27)}$$

The minimum value of the current is calculated by:

$$I_{Lmin} = i_L\big((1-D)T\big) = -\frac{V_{out}}{L}(1-D)T_s + I_{Lmax} \quad \text{(III.28)}$$

The current ripple is defined by:

$$\Delta i_L = -\frac{V_{out}}{L}(1-D)T_s \quad \text{(III.29)}$$

As $V_{in} = (1-D)V_{out}$, one can write:

$$\Delta i_L = -\frac{V_{out}(1-D)D}{Lf} \quad \text{(III.30)}$$

From equation (III.30) and as the current ripple Δi_L is maximal for D = 0.5, the inductance L must satisfy the following inequality:

$$L \geq \frac{V_{out}}{4f_s\Delta i_L} \quad \text{(III.31)}$$

Where Δi_L is generally fixed in the interval of [1%i_L ,10%i_L].

III.2.1.1.b.Inductance value ensuring a continuous operation

In continuous mode, the current flowing through the inductor is not zero over a switching period *Ts* .

In this situation the mean boundary current flowing through the coil verifies:

$$\bar{\imath}_L = \frac{1}{T_s}\int_0^{T_s} i_L dt = \frac{i_{Lmax}}{2} = \frac{\Delta i_L}{2} \quad \text{(III.32)}$$

The continuous conduction limit being reached for $i_{Lmin} = 0$:

$$i_{Lmax} = \frac{V_{in}}{L} DT_s \quad \text{(III.33)}$$

The average value of inductance current becomes:

$$\bar{\imath}_L = \frac{V_{in}}{2L} \Delta T_s \quad \text{(III.34)}$$

And we have :

$$V_{in} = (1 - D)V_{out} \quad \text{(III.35)}$$

From (III.34) and (III.35), the average current of the inductance is expressed as follows:

$$\bar{\imath}_L = \frac{V_{out}(1-D)D}{2L} T_s \quad \text{(III.36)}$$

By replacing the duty cycle value D =1/2 in (III.36), the maximum value of the average current of the inductance $\bar{\imath}_{Lmax}$ can be calculated as follows :

$$\bar{\imath}_{Lmax} = \frac{V_{out}}{8L} T_s \quad \text{(III.37)}$$

The minimal value of the inductance, which guarantees that the converter always runs in the continuous conduction mode, can be determined using equation (III.37) . The following formula can be used to get this inductance's value:

$$L_{min} = \frac{V_{out}}{8\bar{\imath}_{Lmax}} T_s \quad \text{(III.38)}$$

With :

$$T_s = \frac{1}{f_s} \quad \text{(III.39)}$$

The voltage ripple across capacitor C can be calculated as follows:

$$\Delta V_{out} = \frac{\Delta Q}{C} = \frac{i_{out} D T_S}{C} \quad \text{(III.40)}$$

As $i_{out} = (1 - D) i_L$, we can write :

$$\Delta V_{out} = \frac{\bar{\imath}_L (1-D) D}{Cf} \quad \text{(III.41)}$$

Equation (III.41) can be used to calculate the value of the capacitor as follows:

$$C = \frac{\bar{\imath}_L (1-D) D}{f \Delta V_{out}} \quad \text{(III.42)}$$

Where , ΔV_{out} is generally fixed in the interval of $[5\% V_{out}, 20\% V_{out}]$.

III.2.1.2. Control of boost converter

Maintaining a steady bus voltage and/or current in spite of changes in the input (fuel cell, battery, or supercapacitor) and the load is the goal of converter control [60]. The system current should be regulated because the control system must safeguard power components like switches, which are susceptible to overcurrent [64].

Simple PI controllers can be used to regulate the converter's reduction to first order transfer functions.

- **Voltage control**

A proportional-integral (PI) type regulator is used to modify the converter's output voltage (load voltage), and its transfer function is represented by $C_v(s)$. The reference current to be applied to capacitor C is provided by the output of this regulator. The voltage controller's transfer function is provided by:

$$C_v(s) = \frac{K_{p_v} s + K_{i_v}}{s} \quad \text{(III.43)}$$

The capacitor voltage in Laplace domain is given by:

$$V_{out} = \frac{(1-D) i_L - i_{out}}{CS} \quad \text{(III.44)}$$

Figure (III.5) shows the boost converter output voltage regulation loop.

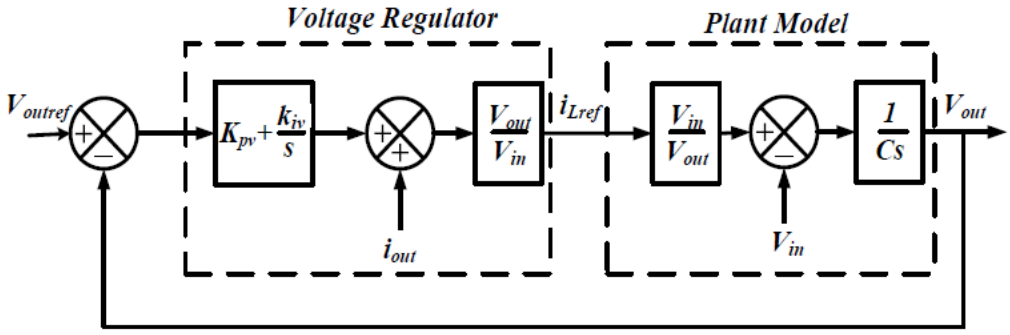

Fig.III.5: *Voltage regulator of the boost converter.*

The closed loop transfer function is given by:

$$B_{v_{close}}(s) = \frac{\frac{K_{p_v}}{C}s+\frac{K_{i_v}}{C}}{s^2+\frac{K_{p_v}}{C}s+\frac{K_{i_v}}{C}} \quad \text{(III.45)}$$

To calculate the PI regulator gains (K_{p_v} and K_{i_v}) , the pole placement method is used . We want that the transfer function (III.45) exhibits the same dynamic behavior as a second-order system of the following function :

$$H_v(s) = \frac{\omega_{vn}^2}{s^2+2\xi_v\omega_{vn}+\omega_{vn}^2} \quad \text{(III.46)}$$

The proportional gain K_{p_v} and integral gain K_{i_v} are determined by identifying term by term the tow characteristic equations of (III.45) and (III.46) , which result in :

$$\begin{cases} K_{p_v} = 2\xi_v\omega_{vn}C \\ K_{i_v} = \omega_{vn}^2 C \end{cases} \quad \text{(III.47)}$$

where ω_{vn} is the natural frequency and $\xi_v$is the damping coefficient.

- **Current control**

The error between the measured currents and their reference can be corrected by a proportional-integral (PI) type regulator, whose transfer function is represented by $C_i(s)$. Each regulator's output enables the determination of the voltage reference that should be applied to the indictor's terminals.

The transfer function of current controller is given by:

$$C_i(s) = \frac{K_{p_i}s+K_{i_i}}{s} \quad \text{(III.48)}$$

The inductor current in Laplace domain are given by:

$$I_L = \frac{V_{in}-(1-D)V_{out}}{LS} \quad \text{(III.49)}$$

Figure (III.6) shows the boost converter output current regulation loop.

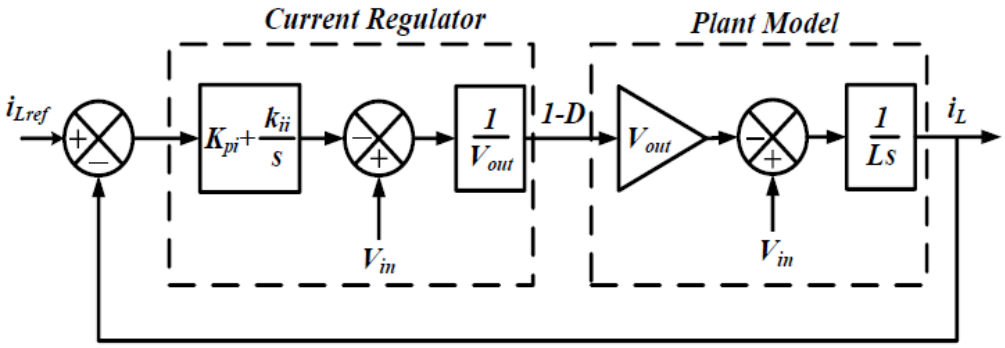

Fig.III.6: *Current regulator of the boost converter.*

The closed loop transfer function is given by:

$$B_{i_{close}}(s) = \frac{\frac{K_{p_i}}{L}s+\frac{K_{i_i}}{L}}{s^2+\frac{K_{p_i}}{L}s+\frac{K_{i_i}}{L}} \quad \text{(III.50)}$$

To calculate the PI regulator gains (K_{p_v} *and* K_{i_v}) , the closed loop transfer function (III.50) has to exhibit the same dynamic behavior as a second-order defined by the following transfer function :

$$H_i(s) = \frac{\omega_{vn}^2}{s^2+2\xi_v\omega_{vn}+\omega_{vn}^2} \quad \text{(III.51)}$$

The proportional gain K_{p_i} and integral gain K_{i_i} are determined by identifying term by term the tow characteristic equations of (III.50) and (III.51) , which result in :

$$\begin{cases} K_{p_i} = 2\xi_i\omega_{in}L \\ K_{i_i} = \omega_{in}^2 L \end{cases} \quad \text{(III.52)}$$

where ω_{in} is the natural frequency and $\xi_i$is the damping coefficient.

III.2.2. DC-DC Buck converter model and control

III.2.2.1.Model of Buck converter

The Buck converter, which is a straightforward and popular voltage step-down device with great efficiency, is shown in Figure (III.7) A buck converter usually consists of a switching element like a MOSFET or an IGBT and a filter made up of an

inductor and a capacitor. The on-state and off-state of the switch S are the two states in which the buck converter operates.

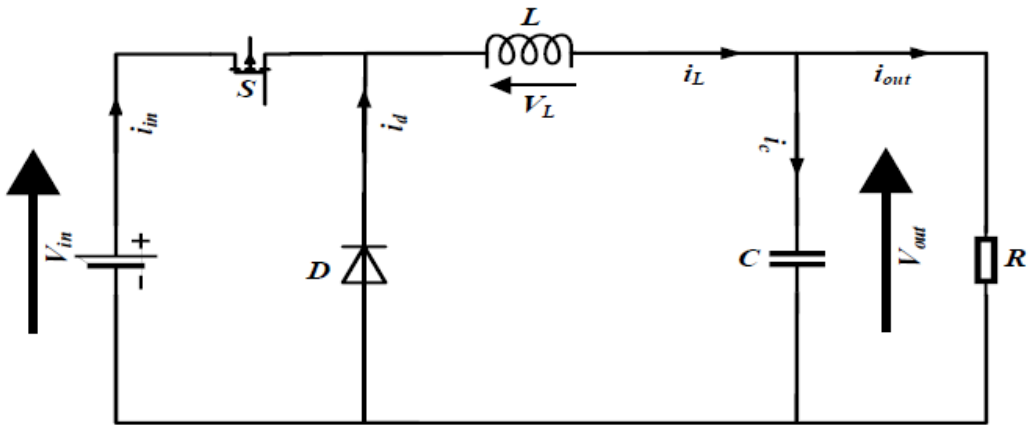

Fig.III.7: *Structure of a buck converter.*

As shown in Figure (III.8), when the switch is closed, the current flowing through the inductor increases linearly. The diode is reverse biased and there is no current flowing through it.

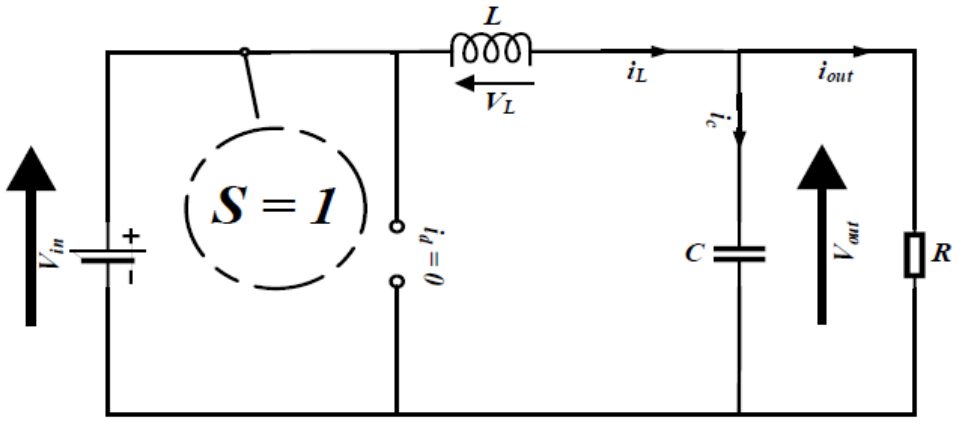

Fig.III.8: *Equivalent circuit of the buck converter when the switch is closed.*

When the switch position is set to S=1, the following equations are obtained:

$$\begin{cases} L\frac{di_L}{dt} = V_{in} - V_{out} = V_L \\ C\frac{dV_{out}}{dt} = i_c = i_L - \frac{V_{out}}{R} \end{cases} \quad \text{(III.53)}$$

$$y = V_{out} = Ri_{out} \quad \text{(III.54)}$$

$$i_{out} = i_L - i_c = i_L - C\frac{dV_{out}}{dt} = \frac{1}{R}V_{out} \quad \text{(III.55)}$$

These equations can be rewritten in the following matrix from:

$$\begin{bmatrix} \frac{di_L}{dt} \\ \frac{dV_{out}}{dt} \end{bmatrix} = \underbrace{\begin{bmatrix} 0 & \frac{-1}{L} \\ \frac{1}{C} & \frac{-1}{RC} \end{bmatrix}}_{A_1} \begin{bmatrix} i_L \\ V_{out} \end{bmatrix} + \underbrace{\begin{bmatrix} \frac{1}{L} \\ 0 \end{bmatrix}}_{B_1} V_{in} \quad \text{(III.56)}$$

$$y = \underbrace{[0 \quad 1]}_{C_2} \begin{bmatrix} i_L \\ V_{out} \end{bmatrix} \quad \text{(III.57)}$$

When switch S is opened, the inductor functions as a source and keeps current flowing through a load resistor, as seen in Figure (III.9). The current keeps flowing via diode D in the inductor during this time. Both the energy stored in the inductor and the current flowing through it decrease when the magnetic field weakens. In continuous mode, diode D is opened prior to the inductor being fully depleted, and switch S is closed.

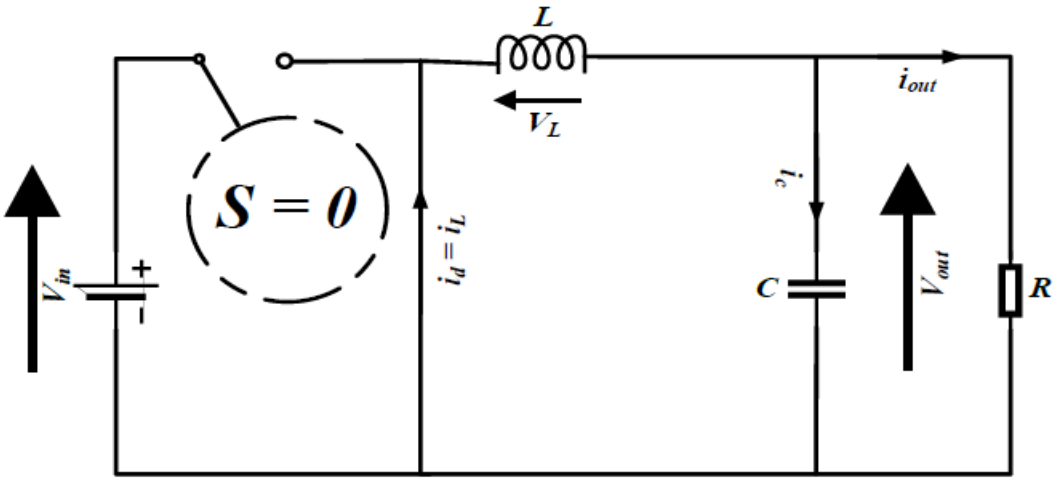

Fig.III.9: *Equivalent circuit of the buck converter when the switch is open.*

When the switch position is set to S=0, the following equations are obtained:

$$\begin{cases} L\frac{di_L}{dt} = V_L = -V_{out} \\ C\frac{dV_{out}}{dt} = i_c = i_L - \frac{V_{out}}{R} \end{cases} \quad \text{(III.58)}$$

$$y = V_{out} = Ri_{out} \quad \text{(III.59)}$$

$$i_{out} = i_L - i_c = i_L - C\frac{dV_{out}}{dt} = \frac{1}{R}V_{out} \quad \text{(III.60)}$$

These equations can be rewritten in the following matrix from:

$$\begin{bmatrix} \frac{di_L}{dt} \\ \frac{dV_{out}}{dt} \end{bmatrix} = \underbrace{\begin{bmatrix} 0 & \frac{-1}{L} \\ \frac{1}{C} & \frac{-1}{RC} \end{bmatrix}}_{A_2} \begin{bmatrix} i_L \\ V_{out} \end{bmatrix} + \underbrace{\begin{bmatrix} 0 \\ 0 \end{bmatrix}}_{B_2} V_{in} \quad \text{(III.61)}$$

$$y = \underbrace{[0 \quad 1]}_{C_2} \begin{bmatrix} i_L \\ V_{out} \end{bmatrix} \tag{III.62}$$

Combining (2.83) with (2.78) and (2.84) with (2.79), state space average model can be obtained by:

$$\frac{dy}{dx} = [DA_1 + (1-D)A_2]x + [DB_1 + (1-D)B_2]V_{in} \tag{III.63}$$

$$y = [C_1 D + C_2(1-D)]x \tag{III.64}$$

Where $x = \begin{bmatrix} i_L \\ V_{out} \end{bmatrix}$ Is the state space vector and D is the duty cycle.

The detailed model of buck converter is expressed by:

$$\begin{cases} L\frac{di_L}{dt} = DV_{in} - V_{out} \\ C\frac{dV_{out}}{dt} = i_L - i_{out} \end{cases} \tag{III.65}$$

$$y = [0 \quad 1] \begin{bmatrix} i_L \\ V_{out} \end{bmatrix} \tag{III.66}$$

The final averaged model exhibits nonlinear and time-invariant behavior. To derive a small-signal representation, the model is linearized around a specific operating point. This procedure yields a linear time-invariant (LTI) small-signal model, as detailed in [65].

Introducing small perturbation, it yields:

$$V_{in} = v_{in} + \tilde{V}_{in} \tag{III.67}$$

$$x = X + \tilde{x} \tag{III.68}$$

$$D = D + \tilde{d} \tag{III.69}$$

$$D' = D' - \tilde{d} \rightarrow D' = 1 - D \tag{III.70}$$

By replacing these perturbations in equation (2.85), it yields:

$$\dot{\tilde{x}} = A\tilde{x} + ((A_1 - A_2)x + (B_1 - B_2)V_{in})\tilde{d} + B\tilde{V}_{in} \tag{III.71}$$

Where

$$A = A_1 D + A_2 D' \tag{III.72}$$

$$B = B_1 D + B_2 D' \tag{III.73}$$

$$A = \begin{bmatrix} 0 & -\frac{1}{L} \\ \frac{1}{C} & \frac{-1}{RC} \end{bmatrix}; B = \begin{bmatrix} \frac{1}{L} \\ 0 \end{bmatrix} \quad \text{(III.74)}$$

The following equation represents the small signal model.

$$\frac{d}{dt}\begin{bmatrix} \tilde{\imath}_L \\ \tilde{V}_{out} \end{bmatrix} = \begin{bmatrix} 0 & -\frac{1}{L} \\ \frac{1}{C} & -\frac{1}{RC} \end{bmatrix}\begin{bmatrix} \tilde{\imath}_L \\ \tilde{V}_{out} \end{bmatrix} + \begin{bmatrix} \frac{1}{L} \\ 0 \end{bmatrix}\tilde{V}_{in}\tilde{d} + \begin{bmatrix} \frac{1}{L} \\ 0 \end{bmatrix}\tilde{V}_{in} \quad \text{(III.75)}$$

Figure (III.10) shows the block diagram of the buck averaged-value model.

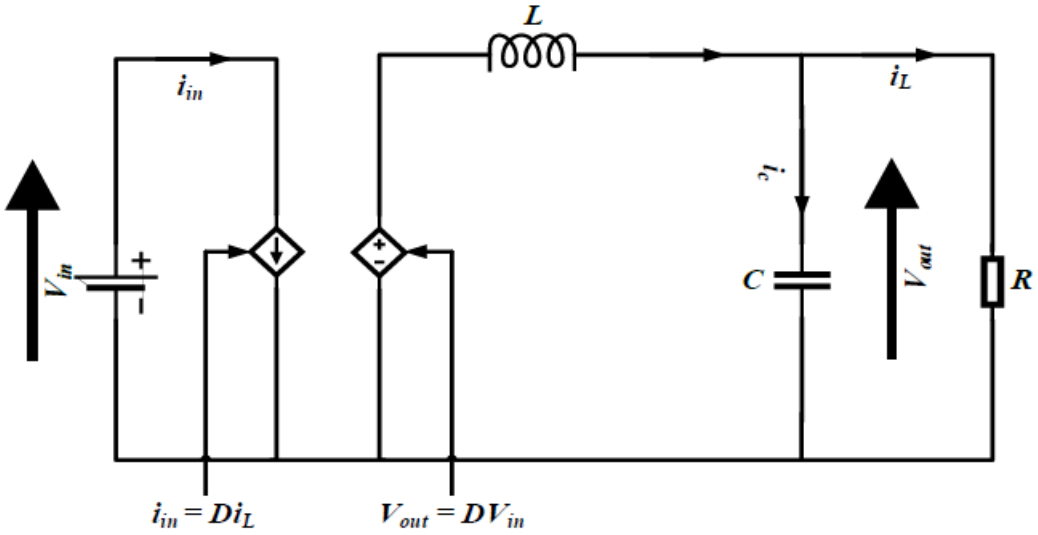

Fig.III.10: *Equivalent circuit of averaged-value buck converter.*

III.2.2.1.a .Sizing of inductance L and the capacitor C

The LC filter is used to smooth the output voltage and current ripples.

When the switch is closed S=1, the inductance current is expressed by:

$$i_L(t) = \frac{V_{in}-V_{out}}{L}t + I_{Lmin} \quad \text{(III.76)}$$

This current reaches its maximum at $t = DTs$, which results in:

$$I_{Lmax} = i_L(DT_s) = \frac{V_{in}-V_{out}}{L}DT_s + I_{Lmin} \quad \text{(III.77)}$$

The current ripple Δi_L is the difference between the maximum and the minimum values of the inductance current as in:

$$\Delta i_L = I_{Lmax} - I_{Lmin} = \frac{V_{in}-V_{out}}{L}DT_s \quad \text{(III.78)}$$

When the switch is open S=0, the inductance current is expressed by:

$$i_L(t) = -\frac{V_{out}}{L}t + I_{Lmax} \quad \text{(III.79)}$$

This current reaches its maximum at $t = (1 - D)Ts$, which results in:

$$I_{Lmin} = i_L\big((1-D)T\big) = -\frac{V_{out}}{L}(1-D)T_s + I_{Lmax} \quad \text{(III.80)}$$

In this case, the current ripple Δi_L is calculated by:

$$\Delta i_L = -\frac{V_{out}}{L}(1-D)T_s \quad \text{(III.81)}$$

The current ripple is directly proportional to the duty-cycle and inversely proportional to the inductance, as can be seen from equations (III.78) and (III.81). Therefore, choosing the right inductor can control the current ripple.

he expressions for the maximum and minimum inductor currents are written as:

$$I_{Lmax} = I_{out} + \frac{\Delta i_L}{2} = \frac{V_{out}}{R} + \frac{V_{out}}{2L}(1-D)T_s \quad \text{(III.82)}$$

$$I_{Lmin} = I_{out} - \frac{\Delta i_L}{2} = \frac{V_{out}}{R} - \frac{V_{out}}{2L}(1-D)T_s \quad \text{(III.83)}$$

There is always a non-null current flowing through the inductor while the buck converter is in the continuous conduction mode. Imposing IL min 0 will yield the minimum inductor value that guarantees continuous conduction mode. Thus, it leads to :

$$L_{min} = \frac{(1-D)}{2}RT_s = \frac{(1-D)}{2f_s}R = \frac{(1-0.5)}{2\times 25000} \times 10 = 0.0001H \quad \text{(III.84)}$$

The output voltage ripples depend on the capacitor connected to the load. The voltage ripple ΔV_c is written as:

$$\Delta V_{out} = \frac{\Delta Q}{C} = \frac{\Delta I_L T_s}{8C} = \frac{V_{out}(1-D)T_s^2}{8LC} \quad \text{(III.85)}$$

Therefore :

$$C = \frac{V_{out}(1-D)T_s^2}{8L\Delta V_{out}} = 2.7 \times 10^{-6}F \quad \text{(III.86)}$$

With $\Delta V_{out} = 5\% V_{out}$

III.2.2.2. Control of buck converter

By adjusting the duty cycle D_{Buck}, the current flowing through the indictor is indirectly controlled. This is accomplished by subtracting the current from its reference value. A PI compensator whose output matches the duty cycle D_{Buck} cancels out the ensuing mistake. DC voltage regulation is carried out similarly.

Simple PI regulators can be used to control the converter's first order transfer functions.

- **Voltage control**

A proportional-integral (PI) controller is employed to regulate the converter's output voltage. The controller's output determines the reference value for the capacitor current.

The transfer function of voltage controller is given by:

$$C_v(s) = \frac{K_{pv}s + K_{iv}}{s} \quad \text{(III.87)}$$

The capacitor voltage in Laplace domain is given by:

$$V_{out} = \frac{i_L - i_{out}}{CS} \quad \text{(III.88)}$$

Figure (III.11) represents block diagram of the output voltage regulation loop of the buck converter.

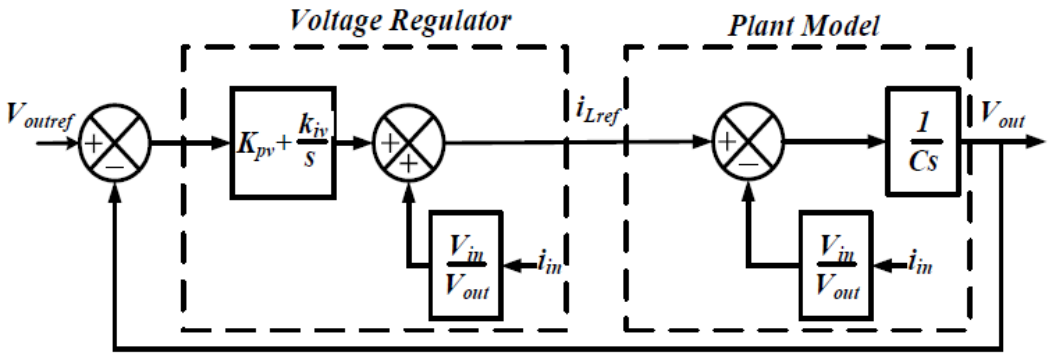

Fig.III.11: *Voltage control of the buck converter.*

From the diagram in Figure (III.11), the closed loop transfer function is written as:

$$H_{v_{close}}(s) = \frac{\frac{K_{pv}}{C}s + \frac{K_{iv}}{C}}{s^2 + \frac{K_{pv}}{C}s + \frac{K_{iv}}{C}} \quad \text{(III.89)}$$

To calculate the gains of the voltage regulator, the transfer function (III.89) has to exhibit the same dynamic behavior as a second-order system of the following transfer function:

$$H_v(s) = \frac{\omega_{vn}^2}{s^2 + 2\xi_v\omega_{vn} + \omega_{vn}^2} \quad \text{(III.90)}$$

The proportional gain K_{p_v} and integral gain K_{i_v} are determined by identifying term by term the tow characteristic equations of (III.89) and (III.90) , which result in :

$$\begin{cases} K_{p_v} = 2\xi_v \omega_{vn} C \\ K_{i_v} = \omega_{vn}^2 C \end{cases} \quad \text{(III.91)}$$

where ω_{vn} is the natural frequency and $\xi_v$is the damping coefficient.

- **Current control**

Figure (III.11) represents block diagram of the inductance current control loop of the buck converter. Using Laplace transform, the inductor current is given by:

$$I_L = \frac{DV_{in} - V_{out}}{LS} \quad \text{(III.92)}$$

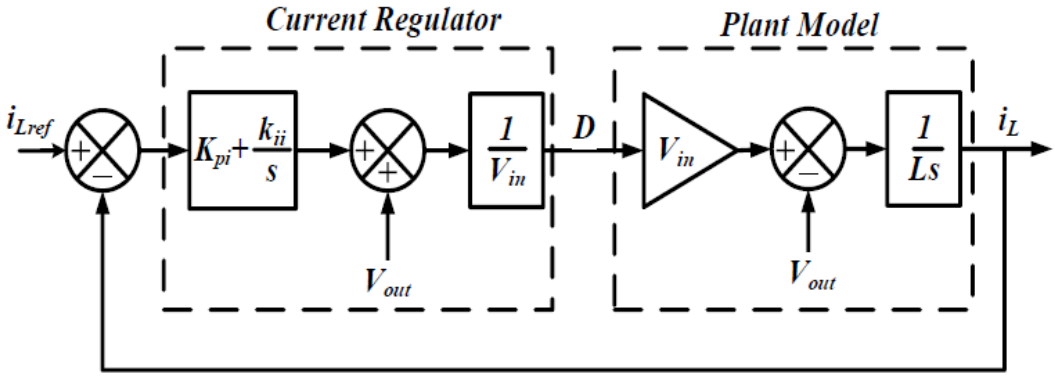

Fig.III.12: *Current control of the buck converter.*

From the diagram in Figure (III.12), the closed loop transfer function is written as:

$$H_{i_{close}}(s) = \frac{\frac{K_{p_i}}{L}s + \frac{K_{i_i}}{L}}{s^2 + \frac{K_{p_i}}{L}s + \frac{K_{i_i}}{L}} \quad \text{(III.93)}$$

To calculate the gains of the PI regulator, the transfer function (III.93) has to exhibit the same dynamic behavior as a second-order system of the following transfer function:

$$H_i(s) = \frac{\omega_{vn}^2}{s^2 + 2\xi_v \omega_{vn} + \omega_{vn}^2} \quad \text{(III.94)}$$

The proportional gain K_{p_i} and integral gain K_{i_i} are determined by identifying term by term the tow characteristic equations of (III.93) and (III.94) , which result in :

$$\begin{cases} K_{p_i} = 2\xi_i \omega_{in} L \\ K_{i_i} = \omega_{in}^2 L \end{cases}$$

where ω_{in} is the natural frequency and $\xi_i$is the damping coefficient.

III.2.3. Bidirectional DC-DC converter modeling

In this study, the average model of the bidirectional DC-DC converter is obtained jut by connecting in parallel the boost and buck converters as shown in Figure (III.13), in which each converter is modeled in its turn by its average model.

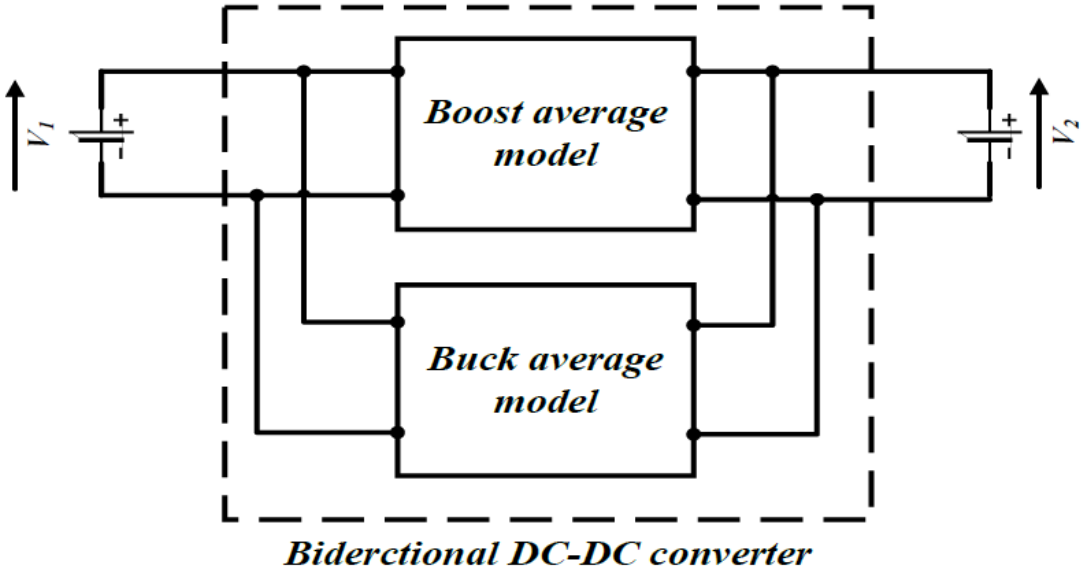

Fig.III.13: *Equivalent circuit of the averaged model of the bidirectional DC-DC converter.*

III.3. DC Microgrid modeling and control

Hybrid photovoltaic (PV) battery in DC microgrids offer enhanced power conversion and distribution efficiency. In this microgrid systems, battery is critical since they is responsible for lightening the difference between generation and consumption, serving the dual function, which supplying energy during generation-consumption deficits and absorbing excess energy. However, these advanced systems present significant control challenges due to complex dynamic interactions between DC microgrid voltage, PV, and battery output currents, especially under system disturbances like irradiance variations, PV cell temperature changes, and load fluctuations[66].

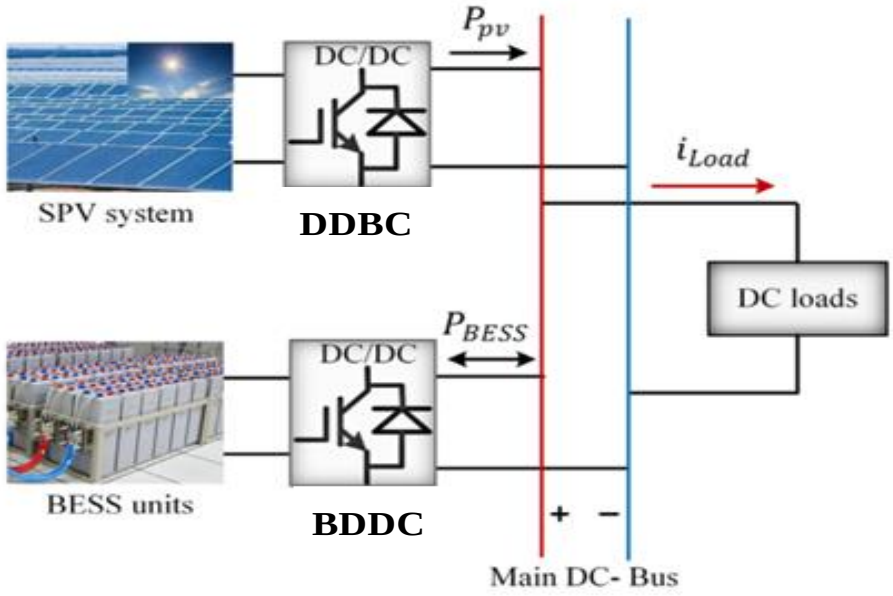

Fig.III.14 *: Schematic diagram of a DC microgrid based on PV with battery.*

III.3.1. Modeling and control of boost converter for PV array

The figure (III.15) show the detailed model of boost converter for PV . So with using of Kirchhoff's law we can find the dynamics of both the voltage of PV and input current of boost converter.

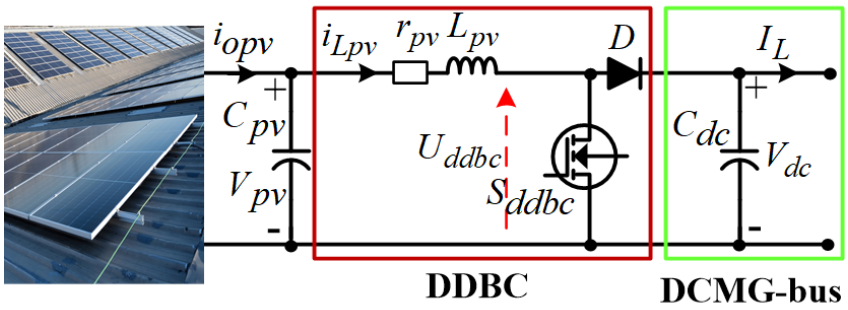

Fig.III.15*:Schematic circuit of the boost converter for PV.*

III.3.1.1. Dynamics of PV voltage

According to the figure (III.15) we can get :

$$\frac{dV_{pv}}{dt} = \frac{1}{C_{pv}} i_{Cpv} = \frac{1}{C_{pv}} \left(i_{opv} - i_{Lpv}\right) \qquad \text{(III.95)}$$

where i_{opv} and i_{Lpv} indicate the PV output current and boost converter input inductance filter current, respectively; and C_{pv} is the PV output capacitor and i_{Cpv} indicates its current. The PV output filter capacitance (C_{pv}) is essential for BOOST CONVERTER

input current reference estimation, voltage regulation, and ripple attenuation of the PV output voltage (V_{pv}).

III.3.1.2. Dynamics of the input boost converter current

And according to the figure (III.15),we can get also :

$$\frac{di_{Lpv}}{dt} = \frac{1}{L_{pv}}(V_{pv} - U_{ddbc} - r_{pv}i_{Lpv}) \quad \text{(III.96)}$$

Where L_{pv} is the boost converter inductance filter and r_{pv} is its resistance.

And we have :

$$U_{ddbc} = (1 - D_{ddbc})V_{dc} \quad \text{(III.97)}$$

Where D_{ddbc} is the cyclical report of the BOOST CONVERTER.

Substituting (III.97) in (III.96) , we find

$$\frac{di_{Lpv}}{dt} = \frac{1}{L_{pv}}\left(V_{pv} - V_{dc} + D_{ddbc}V_{dc} - r_{pv}i_{Lpv}\right) \quad \text{(III.98)}$$

III.3.1.3. Control of boost converter-based PV

In the control of boost converter for PV applications, a double-loop control strategy is commonly employed to enhance system performance, stability, and dynamic response. This structure consists of two main loops: an inner current control loop for regulating the boost converter input current (inductor current) and an outer voltage control loop for regulating the voltage of the PV.

- **PV voltage control loop**

The outer loop regulates the voltage of PV (V_{pv}). This loop operates at a slower bandwidth than the inner loop and generates the boost converter input current reference i_{ref} for the inner loop.

In MPPT-based systems, the outer loop ensures that the PV panel operates at its maximum power point by adjusting the voltage reference V_{pvref}. The outer loop's main objective is to maintain the desired voltage level, contributing to the overall power balance and energy efficiency of the system. In this control loop , we use an regulator PI as follows :

From the circuit in the figure (III.15). we have:

$$i_{Lpv} = i_{pv} - i_{Cpv} \tag{III.99}$$

Where

$$i_{Cpv} = C_{pv} \frac{dV_{pv}}{dt} \tag{III.100}$$

Substituting (III.100) in (III.99) , we find :

$$C_{pv} \frac{dV_{pv}}{dt} = i_{pv} - i_{Cpv} \tag{III.101}$$

using Laplace transform , equation (III.100) becomes :

$$i_{Cpv} = C_{pv} s \, V_{pv} \tag{III.102}$$

The transfer function of the PV-output capacitor system is given by :

$$\frac{V_{pv}}{I_{Cpv}} = \frac{1}{C_{pv} s} \tag{III.103}$$

From this transfer function it can be seen that the regulation of the PV output voltage can provids the PV output capacitor reference current (i^*_{Cpv}) , and using the PV output current as feedforword, we obtain the input current reference of the boost converter.

The schematic of the PI-based outer PV voltage loop is given as in the figure (III.16).

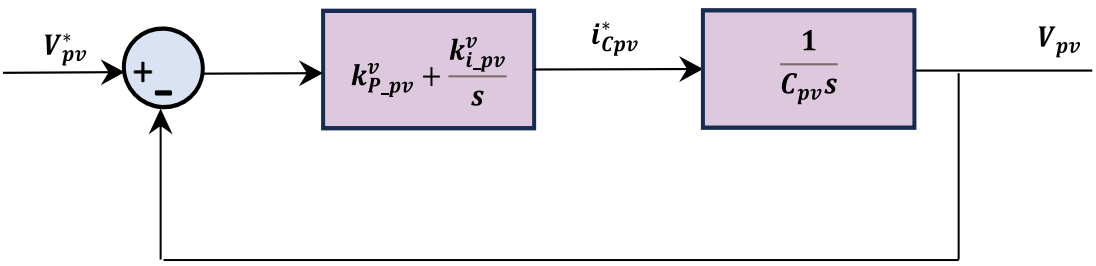

Fig.III.16: *The schematic of the PI within the PV voltage control loop.*

According to the schematic of the PI within the outer PV voltage control loop in figure (III.16) and equation (III.99), we obtain the input current reference of the boost converter as follows :

$$i^*_{Lpv} = i_{pv} - i^*_{Cpv} \tag{III.104}$$

The parametres of the PI regulator ($k^v_{P_pv}$and $k^v_{i\_pv}$) in this control loop are determied using the pols placement method as follows :

From the diagram in Figure (III.16), the closed loop transfer function is written as:

$$F_{pv_{close}}(s) = \frac{\frac{k_{P\_pv}^{v}}{C_{pv}}s + \frac{k_{i\_pv}^{v}}{C_{pv}}}{s^2 + \frac{k_{P\_pv}^{v}}{C_{pv}}s + \frac{k_{i\_pv}^{v}}{C_{pv}}} \quad \text{(III.105)}$$

To calculate the gains of the voltage regulator, the transfer function (III.105) has to exhibit the same dynamic behavior as a second-order system of the following transfer function:

$$H_v^{pv}(s) = \frac{(\omega_{nv}^{pv})^2}{s^2 + 2\xi_v^{pv}\omega_{nv}^{pv} + (\omega_{nv}^{pv})^2} \quad \text{(III.106)}$$

The proportional gain K_{p_v} and integral gain K_{i_v} are determined by identifying term by term the tow characteristic equations of (III.105) and (III.106) , which result in :

$$\begin{cases} K_{p_v} = 2\xi_v^{pv}\omega_{nv}^{pv}C_{pv} \\ K_{i_v} = (\omega_{nv}^{pv})^2 C_{pv} \end{cases} \quad \text{(III.107)}$$

where ω_{nv}^{pv} is the natural frequency and ξ_v^{pv} is the damping coefficient.

- **Boost converter input current control loop**

The inner loop is responsible for regulating the input current of the boost converter (i_{Lpv}). It is designed with fast dynamic response, as the current changes more rapidly than voltage. This loop ensures that the inductor current accurately tracks a reference signal provided by the outer loop. By controlling the current directly, it improves system stability, enhances disturbance rejection, and ensures better transient performance.

The output of this loop is typically the duty cycle D_{ddbc} of the boost converter's switching device. We use an regulator PI as follows :

From the circuit in the figure (III.15). we have:

$$U_{ddbc} = V_{pv} - U_{Lpv} \quad \text{(III.108)}$$

Where:

$$U_{Lpv} = L_{pv}\frac{di_{Lpv}}{dt} \quad \text{(III.109)}$$

Substituting (III.109) in (III.108) , we find :

$$L_{pv}\frac{di_{Lpv}}{dt} = V_{pv} - U_{ddbc} \quad \text{(III.110)}$$

Using Laplace transform; equation (III.109) becomes :

$$U_{Lpv} = L_{pv}s\, i_{Lpv} \quad \text{(III.111)}$$

The transfer function of the boost converter-input inductor system is given by:

$$\frac{i_{Lpv}}{U_{Lpv}} = \frac{1}{L_{pv}s} \quad \text{(III.112)}$$

From this transfer function it can be seen that the regulation of the input current of the boost converter can provids the inductor voltage reference of this converter (U^*_{Lpv}), and using the PV output voltage as feedforword, we obtain the input voltage reference of the boost converter.

The schematic diagram of the PI-based input boost converter current control loop is given as in the figure (III.17).

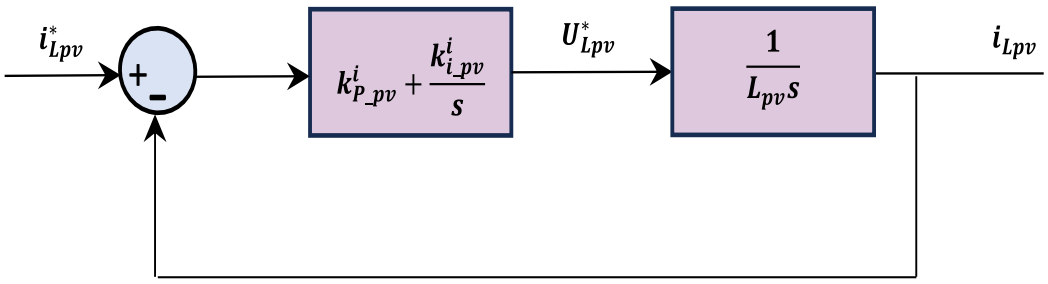

Fig.III.17: *The schematic of the PI-based input boost converter current control loop.*

According to the schematic of the PI-based input boost converter current control loop in figure (III.17) and equation (III.108). we obtain the boost converter input voltage reference as follows:

$$U^*_{ddbc} = V_{pv} - U^*_{Lpv} \quad \text{(III.113)}$$

The parametres of the PI regulator ($k^i_{P_pv}$and $k^i_{i\_pv}$) in this control loop are determied using the pols placement method as follows :

From the diagram in Figure (III.17), the closed loop transfer function is written as:

$$F_{pv_{close}}(s) = \frac{\frac{k^i_{P\_pv}}{L_{pv}}s + \frac{k^i_{i\_pv}}{L_{pv}}}{s^2 + \frac{k^i_{P\_pv}}{L_{pv}}s + \frac{k^i_{i\_pv}}{L_{pv}}} \quad \text{(III.114)}$$

To calculate the gains of the current regulator, the transfer function (III.114) has to exhibit the same dynamic behavior as a second-order system of the following transfer function:

$$H_v^{pv}(s) = \frac{(\omega_{ni}^{pv})^2}{s^2+2\xi_i^{pv}\omega_{ni}^{pv}+(\omega_{ni}^{pv})^2} \quad \text{(III.115)}$$

The proportional gain K_{p_i} and integral gain K_{i_i} are determined by identifying term by term the tow characteristic equations of (III.114) and (III.115) , which result in :

$$\begin{cases} K_{p_i} = 2\xi_i^{pv}\omega_{ni}^{pv}L_{pv} \\ K_{i_i} = (\omega_{ni}^{pv})^2 L_{pv} \end{cases} \quad \text{(III.116)}$$

where ω_{ni}^{pv} is the natural frequency and ξ_i^{pv} is the damping coefficient.

And from the same circuit we find as in figure (III.15) :

If the switch $S = 0$; $U_{ddbc} = V_{dc}$ else $S = 1$; $U_{ddbc} = 0$.

So :

$$U_{ddbc} = (1 - D)\, V_{dc} \quad \text{(III.117)}$$

Substituting (III.107) in (III.101) , we get :

$$U_L^* = L_{pv}\frac{di_{Lpv}}{dt} = V_{pv} - (1 - D)\, V_{dc} \quad \text{(III.118)}$$

So the duty cycle becomes :

$$D_{ddbc} = \frac{U_L^* - V_{pv}}{V_{dc}} + 1 \quad \text{(III.119)}$$

This hierarchical control strategy allows for precise control of power flow and voltage levels while ensuring the converter operates efficiently and stably under varying load and environmental conditions.

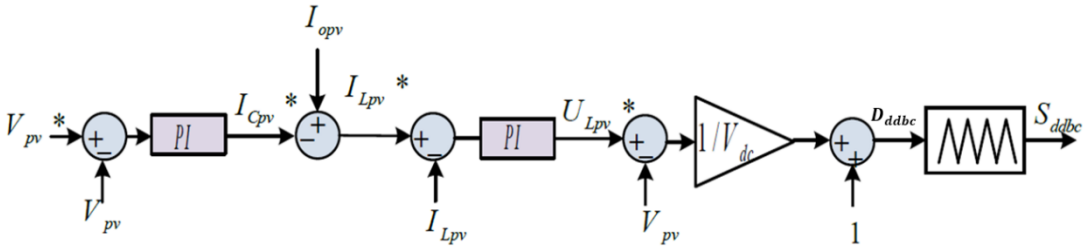

Fig.III.18:*Regulation of both the PV output voltage and boost converter input current using PI controllers.*

III.3.2. Bidirectional dc-dc converter-based battery Modeling and control

Figure (III.19) show the detailed model of bidirectional dc-dc converter-based battery. So with using of Kirchhoff's law we can find the DC Microgrid voltage dynamics and the output current of battery.

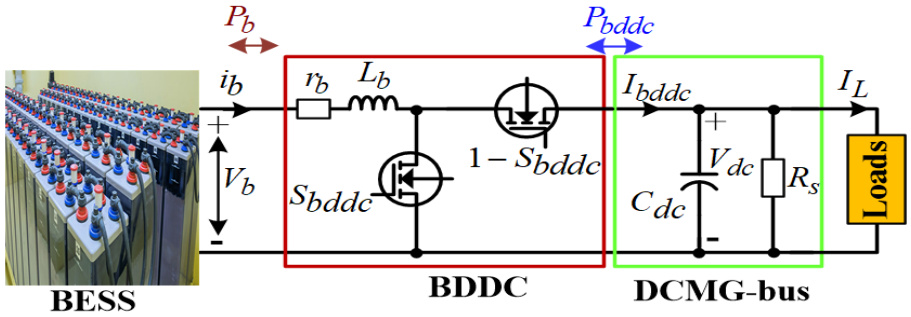

Fig.III.19:*Equivalent schematic diagram of the bidirectional dc-dc converter-based battery.*

III.3.2.1. The dynamics DC voltage

According to the figure (III.19) we can get :

$$\frac{dV_{dc}}{dt} = \frac{1}{C_{dc}} i_{Cdc} = \frac{1}{C_{dc}} \left(i_{bddc} + i_{ddbc} - \frac{V_{dc}}{R_{loss}} - I_L \right) \qquad \text{(III.120)}$$

where i_{Cdc}, i_{bddc}, and i_{ddbc} denote the microgrid-bus capacitor current, the bidirectional dc-dc converter output current, and the boost converter outputcurrent, respectively. I_L represents the current consumed by the DC loads connected to the microgrid-bus, and $\frac{V_{dc}}{R_{loss}}$ represents the bidirectional dc-dc converter switching and its input inductance filter power losses.

III.3.2.2. Dynamics of battery output current

And according to the figure (III.19),we can get also :

$$\frac{di_b}{dt} = \frac{1}{L_b}(V_b - r_b i_b - U_{bddc}) \quad \text{(III.121)}$$

And we have :

$$U_{bddc} = (1 - D_{bddc})V_{dc} \quad \text{(III.122)}$$

Where D_{bddc} is the cyclical report of the bidirectional dc-dc converter.

$$\frac{di_b}{dt} = \frac{1}{L_b}(V_b - r_b i_b - D_{bddc}V_{dc}) \quad \text{(III.123)}$$

III.3.2.3.Control of bidirectional dc-dc converter

The integration of a Battery into a DC microgrid is typically achieved using a bidirectional DC-DC converter. To ensure reliable and stable power exchange between the battery and the DC bus, a double-loop control structure is implemented, consisting of an current control loop and an voltage control loop.

- **DC voltage loop**

The outer loop can be configured for various control objectives depending on the operational mode of the battery:

- In voltage control mode, it regulates the DC bus voltage V_{dc}, supporting voltage stability during load variations or renewable generation fluctuations.
- In power control mode**,** it regulates the power exchanged with the DC bus (P_b or P_{bddc}), depending on the energy management strategy of the microgrid.

The outer loop operates with slower dynamics, and its output is the reference current i_{bref} for the inner loop. We use an regulator PI as follows :

According to the figure (III.19) we can get :

$$P_{in\ bddc} = P_{out\ bddc} \quad \text{(III.124)}$$

$$i_b V_b = V_{dc} i_{bddc} \quad \text{(III.125)}$$

Where

$$i_{bddc} = i_{Cdc} - i_L - \frac{V_{dc}}{R_s} - i_{ddbc} \quad \text{(III.126)}$$

Substituting (III.120) in (III.119) , we get :

$$i_b = \frac{V_{dc}}{V_b}\left(i_{Cdc} - i_L - \frac{V_{dc}}{R_s} - i_{ddbc}\right) \quad \text{(III.127)}$$

And we have :

$$i_{Cdc} = C_{dc}\frac{dV_{dc}}{dt} \quad \text{(III.128)}$$

Using Laplace transform, equation (III.122) becomes :

$$i_{Cdc} = C_{dc} s\, V_{dc} \quad \text{(III.129)}$$

The transfer function of the DC bus output capacitor system is given by :

$$\frac{V_{dc}}{i_{Cdc}} = \frac{1}{C_{dc}s} \quad \text{(III.130)}$$

From this transfer function it can be seen that the regulation of the DC bus output voltage can provids the DC bus output capacitor reference current (i^*_{Cdc}) , and using the DC bus output current as feedforword, we obtain the battery output current reference.

The schematic diagram of the PI-based outer DC bus output voltage control loop is given as in the figure (III.20).

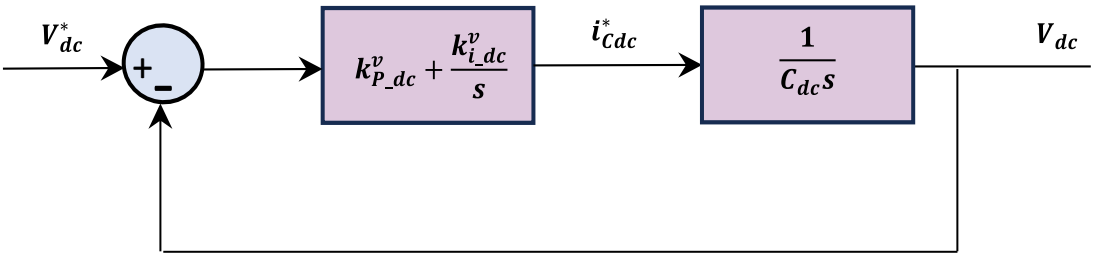

Fig.III.20: *The schematic diagram of the PI-based outer DC bus output voltage control loop.*

According to the schematic diagram of the PI-based outer DC bus output voltage control loop in figure (III.20) and equation (III.121), we obtain the battery output current reference as follows :

$$i^*_b = \frac{V_{dc}}{V_b}\left(i^*_{Cdc} - i_L - \frac{V_{dc}}{R_s} - i_{ddbc}\right) \quad \text{(III.131)}$$

The parametres of the PI regulator ($k^v_{P_dc}$and $k^v_{i\_dc}$) in this control loop are determied using the pols placement method as follows :

From the diagram in Figure (III.20), the closed loop transfer function is written as:

$$F_{dc_{close}}(s) = \frac{\frac{k_{P\_dc}^{v}}{C_{dc}}s + \frac{k_{i\_dc}^{v}}{C_{dc}}}{s^2 + \frac{k_{P\_dc}^{v}}{C_{dc}}s + \frac{k_{i\_dc}^{v}}{C_{dc}}} \quad \text{(III.132)}$$

To calculate the gains of the voltage regulator, the transfer function (III.126) has to exhibit the same dynamic behavior as a second-order system of the following transfer function:

$$H_v^{dc}(s) = \frac{(\omega_{nv}^{dc})^2}{s^2 + 2\xi_v^{dc}\omega_{nv}^{dc} + (\omega_{nv}^{dc})^2} \quad \text{(III.133)}$$

The proportional gain K_{p_v} and integral gain K_{i_v} are determined by identifying term by term the tow characteristic equations of (III.126) and (III.127) , which result in :

$$\begin{cases} K_{p_v} = 2\xi_v^{dc}\omega_{nv}^{dc}C_{dc} \\ K_{i_v} = (\omega_{nv}^{dc})^2 C_{dc} \end{cases} \quad \text{(III.134)}$$

where $\omega_{nv}^{dc}$is the natural frequency and$\xi_v^{dc}$is the damping coefficient.

- **Battery current control loop**

The inner loop is designed to regulate the inductor current (battery current) (i_b) of the bidirectional converter. This loop operates with high bandwidth to ensure fast dynamic response and accurate tracking of the current reference i_{bref}. By shaping the current flowing to or from the battery, it enhances system stability and improves the transient performance of power flow control. We use an regulator PI as follows :

The duty cycle of the converter's switches is calculated in this loop based on the current error, and it determines the power flow direction:

- S_{bddc}=1: discharging mode
- S_{bddc}=0: charging mode

From the circuit in the figure (III.19). we have:

$$U_{Lb} = U_{bddc} - r_b i_b - V_b \quad \text{(III.135)}$$

Where

$$U_{Lb} = L_b \frac{di_b}{dt} \quad \text{(III.136)}$$

Substituting (III.129) in (III.130) , we get :

$$L_b \frac{di_b}{dt} = U_{bddc} - r_b i_b - V_b \quad \text{(III.137)}$$

The Laplace transform; equation (III.130) becomes :

$$U_{Lb} = L_b s \, i_b \quad \text{(III.138)}$$

The transfer function of the battery-ouput inductor system is given by :

$$\frac{i_{Lb}}{U_{Lb}} = \frac{1}{L_b s} \quad \text{(III.139)}$$

From this transfer function it can be seen that the regulation of the battery output current can provids the battery inductor reference voltage(U_{Lb}^*), and using the battery input voltage as feedforword, we obtain the DC bus output voltage reference.

The schematic diagram of the PI-based output battery current control loop is given as in the figure (III.21).

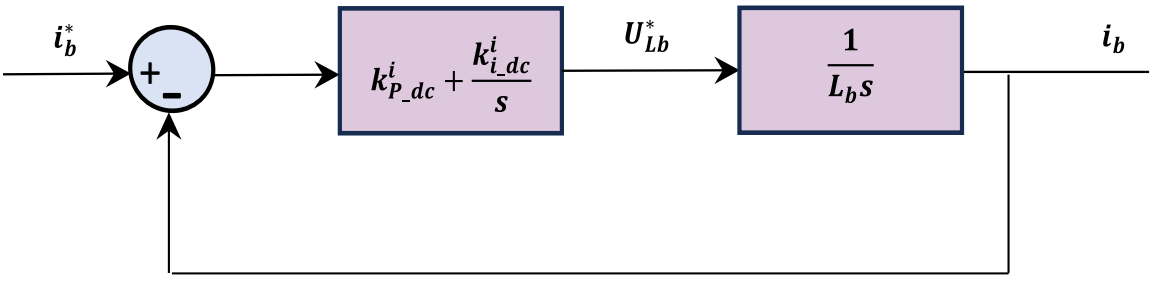

Fig.III.21: *The schematic diagram of the PI-based output battery current control loop.*

According to the schematic diagram of the PI-based input boost converter current loop in figure (III.21) and equation (III.129). we obtain the PV output voltage reference as follows:

$$U_{Lb}^* = U_{bddc}^* - r_b i_b - V_b \quad \text{(III.140)}$$

The parametres of the PI regulator ($k_{P_dc}^i$and $k_{i\_dc}^i$) in this control loop are determied using the pols placement method as follows :

From the diagram in Figure (III.21), the closed loop transfer function is written as:

$$F_{dc_{close}}(s) = \frac{\frac{k_{P\_dc}^i}{L_{dc}} s + \frac{k_{i\_dc}^i}{L_{dc}}}{s^2 + \frac{k_{P\_dc}^i}{L_{dc}} s + \frac{k_{i\_dc}^i}{L_{dc}}} \quad \text{(III.141)}$$

To calculate the gains of the current regulator, the transfer function (III.135) has to exhibit the same dynamic behavior as a second-order system of the following transfer function:

$$H_v^{dc}(s) = \frac{\left(\omega_{ni}^{dc}\right)^2}{s^2+2\xi_i^{dc}\omega_{ni}^{dc}+\left(\omega_{ni}^{dc}\right)^2} \quad \text{(III.142)}$$

The proportional gain K_{p_i} and integral gain K_{i_i} are determined by identifying term by term the tow characteristic equations of (III.135) and (III.136) , which result in :

$$\begin{cases} K_{p_i} = 2\xi_i^{dc}\omega_{ni}^{dc}L_{dc} \\ K_{i_i} = \left(\omega_{ni}^{dc}\right)^2 L_{dc} \end{cases} \quad \text{(III.143)}$$

where ω_{ni}^{dc} is the natural frequency and ξ_i^{dc} is the damping coefficient.

And from the same circuit we find as in figure (III.19):

If the switch $\begin{matrix} S=0 \\ S_1=1 \end{matrix}$; $U_{bddc} = V_{dc}$ else $\begin{matrix} S=1 \\ S_1=0 \end{matrix}$; $U_{bddc} = V_b - U_L$.

So :

$$U_{bddc} = (1-D)\,V_{dc} \quad \text{(III.144)}$$

And so :

$$U_L^* = V_b - U_{bddc} = V_b - (1-D)\,V_{dc} \quad \text{(III.145)}$$

So the duty cycle becomes :

$$D_{bddc} = \frac{U_L^* - V_b}{V_{dc}} + 1 \quad \text{(III.146)}$$

This hierarchical control approach guarantees the converter runs effectively and steadily under a range of load and environmental circumstances while enabling fine control over power flow and voltage levels.

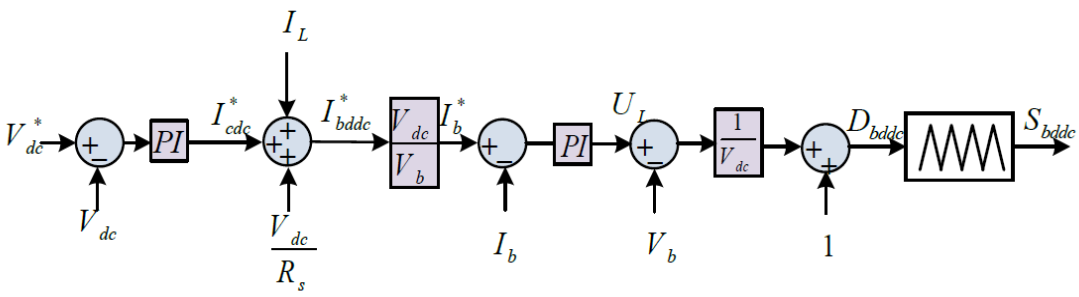

Fig.III.22: *Regulation of both the MICROGRID voltage and battery output current using PI controllers.*

The global schematic control of the PV/battrey based DC microgrid using traditional PI controllers is given as shown in Figure III.23

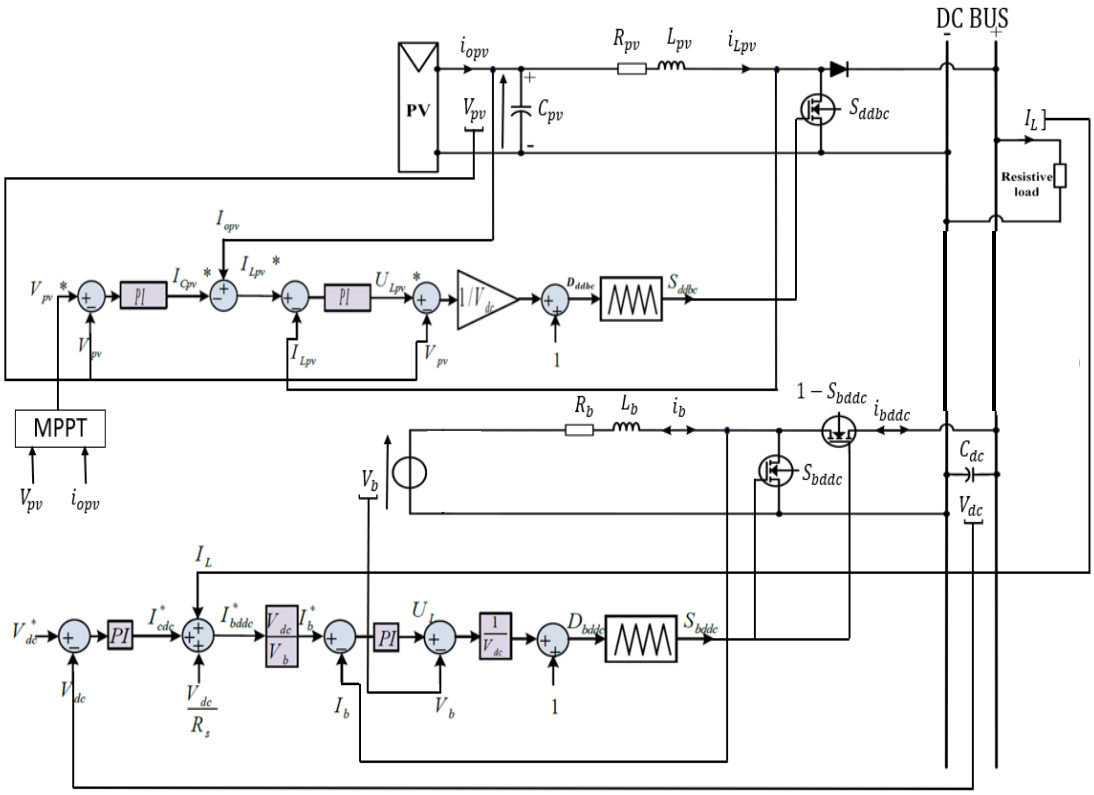

Fig.III.23: *glopal diagram of the control by PI regulators.*

III.4. Simulation results

In this simulation, the system (DC microgrid based on PV and battery) is controlled using PI regulators to maintain stable operation. The regulators adjust the control signals to keep currents, voltages, and power levels within desired ranges. We also monitor the State of Charge (SOC%) of the battery, which indicates the remaining available energy.

The results show that the PI controllers perform effectively, maintaining stable voltage and current levels with minimal fluctuations. The SOC changes predictably based on load demand, confirming proper system regulation. Overall, the simulation

demonstrates reliable control under the tested conditions. The result was as follows:

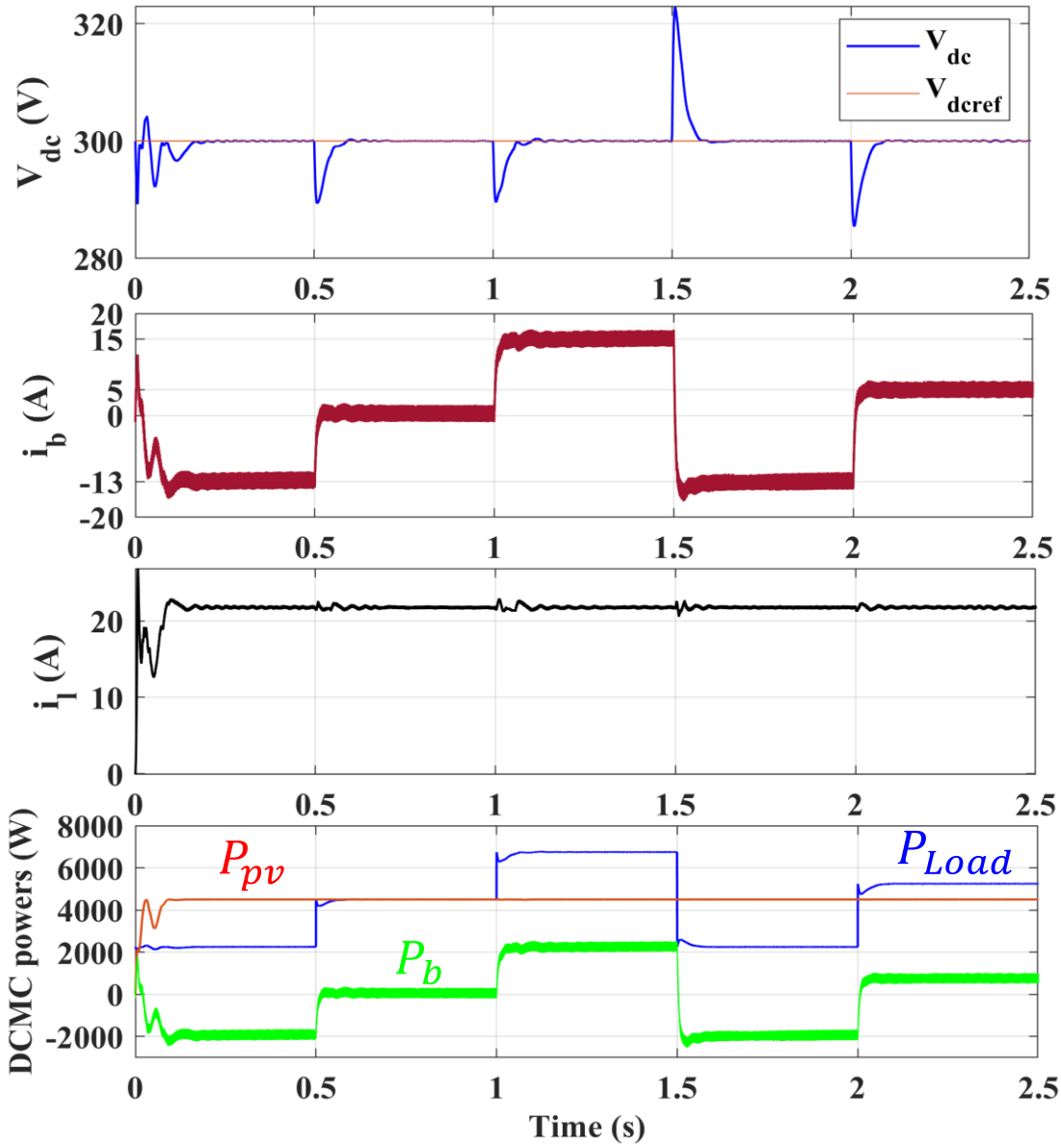

***Fig.III.24**:Simulation results of the systeme under load changes.*

Figure (III.24) illustrates the simulation results of the system under various load changes. Initially, the system operates with a resistive load of 40 Ω. Subsequently, additional resistive loads of 40 Ω, 40 Ω, and –20 Ω are introduced sequentially, followed by an additional load of 30 Ω. Despite these successive load variations, the system successfully maintains its performance, and the control strategy ensures that the DC voltage remains stable and the power balance is preserved. As a result, the system returns to its previous steady-state performance, demonstrating the robustness and effectiveness of the implemented control approach.

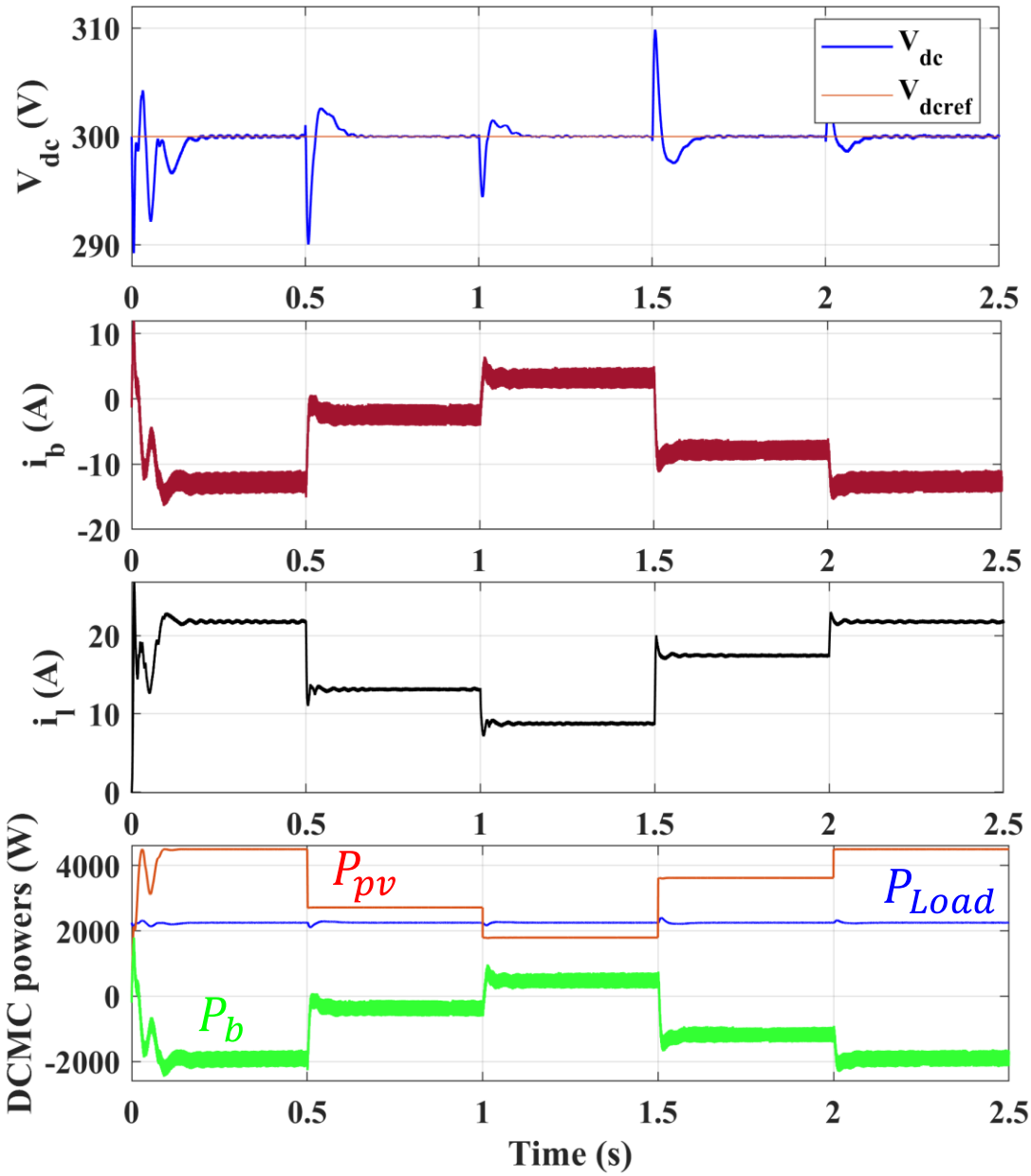

***Fig.III.25**:Simulation results of the systeme under solar iradiation changes.*

Figure (III.25) presents the simulation results of the system under varying solar irradiation levels. Initially, the solar irradiation is set to 1000 W/m². It is then decreased successively to 600 W/m², 400 W/m², followed by an increase to 800 W/m², and finally returns to 1000 W/m². Throughout these fluctuations, the control system effectively maintains the stability of the DC microgrid. The DC bus voltage remains regulated, and the power balance is preserved. After all changes in solar irradiation, the system successfully returns to its previous steady-state performance, demonstrating the robustness and adaptability of the implemented control strategy under varying environmental conditions.

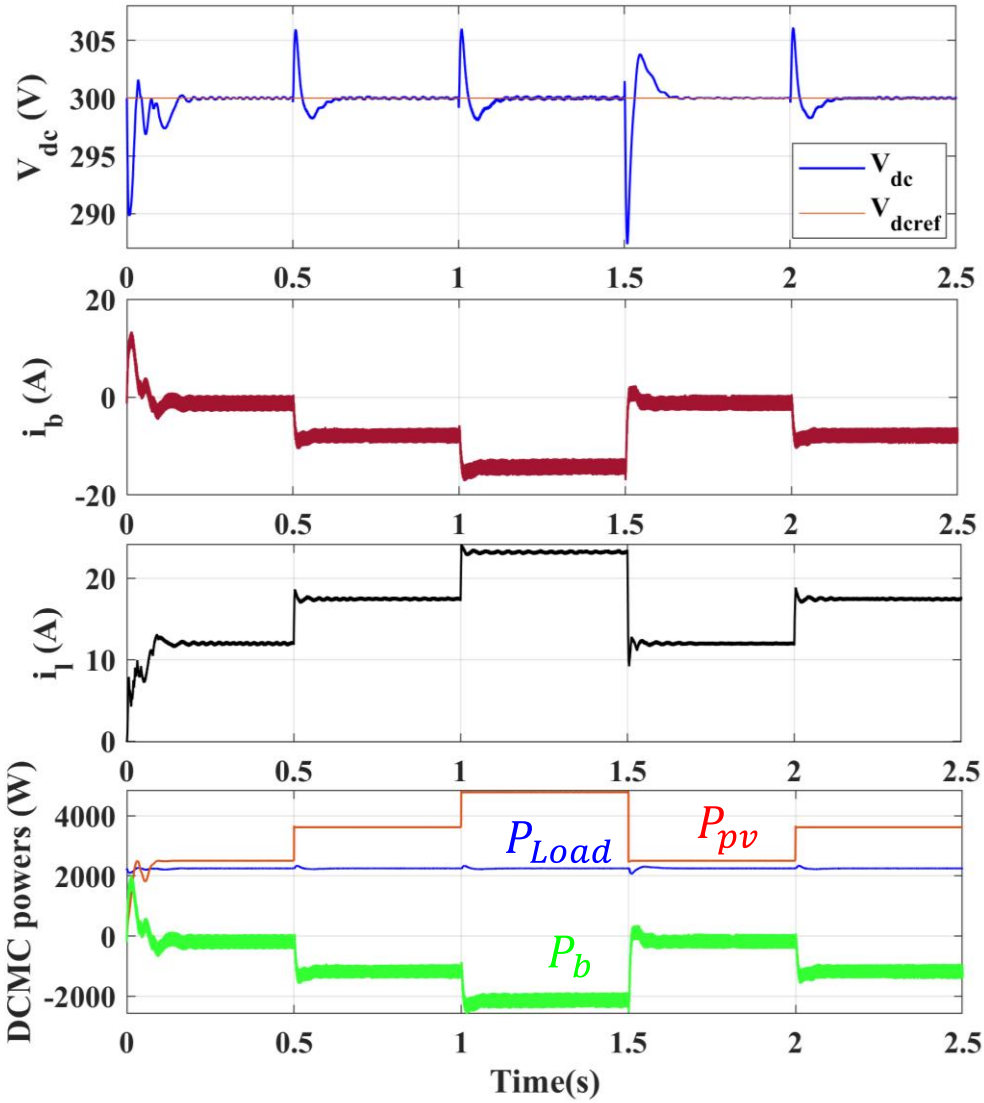

***Fig.III.26**:Simulation results of the systeme under PV cell temperature changes.*

Figure(III.26) illustrates the simulation results of the system under variations in the PV cell temperature. The initial temperature is set to 20°C, and it subsequently changes to 25°C, then 30°C, followed by a return to 20°C, and finally back to 25°C. These temperature variations directly affect the output characteristics of the photovoltaic source. Despite these changes, the control system effectively maintains the stability of the DC bus voltage and ensures power balance within the microgrid. After all temperature fluctuations, the system successfully returns to its previous steady-state behavior, confirming the robustness and efficiency of the applied control strategy in managing environmental disturbances.

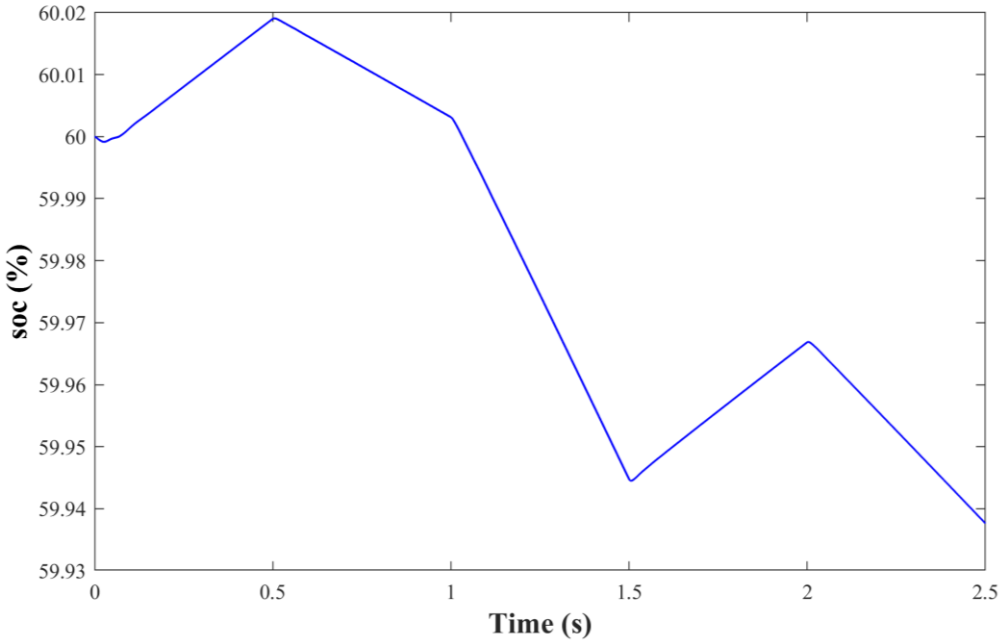

Fig.III.27: *State of charge (soc(%)) of the systeme under load changes.*

Figure(III.27) illustrates State of charge (soc(%)) of the systeme under load changes. The state of charge is following the power balance in our system Which occurs due to changes of charge $(P_{pv} = cte)$; when $P_{Load} < P_{pv}$ (the battery was in charge mod), and when $P_{Load} > P_{pv}$ (the battery was in discharge mod); becouse the battery compensates the lack of power in the PV (P_{pv}).

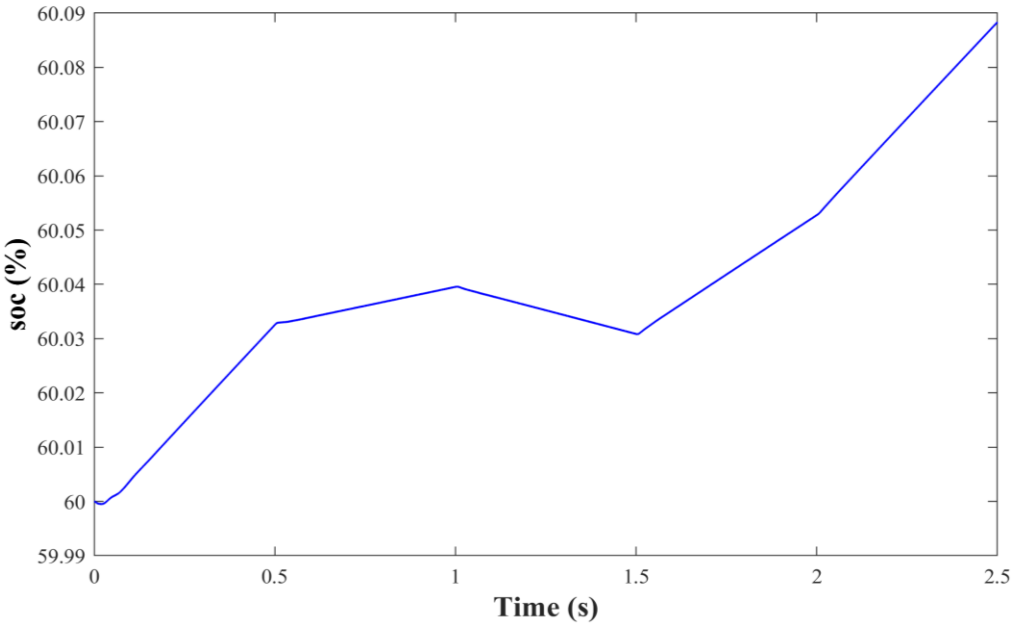

Fig.III.28: *State of charge (soc(%)) of the systeme under solar iradiation changes.*

Figure(III.28) illustrates State of charge (soc(%)) of the systeme under solar iradiation changes.in this case the state of charge is following the power balance in our system Which occurs due to changes of the solar iradiation $(P_{Load} = cte)$; when $P_{Load} < P_{pv}$ (the battery was in charge mod), and when $P_{Load} > P_{pv}$ (the battery was in discharge mod); becouse the battery compensates the lack of power Which creates when $P_{Load} >< P_{pv}$.

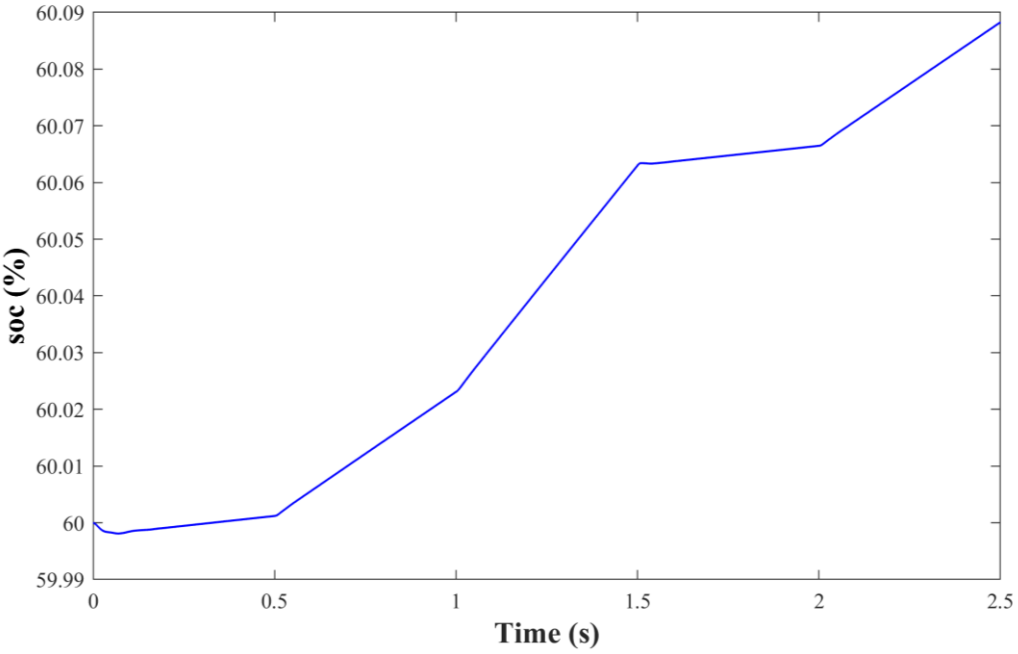

Fig.III.29: *State of charge (soc(%)) of the systeme under PV cell temperature changes.*

Figure(III.29) illustrates State of charge (soc(%)) of the systeme under PV cell temperature changes.in this case the state of charge is following the power balance in our system Which occurs due to changes of the PV cell temperature $(P_{Load} = cte)$; when $P_{Load} < P_{pv}$ (the battery was in charge mod), and when $P_{Load} > P_{pv}$ (the battery was in discharge mod); becouse the battery compensates the lack of power Which creates when $P_{Load} >< P_{pv}$.

III.5.Conclusion

Proportional-Integral (PI) controllers are employed to regulate a DC microgrid system composed of photovoltaic (PV) panels and battery energy storage. The control strategy is designed to ensure stable operation of the microgrid by maintaining the DC bus

voltage within acceptable limits and achieving real-time power balance between generation, storage, and load demands.

The simulation results clearly demonstrate the effectiveness of the implemented PI control approach. The system successfully maintains voltage stability across the DC bus and ensures dynamic power balance despite variations in solar irradiance and load conditions. Moreover, the control strategy significantly improves battery current quality by reducing ripple and suppressing undesirable fluctuations. This not only enhances energy efficiency but also contributes to extending the operational life of the battery system.

While PI controllers offer the advantages of simplicity and ease of implementation, they may face limitations in handling fast transients, nonlinearities, and uncertainties that are inherent in renewable-based DC microgrids. Therefore, in next chaptre, we aim to explore advanced control methodologies such as Super-Twisting Controllers, which are part of the higher-order Sliding Mode Control (SMC) family. These controllers are known for their robustness against disturbances and model uncertainties, and their ability to provide finite-time convergence without chattering.

The application of such advanced control techniques is expected to further enhance the performance of the DC microgrid, particularly in terms of voltage regulation, power quality, and system robustness under varying operational scenarios. Future studies will focus on validating these methods through comprehensive simulations and, potentially, experimental implementation .

Chapter IV

Control by super twisting

IV.1.Introduction

In order to ensure zero static error and a fast reaction, nonlinear control techniques are typically used to tackle some of the traditional control problems, such as parametric variations. This results in a stable and reliable control system. Sliding mode control (SMC) is renowned for its robustness and simplicity among these nonlinear control strategies.

V. Utkin created SMC in the early 1950s, and it has since been acknowledged as a useful tool for designing durable controllers in intricate high-order nonlinear dynamic plants that operate in a variety of unpredictable circumstances. SMC, which is based on the variable structure system control theory, offers ways to ensure robustness under parameter uncertainties that arise when PID controllers are utilized, as well as ways to overcome issues with instability or poor performance [66][68] [69]. The main benefit of SMC is its low sensitivity to disturbances and changes in parameters, which eases the need for precise system modeling [69][70].

The goal of this chapter's first section is not to go into great detail on the sliding mode control approach, but rather to provide a quick overview of it and then use it to control the PV and battery based DC microgrid system. The goal is to use the advantages of the super twisting algorithm technique to improve the control of all controlled varaiables within the overral control circout of the PV and battery based DC microgrid system, including the PV output voltage, the input boost converter current, the DC voltage, and the bettrey current will receive particular attention in chapter.

IV.2.First Order Sliding Mode Control

One specific method of working with systems that have changeable structures is the sliding mode control technique. According to a well-defined switching logic, a system with a changeable structure is one that can alter its structure by alternating between two states, as shown in figure (IV.1).

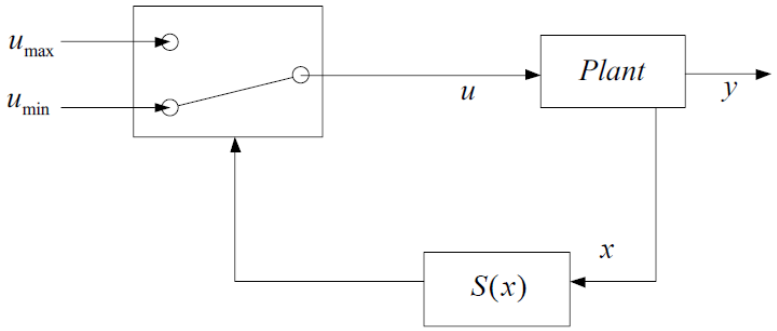

Fig.IV.1: *Variable structure regulation system with a change of structure by switching.*

The switching between two values is defined by the following law:

$$u = \begin{cases} u_{min} & for\ S(x) > 0 \\ u_{max} & for\ S(x) < 0 \end{cases} \quad \text{(IV.1)}$$

A good characterization of the switching logic and a reasonable selection of each structure's characteristics are essential for systems with variable structures. The system is in sliding mode when switching occurs at a relatively high frequency under specific circumstances. S(x) = 0 defines the system's dynamic behavior; S(x) is the sliding surface. The goal is to move the system's state trajectory in the direction of this surface and keep the sliding regime going until the system reaches equilibrium [68][69] [71].Robustness against parameter or disturbance changes is a major benefit of variable-structure control in sliding mode [71]. Other benefits of sliding mode control are its simplicity and ease of implementation. Because of these benefits, using this control is highly intriguing and ideal for grid-connected voltage source converters. Sliding mode control's "chattering" oscillation phenomenon, however, has a significant disadvantage in that it can excite high-frequency switching dynamics, which makes it undesirable as it frequently results in control inaccuracy and significant heat loss in electric circuitry [72][70].

Choosing the manifold in the state space that permits the trajectory of the system's state variables to converge towards the desired point of equilibrium is the first step in designing the control law in sliding mode. Next, the condition of the sliding mode's existence is established, which is connected to the convergence of the state

trajectory, and the control laws that have the responsibility of preserving the sliding conditions (attractiveness) are determined. In other words, the process of conceptualizing the law of control by sliding mode is completed in three steps [70][71]:

Step 1: Choice of sliding surface.

Step 2: Development of the convergence condition.

Step 3: Determination of the control law.

IV.2.1.Choice of Sliding Surface

For a system defined by equation (IV.2), the vector of the surface $S(x)$ has the same dimension as the control vector u .

$$\frac{dx}{dt} = f(x) + B(x)u \tag{IV.2}$$

The sliding surface is a scalar function such that the variable to be adjusted slides on this surface and tends towards the origin of the phase plane [68] [73][71]. A general form proposed by *J.J. Slotine* that ensure the convergence of the variable to settle towards its reference is given by [74]:

$$S(x) = \left(\frac{d}{dt} + \lambda\right)^{r-1} e(x) \tag{IV.3}$$

$e(x)$:Represents the difference between the variable to be regulated and its reference.

λ : is a positive constant.

r : is the relative degree of variable; it represents the number of times one takes to differentiate the output to bring up the control.

Maintaining the surface at zero is the control's goal. One way to think of the sliding surface is as a linear differential equation, with e(x) = 0. This comes down to a tracking the trajectory problem for an appropriate choice of controller gains, which is the same as an exact linearization of the difference while adhering to the convergence condition [74][73].

IV.2.2. Conditions of Existence and Convergence

The system's dynamics can converge towards the sliding surface when the condition of convergence or attractiveness is met; this is accomplished by creating a

scalar function of *Lyapunov* V (x) > 0 for the system's state variables. This function must be reduced by the control law. The answer is to create a control so that the square of the sliding surface corresponds to a *Lyapunov* function and to select a scalar function S(x) to ensure that the variable to be controlled is attracted to its reference value.

Lyapunov's function is defined as follows:

$$V(x) = \frac{1}{2}S^2(x) \quad \text{(IV.4)}$$

The derivative of this function is:

$$V(x) = S(x)\dot{S}(x) \quad \text{(IV.5)}$$

The function V(x) can be forced by making sure that its derivative is negative. According to equation (IV.4), the square of the separation between a certain point on the phase plane and the sliding surface, represented by S 2 (x), continuously diminishes as long as The Lyapunov function's derivative is always negative, which forces the system's path to move from both sides in the direction of the surface. An ideal sliding regime with an infinite switching frequency is assumed by this condition [75].

IV.2.3. Determination of the Sliding Mode Control Law

To achieve a sliding regime, a discontinuous control is necessary. A continuous component can be added to this discontinuous control if it is necessary [71]. The discontinuous control is used to confirm the attractiveness conditions when there is a disturbance. The sliding mode controller structure is composed of two sections: the stabilizing (u_{sw}) and the accurate linearization (u_{eq}) sections. It is determined by:

$$u = u_{eq} + u_{sw} \quad \text{(IV.6)}$$

The variable to be controlled on the sliding surface S(x) = 0 is maintained using the similar instruction put forward by Filipov and Utkin [71]. If this variable is not on the sliding surface, it is driven towards its reference using discontinuous control [73][76]. Verification of the convergence requirement is then established.

IV.2.3.1. Equivalent Control

Consider the previous system (IV.2), an equivalent control vector can be developed by setting the derivative as a function of time of the switching function equal to zero:

$$S(x,t) = \left(\frac{\partial S}{\partial x}\right)(f(x,\dot{t}) + B(x,t) + \frac{\partial S}{\partial t} = 0 \quad \text{(IV.7)}$$

Hence, we can find the equivalent control defined by:

$$u_{eq} = -\left[\left(\frac{\partial S}{\partial x}\right)^t B(x,t)\right]^{-1}\left\{\left(\frac{\partial S}{\partial x}\right)^t f(x,t) + \frac{\partial S}{\partial t}\right\}$$

(IV.8)

With the condition of existence:

$$\left[\left(\frac{\partial S}{\partial x}\right)^t B(x,t)\right] \neq 0 \qquad \text{(IV.8)}$$

IV.2.3.2. Discontinuous Control

A control that can bring these trajectories closer to its references is required when the state trajectories are not on the sliding surface S(x) = 0 because of disruptions or modifications in the system parameters. This condition can be met by a discontinuous function (two-level switch), which is defined by:

$$u_{sw} = -ksgn(S(x)) \qquad with\ k > 0$$

(IV.10)

With :

$$sgn\big(S(x)\big) = \begin{cases} 1 & S(x) > 0 \\ -1 & S(x) < 0 \\ 0 & S(x) = 0 \end{cases} \qquad \text{(IV.9)}$$

IV.2.4. Integral Sliding Mode Control

In this approach, the sliding surface can be improved by inserting an integral action in its expression, this surface is then defined by [71]:

$$S(t) = \left(\lambda + \frac{d}{dt}\right)^{r-1} e(x) + k_i \int e(t)dt$$

(IV.12)

where k_i is a positive integral gain.

This method has the benefit of using a plane that passes through the origin as the sliding surface. When the system is second order, r = 2, the solution is found on a plane, however in the classic sliding mode, the solution is found on a line [71][76][77].

IV.3.Second-Order Sliding Mode Control

A promising method for handling the chattering issue while retaining the primary benefits of the traditional SMC in terms of resilience, order reduction, simplicity, and ease of implementation is higher-order sliding modes (HOSM). [78][79]. Furthermore, in the presence of switching delays and measurement noise, it is claimed that the practical application of HOSM yields a greater accuracy than the standard SMC [80]. A continuation of the conventional sliding mode theory is HOSM.

In this context, first-order sliding mode control (1-SMC) is typically used to refer to the classical SMC that was previously presented. The 1-SMC is restricted to situations where the sliding variable and the relative degree inside the system must be one, which may restrict the sliding variable's selection [81]. This is another reason for the development of this approach. Prior to applying the actual control signal, integrators are added to the input channel with the primary goal of increasing the order of the controlled system. As a result, unlike in 1-SMC, the discontinuous control component affects the sliding variable's higher-order time derivative rather than its first-time derivative. To put it another way, this new approach can much lessen the chattering effect because the higher derivative of the sliding variable actually contains the discontinuous control action [81], [73], and [82]. HOSM can be achieved using a variety of algorithms. To zero the outputs with relative degree two or to prevent chattering when zeroing the outputs with relative degree one, the second order sliding mode controllers (2-SMC) are specifically used. The sub-optimal controller, terminal sliding mode controllers, twisting controllers, and super-twisting controllers are examples of second-order algorithms. Specifically, the method for twisting forces the S(x) knowledge is necessary to slide a variable of relative degree two into the 2-sliding set. Although the sliding variable has relative degree one, the super-twisting algorithm does not require that. Because it gets rid of chattering, the super-twisting algorithm is currently preferred over the traditional siding method. This section presents a brief review on the super-twisting algorithm, which has been successfully implemented to solve the chattering problems.

IV.3.1. Basic Concepts Second-Order Sliding Mode Control: Super Twisting Algorithm

Considering an uncertain nonlinear system whose dynamics is described by:

$$\begin{cases} x^n = f(x) + g(x)u \\ S = S(x) \end{cases} \quad \text{(IV.10)}$$

where S is the sliding variable, f (x) and g(x) are some smooth and uncertain vector functions, t is the time, $u \in R$ is the control input, and $x \in R^n$ is the state vector. In order to guarantee convergence in an unlimited amount of time, the sliding surface is built with a relative degree r with regard to the control variable u, and it is defined to satisfy the necessary control parameters. Driving the intended sliding variable S to zero in a finite amount of time is the control goal in 1-SMC. In contrast, 2-SMC requires that the sliding variable S and its derivative $\dot{S}$ be driven to zero in a finite amount of

time. The second derivative of the sliding variable $\ddot{S}$ is subjected to a discontinuous control action in order to accomplish this [73]. This technique, despite being a 2-SMC, was first created for systems with relative degree one in order to circumvent the chattering issue associated with the use of 1-SMC [78]. That is, only when the system's relative degree is one can this technique drive the sliding variable and its derivative to zero in finite time. The sliding mode control's control signal is typically divided into two sections: one that relates to the equivalent control, which handles the system's and the sliding surface's dynamics, and another that relates to the switching control, which is in charge of preserving the system's dynamics on the sliding surface.

Defining the sliding surface as:

$$S(x) = e \tag{IV.11}$$

where e is the tracking error defined as follows:

$$e = x - x_{ref} \tag{IV.12}$$

where x_{ref} is the desired trajectory, and x is the actual trajectory.

The sliding mode control is given:

$$u = u_{eq} + u_{sw} \tag{IV.13}$$

where u_{eq} is the equivalent control proposed by *Filipov* without regarding the system uncertainty and external disturbance. It serves to keep the variable to control on the sliding surfaces. The equivalent control is derived by considering that the derivative of the surface is null $S(x)= 0$. u_{sw} is the discrete control, which ensures convergence such that $\dot{S}S >0$.

In Super-Twisting sliding mode control, switching control is usually adopted as:

$$\begin{aligned} u_{sw} &= -\lambda |S|^{\frac{1}{2}} sign(S) + u_1 \\ \dot{u} &= -\alpha sign(S) \end{aligned} \tag{IV.14}$$

Therefore, the time derivative of the sliding surface $S(x)$ is:

$$\dot{S}(x) = \dot{e} = \dot{x} - \dot{x}_{ref} \tag{IV.15}$$

Equation (IV.13) can be rewritten:

$$u_{eq} = \frac{-f(x)+\dot{x}_{ref}}{g(x)} \tag{IV.16}$$

The switching control law is designed based on the Super-Twisting algorithm, the algorithm is as follow:

$$u_{sw} = -\lambda |S|^{\frac{1}{2}} sign(S) - \int \alpha sign(S)\, dt \tag{IV.17}$$

where α and λ are positive constants.

The final control law can be obtained as follows:

$$u = \frac{-f(x)+\dot{x}_{ref}}{g(x)} = -\lambda|S|^{\frac{1}{2}}sign(S) - \int \alpha sign(S)\, dt$$

(IV.21)

IV.3.2. Stability Analysis

In order to achieve an explicit relation for the controller design parameters, the work published in [83][84] proposes quadratic like Lyapunov functions for the super-twisting controller. We shall return this analysis in the lines that follow.

$$\dot{S} = \Psi(S) + u \qquad \text{(IV.18)}$$

WhereΨ (S) is an unknown bounded perturbation term and globally bounded by:

$|\Psi(S)| \leq \delta|S|^{\frac{1}{2}}$ for some constant $\delta > 0$. The super-twisting sliding mode controller for perturbation and chattering elimination is given by:

$$u_{sw} = -\lambda|S|^{\frac{1}{2}}sign(S) + u_1$$
$$\dot{u}_1 = -\alpha sign(S)$$

(IV.23)

System (IV.22)closed by control (IV.23)results in:

$$\dot{S} = -\lambda|S|^{\frac{1}{2}}sign(S) + u_1 + \Psi(S)$$
$$\dot{u}_1 = -\alpha sign(S)$$

(IV.24)

Proposing the following candidate *Lyapunov* function:

$$V = 2\alpha|S| + \frac{1}{2}u_1^2 + \frac{1}{2}\left(\lambda|S|^{\frac{1}{2}}sign(S) - u_1\right) = \xi^T P\xi$$

(IV.25)

Where

$$\xi^T = \left(|S|^{\frac{1}{2}}sign(S), u_1\right) \qquad \text{(IV.19)}$$

$$P = \frac{1}{2}\begin{pmatrix} 4\alpha + \lambda^2 & -\lambda \\ -\lambda & 2 \end{pmatrix} \qquad \text{(IV.20)}$$

The time derivative of (IV.25)is:

$$\frac{dV}{dt} = \frac{d}{dt}(\xi^T P\xi) = \dot{\xi}^T P\xi + \xi^T P\dot{\xi} \qquad \text{(IV.21)}$$

Equation (IV.28) can be rewritten in the following form:

$$\dot{V} = -\frac{1}{\left|s^{1/2}\right|}\xi^T Q\xi + \frac{\Psi(S)}{\left|s^{1/2}\right|}q^T\xi$$

(IV.29)

Where :

$$Q = \frac{\lambda}{2}\begin{pmatrix} 2\alpha + \lambda^2 & -\lambda \\ -\lambda & 1 \end{pmatrix} \quad \text{(IV.22)}$$

$$q^T = \begin{pmatrix} 2\alpha + \frac{1}{2}\lambda^2 & -\frac{1}{2}\lambda \end{pmatrix}$$

(IV.31)

Applying the bounds for the perturbations as given in [83][84], the expression for the derivative of the *Lyapunov* function is reduced to

$$\dot{V} = -\frac{1}{2\left|s^{1/2}\right|}\xi^T\hat{Q}\xi$$

(IV.32)

Where

$$\hat{Q} = \begin{pmatrix} 2\alpha + \lambda^2 - \left(\frac{4\alpha}{\lambda} + \lambda\right)\delta & -\lambda + 2\delta \\ -\lambda + 2\delta & 1 \end{pmatrix}$$

(IV.33)

$\dot{V}$ is negative if $\hat{Q} \geq 0$, which is valid if the controller gains α and λ satisfy the following conditions:

$$\lambda > 2\delta\,,\ and\ \alpha > \lambda\frac{5\lambda\delta + 4\delta^2}{2(\lambda - 2\delta)} \quad \text{(IV.23)}$$

IV.3.3. Super twisting control of the DC microgrid

In this section, to improve the performance and dynamic responses of the four control loops within the overal control circuit of the DC microgrid, as well as the robustness to parametters variations, the super twisting technique is used instead of the PI controllers.

III.3.3.1.Super twisting control of the boost converter

In the control of boost converter for PV applications, a double-loop control strategy is commonly employed to enhance system performance, stability, and dynamic response. This structure consists of two main loops: a current control loop for regulating the input current of the boost converter (inductor current) and a voltage control loop for regulating the voltage of the PV. After discussing the theoretical basis of the super twisting control technique, the control law will be driven for the boost converter for PV system. The control of this system must enable PV voltage regulation as well boost converter input current control.

➢ **Super twisting control of PV voltage**

For the purpose of PV voltage controller design, we define the following surface.

$$S_1 = V_{pv} - V_{pv}^* \quad \text{(IV.24)}$$

The equivalent control design starts first by defining the sliding surfaces derivatives as follows:

$$S_1 = \dot{S}_1 = 0 \quad \text{(IV.25)}$$

Using the dynamic model of the PV voltage in (III.95), the derivatives of the two sliding surfaces can be written in the following form:

$$\dot{S}_1 = f_1(x) + g_1 u_{eq1} - \dot{V}_{pv}^* = 0 \quad \text{(IV.26)}$$

where

$f_1(x) = \frac{-i_{Lpv}}{C_{pv}}$ and $g_1 = \frac{1}{C_{pv}}$

Setting $\dot{S}_1 = 0$, then the equivalent control law can be obtained as:

$$u_{eq1} = \frac{-f_1(x) + \dot{V}_{pv}^*}{g_1} \quad \text{(IV.27)}$$

The switching control law is designed based on the Super-Twisting technique as follows:

$$u_{s1} = -\lambda_1 |S_1|^{\frac{1}{2}} sign(S_1) - \alpha_1 \int sign(S_1) dt \quad \text{(IV.28)}$$

Where λ_1 and α_1 are positive constants

The final super twisting control law of the PV voltage regulation that represent the boost converter input current reference is then given by:

$$u_1 = i_{Lpv}^* = u_{s1} + u_{eq1} \quad \text{(IV.29)}$$

$$i_{Lpv}^* = -\lambda_1 |S_1|^{\frac{1}{2}} sign(S_1) - \alpha_1 \int sign(S_1) dt + \frac{-f_1(x) + \dot{V}_{pv}^*}{g_1} \quad \text{(IV.30)}$$

➢ **Super twisting control of boost converter input current**

In this section, after providing the input current reference of the boost converter from the regulation of the PV voltage, a super twisting controller is used for regulating the input current of the boost converter to provide the duty cycle of the boost converter. So, for this purpose, we define the following surface.

$$S_2 = i_{Lpv} - i_{Lpv}^* \quad \text{(IV.31)}$$

In this, the equivalent control design is starts by defining the sliding surfaces derivatives as follows:

$$S_2 = \dot{S}_2 = 0 \quad \text{(IV.32)}$$

Using the dynamic model of the boost converter input current in (III.98), the derivatives of the two sliding surfaces can be written in the following form:

$$\dot{S}_2 = f_2(x) + g_2 u_{eq2} - \dot{i_{Lpv}^*} = 0 \quad \text{(IV.33)}$$

where

$$f_2(x) = \frac{1}{L_{pv}}\left(V_{pv} - V_{dc} - r_{pv} i_{Lpv}\right) \text{ and } g_2 = \frac{V_{dc}}{L_{pv}}$$

When setting $\dot{S}_2 = 0$, we obtained the equivalent control law of the regulation of boost converter input current u_{eq2} as follows:

$$u_{eq2} = \frac{-f_2(x) + \dot{i_{Lpv}^*}}{g_2} \quad \text{(IV.34)}$$

In this regulation, the switching control law u_{s2} is designed based on the Super-Twisting technique as follows:

$$u_{s2} = -\lambda_2 |S_2|^{\frac{1}{2}} sign(S_2) - \alpha_2 \int sign(S_2) dt \quad \text{(IV.35)}$$

Where λ_2 and α_2 are positive constants

The final super twisting control law of the boost converter input current regulation that represent the duty cycle of the boost converter is then given by:

$$u_2 = U_{ddbc}^* = u_{s2} + u_{eq2} \quad \text{(IV.36)}$$

$$U_{ddbc}^* = -\lambda_2 |S_2|^{\frac{1}{2}} sign(S_2) - \alpha_2 \int sign(S_2) dt + \frac{-f_2(x) + \dot{i_{Lpv}^*}}{g_2} \quad \text{(IV.37)}$$

III.3.3.2. Super twisting control of the bidirectional converter

In this section, we use the super twisting control technique for regulationg both the DC voltage and battery current, aiming to improve the stability and performance of the DC microgrid.

- **Super twisting control of DC voltage**

As described in third chapter, the regulating the DC voltage can provide the battery reference current. So, for the purpose of implemented this regulation using the super twisting technique, we define the following surface.

$$S_3 = V_{dc} - V_{dc}^* \tag{IV.38}$$

In this regulation part, the equivalent control design is first starts by defining the sliding surfaces derivative as follows:

$$S_3 = \dot{S}_3 = 0 \tag{IV.39}$$

Using the dynamic model of the DC voltage in (III.95), the derivatives of the two sliding surfaces can be written in the following form:

$$\dot{S}_3 = f_3(x) + g_3 u_{eq3} - \dot{V}_{dc}^* = 0 \tag{IV.40}$$

where

$$f_3(x) = \frac{1}{C_{dc}}\left(i_{ddbc} - \frac{V_{dc}}{R_{loss}} - I_L\right) \text{ and } g_3 = \frac{V_b}{C_{dc}V_{dc}}$$

Setting $\dot{S}_3 = 0$, then the equivalent control law of the DC voltage regulation can be obtained as:

$$u_{eq3} = \frac{-f_3(x)+\dot{V}_{dc}^*}{g_3} \tag{IV.41}$$

The switching control law is designed based on the Super-Twisting technique as follows:

$$u_{s3} = -\lambda_3 |S_3|^{\frac{1}{2}} sign(S_3) - \alpha_3 \int sign(S_3) dt \tag{IV.42}$$

where λ_3 and α_3 are the DC voltage super twisting gains, which are positive constants

The final super twisting control law of the DC voltage regulation that represent the battery current reference is then given by:

$$u_3 = i_b^* = u_{s3} + u_{eq3} \tag{IV.43}$$

$$i_b^* = -\lambda_3 |S_3|^{\frac{1}{2}} sign(S_3) - \alpha_3 \int sign(S_3) dt + \frac{-f_3(x)+\dot{V}_{dc}^*}{g_3} \tag{IV.44}$$

- **Super twisting control of boost converter input current**

In this section, after providing the battery current reference from the regulation of the DC voltage, a super twisting controller is used for regulating the battery current to

provide the duty cycle of the bidirectional converter. So, for this purpose, we define the following surface.

$$S_4 = i_b - i_b^* \tag{IV.45}$$

In this, the equivalent control design is starts by defining the sliding surfaces derivatives as follows:

$$S_4 = \dot{S}_4 = 0 \tag{IV.46}$$

Using the dynamic model of the battery current in (III.123), the derivatives of the two sliding surfaces can be written in the following form:

$$\dot{S}_4 = f_4(x) + g_4 u_{eq4} - \dot{i}_b^* = 0 \tag{IV.47}$$

where

$$f_4(x) = \frac{1}{L_b}(V_b - r_b i_b) \text{ and } g_4 = \frac{V_{dc}}{L_b}$$

When setting $\dot{S}_4 = 0$, we obtained the equivalent control law of the regulation of battery current u_{eq4} as follows:

$$u_{eq4} = \frac{-f_4(x) + \dot{i}_b^*}{g_4} \tag{IV.48}$$

Similarly, the switching control law u_{s4} is designed based on the Super-Twisting technique as follows:

$$u_{s4} = -\lambda_4 |S_4|^{\frac{1}{2}} sign(S_2) - \alpha_4 \int sign(S_4) dt \tag{IV.49}$$

Where λ_4 and α_4 are positive constants, representing the gains of super twisting controller used for the regulation of the battery current.

The final super twisting control law of the battery current regulation that represent the duty cycle of the bidirectional converter is then given by:

$$u_4 = U_{bddc}^* = u_{s4} + u_{eq4} \tag{IV.50}$$

$$U_{bddc}^* = -\lambda_2 |S_2|^{\frac{1}{2}} sign(S_2) - \alpha_2 \int sign(S_2) dt + \frac{-f_2(x) + \dot{i}_{Lpv}^*}{g_2} \tag{IV.51}$$

The ovaral control schematic of the DC microgrid using the super twisting technique is shown in Figure. IV. 2.

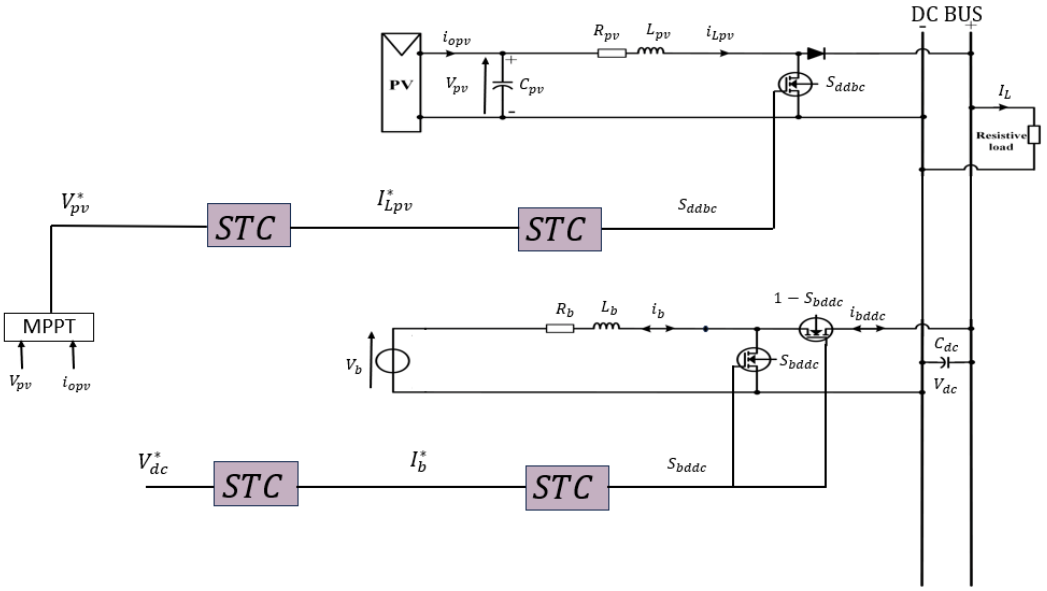

Fig.IV.2: *glopal diagram of the control by super twisting controllers.*

IV.4. Simulation results

In this simulation, the system (DC microgrid based on PV and battery)is controlled using super twisting method to maintain stable operation. The method adjusts the control signals to keep currents, voltages, and power levels within desired ranges. We also monitor the State of Charge (SOC%) of the energy storage system, which indicates the remaining available energy. After we used the regulators PI ,now we use super twisting method To improve results, so the results was as follows :

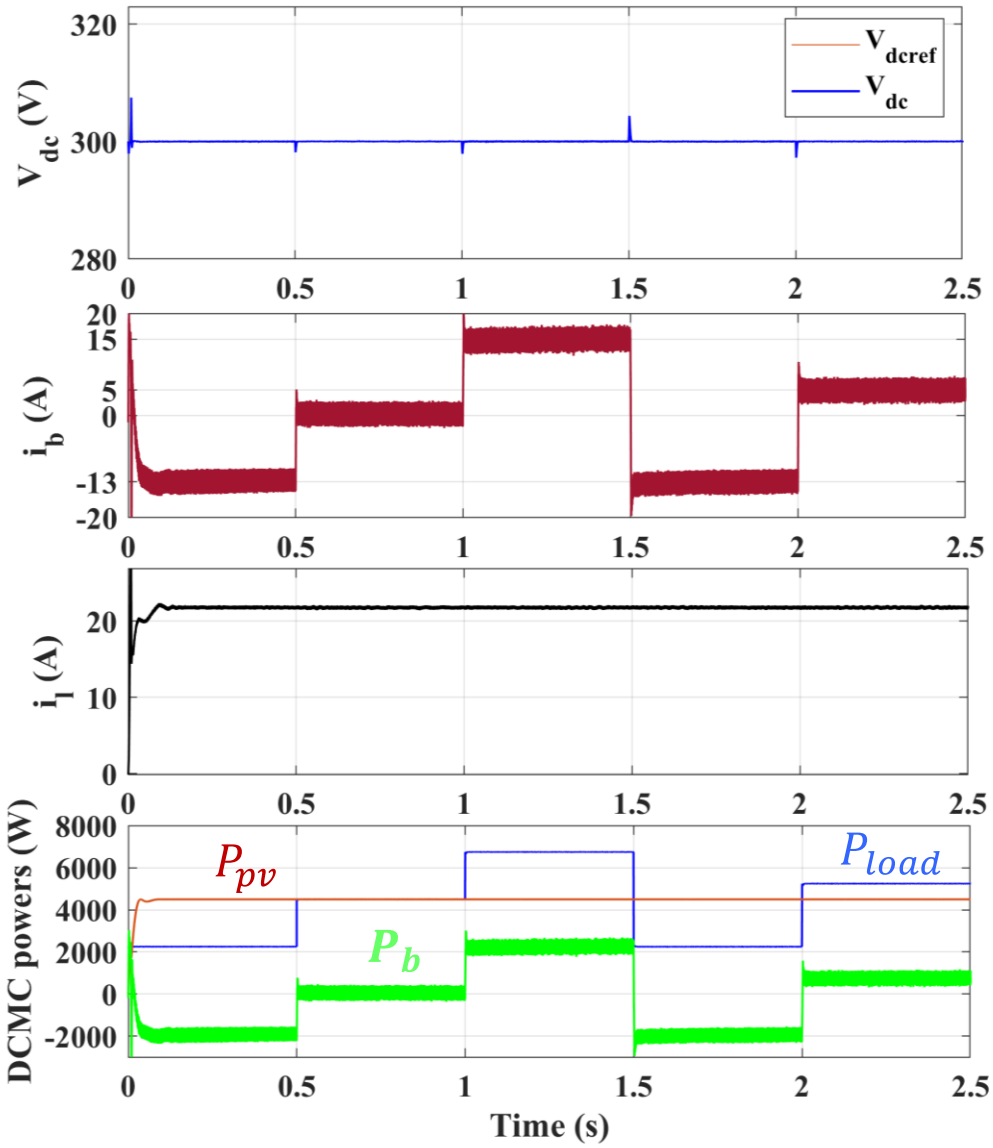

Fig.IV.3: *Simulation results of the systeme under load changes control by super twisting.*

Figure (IV.3) illustrates the simulation results of the system under various load changes control by super twisting. Initially, the system operates with a resistive load of 40 Ω. Subsequently, additional resistive loads of 40 Ω, 40 Ω, and –20 Ω are introduced sequentially, followed by an additional load of 30 Ω. Despite these successive load variations, the system successfully maintains its performance, and the control strategy ensures that the DC voltage remains stable and the power balance is preserved. As a result, the system returns to its previous steady-state performance, demonstrating the robustness and effectiveness of the implemented control approach.

In this case, it is evident that the control strategy based on the super-twisting algorithm yields significantly better performance compared to the conventional PI regulators. One of the most notable improvements is the elimination of current ripple, which contributes

to enhanced system efficiency. Additionally, the voltage response is much more stable, indicating a more robust and reliable control behavior.

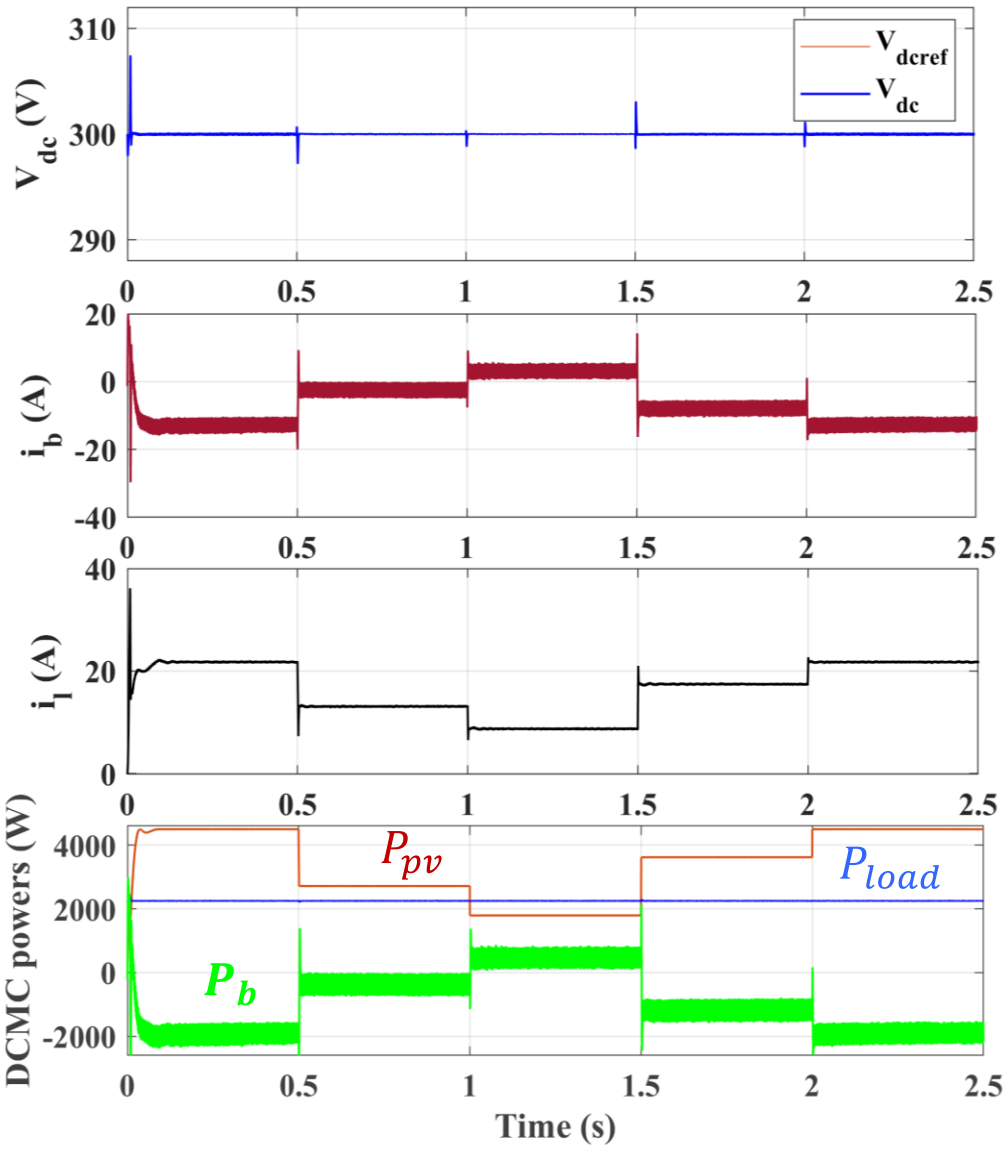

Fig.IV.4: *Simulation results of the systeme under solar iradiation changes control by super twisting.*

Figure (IV.4) presents the simulation results of the system under varying solar irradiation levels control by super twisting. Initially, the solar irradiation is set to 1000 W/m². It is then decreased successively to 600 W/m², 400 W/m², followed by an increase to 800 W/m², and finally returns to 1000 W/m². Throughout these fluctuations, the control system effectively maintains the stability of the DC microgrid. The DC bus voltage remains regulated, and the power balance is preserved. After all changes in solar irradiation, the system successfully returns to its previous steady-state performance, demonstrating the robustness and adaptability of the implemented control strategy under varying environmental conditions.

The results clearly demonstrate that using the super-twisting control method provides superior outcomes when compared to the traditional PI controllers. Unlike the PI-based approach, which often introduces noticeable ripples in the current, the super-twisting technique maintains a smooth and steady current profile. Furthermore, the voltage remains consistently stable throughout the operation, reflecting improved dynamic response and system reliability.

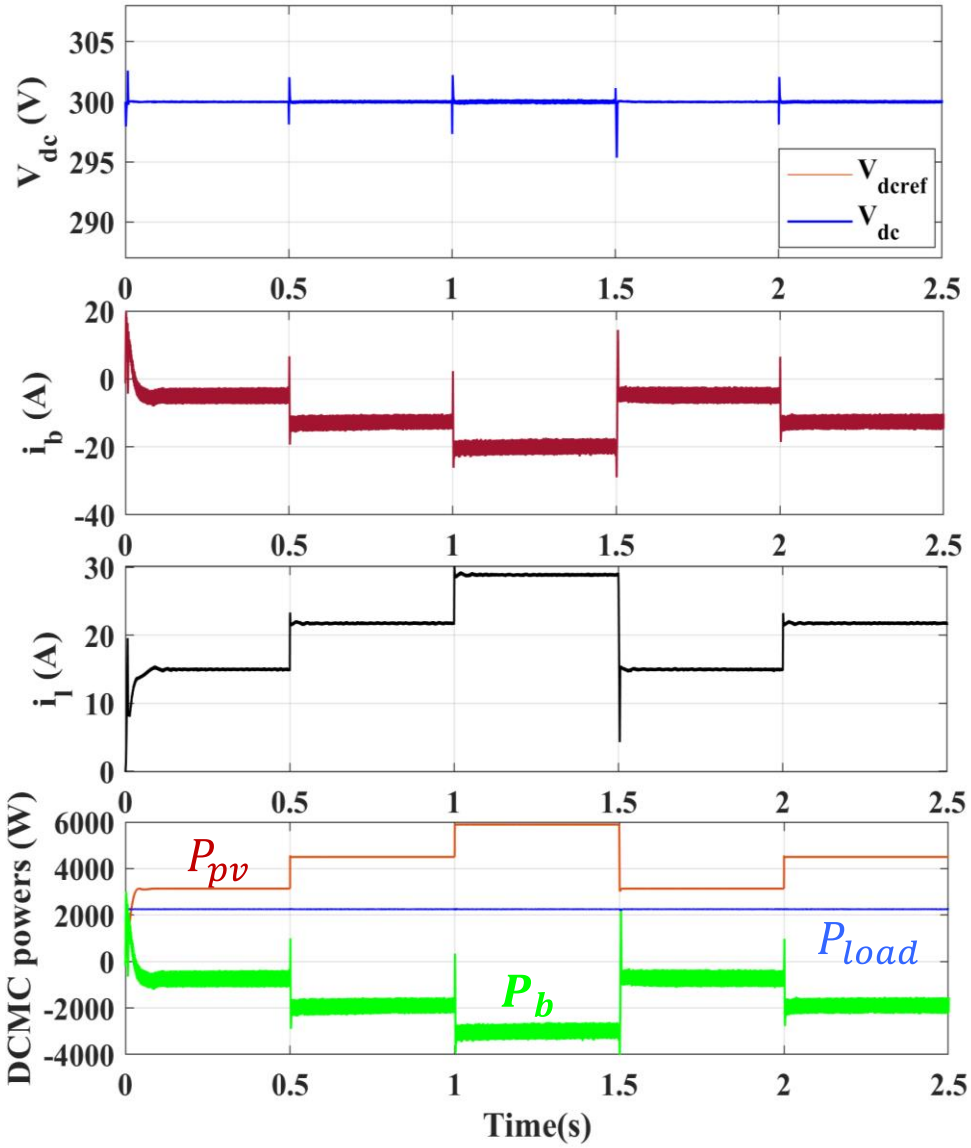

Fig.IV.5: *Simulation results of the systeme under PV cell temperature changes control by super twisting.*

Figure(IV.5) illustrates the simulation results of the system under variations in the PV cell temperature control by super twisting. The initial temperature is set to 20°C, and it subsequently changes to 25°C, then 30°C, followed by a return to 20°C, and finally

back to 25°C. These temperature variations directly affect the output characteristics of the photovoltaic source. Despite these changes, the control system effectively maintains the stability of the DC bus voltage and ensures power balance within the microgrid. After all temperature fluctuations, the system successfully returns to its previous steady-state behavior, confirming the robustness and efficiency of the applied control strategy in managing environmental disturbances.

From the observations in this scenario, it's apparent that the super-twisting control method outperforms the PI regulator approach in several aspects. Most importantly, the current waveform shows no signs of ripple, which is a common issue in PI-based control. Moreover, the voltage remains steady without fluctuations, highlighting the advantages of using a higher-order sliding mode technique in achieving better control quality.

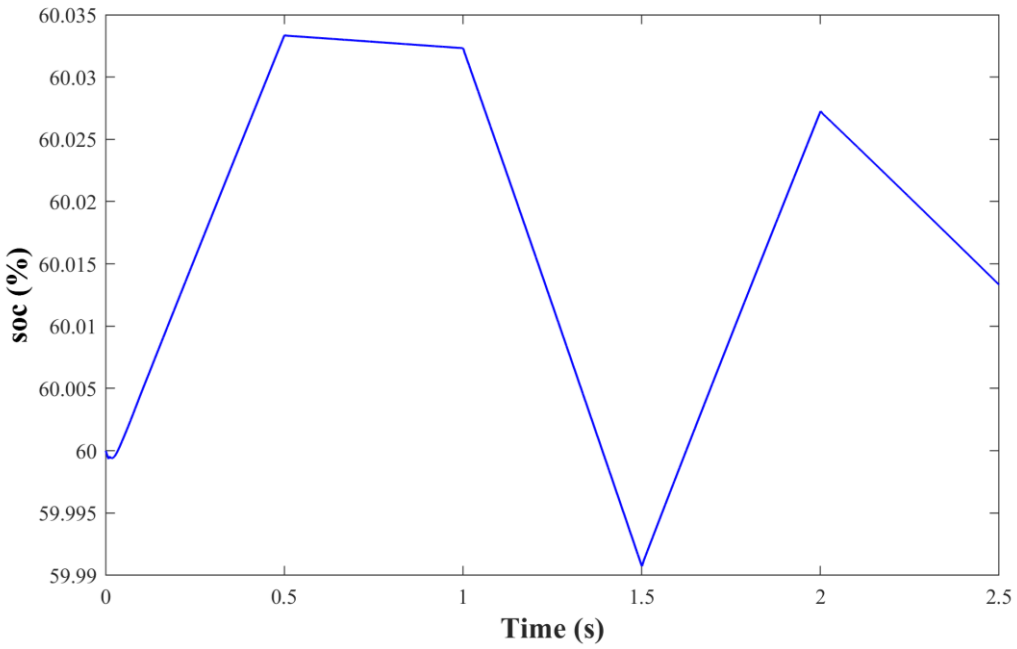

Fig.IV.6: *State of charge (soc(%)) of the systeme under load changes changes control by super twisting.*

Figure(IV.6) illustrates State of charge (soc(%)) of the systeme under load changes control by super twisting. The state of charge is following the power balance in our system Which occurs due to changes of charge $(P_{pv} = cte)$; when $P_{Load} < P_{pv}$ (the battery was in charge mod), and when $P_{Load} > P_{pv}$ (the battery was in discharge mod); becouse the battery compensates the lack of power in the PV (P_{pv}).

In this case we can see that the results of cammand by super twisting is better than the commad by regulators PI .

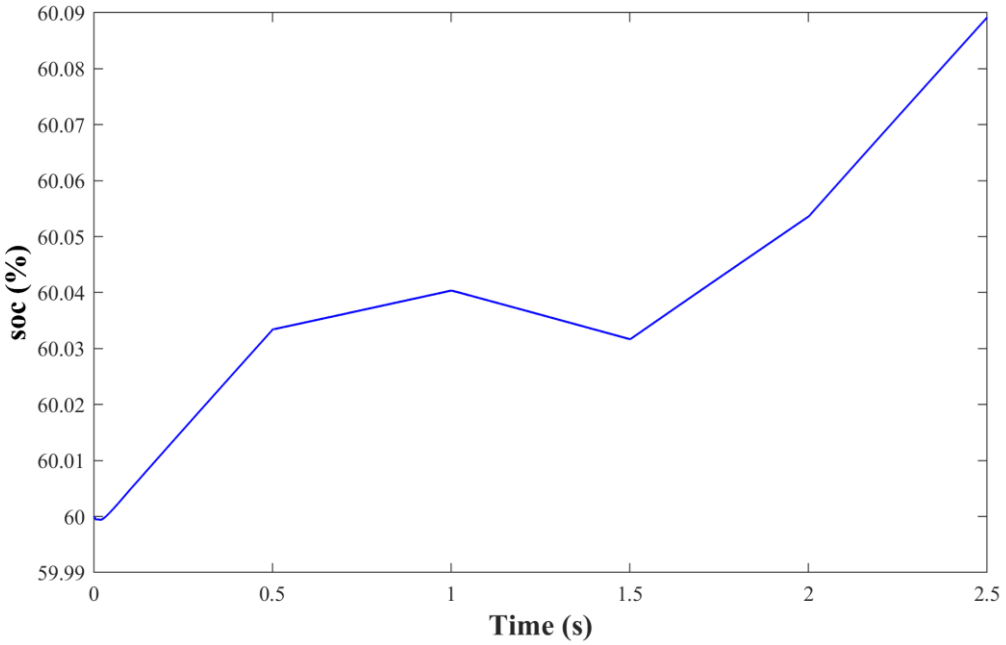

Fig.IV.7: *State of charge (soc(%)) of the systeme under solar iradiation changes control by super twisting.*

Figure(IV.7) illustrates State of charge (soc(%)) of the systeme under solar iradiation changes control by super twisting. In this case the state of charge is following the power balance in our system Which occurs due to changes of the solar iradiation $(P_{Load} = cte)$; when $P_{Load} < P_{pv}$ (the battery was in charge mod), and when $P_{Load} > P_{pv}$ (the battery was in discharge mod); becouse the battery compensates the lack of power Which creates when $P_{Load} >< P_{pv}$.

This case study highlights the effectiveness of the super-twisting algorithm when applied as a control control, showing clear advantages over the traditional PI regulator.

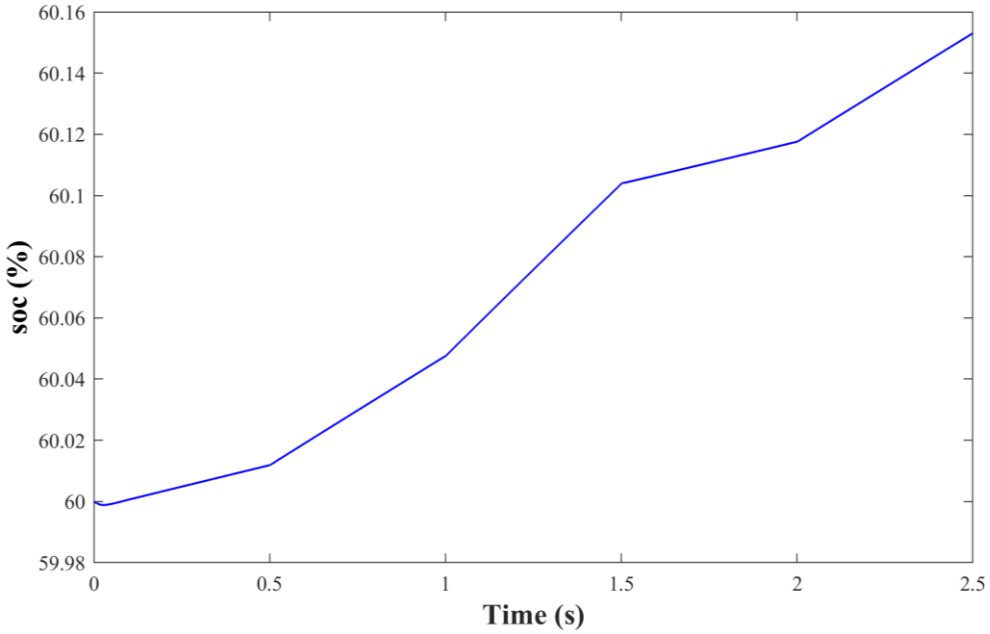

Fig.IV.8: *State of charge (soc(%)) of the systeme under PV cell temperature changes control by super twisting.*

Figure(IV.8) illustrates State of charge (soc(%)) of the systeme under PV cell temperature changes control by super twisting. In this case the state of charge is following the power balance in our system Which occurs due to changes of the PV cell temperature $(P_{Load} = cte)$; when $P_{Load} < P_{pv}$ (the battery was in charge mod), and when $P_{Load} > P_{pv}$ (the battery was in discharge mod); becouse the battery compensates the lack of power which creates when $P_{Load} >< P_{pv}$.

Upon analyzing the system's performance under both control strategies, it becomes clear that the super-twisting control significantly enhances system behavior compared to PI regulation.

IV.4.Conclusion

In conclusion, this chapter provided an overview of the sliding mode control approach and focused on applying the super twisting algorithm to control the photovoltaic (PV) and battery-based DC microgrid system. The primary goal was to leverage the advantages of the super twisting technique to enhance the control of key variables within the system, such as the PV output voltage, input boost converter current, DC voltage, and battery current. By utilizing this method, we were able to ensure the stable

operation of the system, maintaining currents, voltages, and power levels within desired ranges.

The application of the super twisting method, compared to the previously used PI regulators, significantly improved the performance of the system. Furthermore, monitoring the State of Charge (SOC%) of the energy storage system allowed for a more precise assessment of the remaining available energy, ensuring optimal operation throughout the simulation. The results demonstrated the effectiveness of the super twisting method in enhancing the overall control and performance of the PV and battery-based DC microgrid system.

General Conclusion

This research explored the control of a photovoltaic-based hybrid energy storage system integrated into a DC microgrid, with a primary focus on voltage stabilisation and disturbance rejection. Accurate modeling of both the PV system and the battery was carried out, forming the foundation for control development and performance analysis.

The implementation of a Proportional-Integral (PI) controller offered a baseline for assessing system performance. While the PI controller provided acceptable results under steady conditions, it exhibited limitations in handling dynamic disturbances and rapidly changing operating scenarios. This aligns with conclusions found in the literature where PI controllers often underperform under non-linear or time-varying conditions.

To address these shortcomings, a super-twisting sliding mode control technique was introduced. The super-twisting algorithm, based on higher-order sliding mode theory, is known for its ability to reduce chattering while maintaining robustness against uncertainties and disturbances.

The comparative analysis demonstrated that super-twisting control significantly improved voltage regulation and enhanced the system's robustness to disturbances and load variations. This advanced method allowed the hybrid energy storage system to respond more quickly and effectively to non-linear changes in the microgrid, ensuring stable and reliable operation.

In conclusion, the research highlights the critical importance of combining accurate system modeling with robust control strategies to manage renewable energy sources in DC microgrids. The findings support the use of advanced control techniques like super-twisting control to enhance system resilience and stability, paving the way for more reliable renewable energy integration. Future work could include real-time implementation, hardware-in-the-loop testing, and the inclusion of other renewable energy sources such as wind turbines or supercapacitors.

Bibliography :

[1] Lasseter, R. H. (2002). Microgrids. IEEE Power Engineering Society Winter Meeting, 1, 305–308.

[2] Dragicevic, T., Lu, X., Vasquez, J. C., & Guerrero, J. M. (2016). DC microgrids–Part I: A review of control strategies and stabilization techniques. IEEE Transactions on Power Electronics, 31(7), 4876–4891.

[3] Olivares, D. E., Mehrizi-Sani, A., Etemadi, A. H., et al. (2014). Trends in microgrid control. IEEE Transactions on Smart Grid, 5(4), 1905–1919.

[4] Yann Pankow, "Etude de l'intégration de la production décentralisée dans un réseau basse tension. Application au générateur photovoltaïque," Thèse de Doctorat de l'Ecole Nationale Supérieure d'Arts et Métiers, Paris, 2004.

[5] Messaoudi Salah et Gouga Adel, "Étude comparative de quelques techniques de poursuite du point de puissance maximale d'un générateur photovoltaïque," Mémoire d'Ingéniorat de l'Université Mohamed Khider de Biskra, 2007.

[6] http://www.cipcsp.com/tutorial, Dernier accès : 22/ 06/2011.

[7] Makhebi Charaf-Eddine et Toumert Mhand,"Etude et réalisation d'un régulateur analogique et numérique de la charge/décharge d'une batterie associée à un système photovoltaïque," Mémoire d'Ingéniorat de l'école Nationale Polytechnique d'Alger, 2008.

[8] Sébastien Quoizola, "Épitaxie en phase vapeur silicium sur silicium sur mesoporeux pour report sur substrats économiques et application photovoltaïque bas coût," Thèse de Doctorat, de l'Institute National des Sciences Appliquées de Lyon, 2003.

[9] AkihKiro Oi,"Design and simulation of photovoltaic water pumping system," Thèse de Master de l'Université de California, Septembre 2005.

[10] Bellala Djamel, "Contribution à l'optimisation des systèmes de conversion d'énergie. Application aux systèmes photovoltaïques," Thèse Doctorat de l'Université de Batna, 2009.

[11] F. Adamo, F. Attivissimo, A. Di Nisio, A. M. L. Lanzolla and M. Spadavecchia, "Parameters estimation for a model of photovoltaic panels," XIX IMEKO World Congress, September, Lisbon, Portugal , 2009.

[12] Angel Cid Pastor,"Conception et réalisation de modules photovoltaïques électroniques," Thèse de Doctorat de l'Institut National des Sciences Appliquées de Toulouse, Septembre 2006.

[13] V. Di Dio, D. La Cascia, R. Miceli and C. Rando, "A mathematical model to determine the electrical energy production in photovoltaic fields under mismatch effect," IEEE-ICCEP 2009 International Conference on Clean Electrical Power, Capri, Italia, pp. 46-51.

[14] Chen-Chi Chu and Chieh-Li Chen, "Robust maximum power point tracking method for photovoltaic cells: A sliding mode control approach," Solar Energy, Vol. 83, No 8, August 2009, pp. 1370-1378.

[15] Azadeh Safari and Saad Mekhilef, "Simulation and hardware implementation of incremental conductance MPPT with direct control method using cuk converter," IEEE Transaction on Industrial Electronics, Vol. 58, No. 4, April 2011, pp. 1154-1161.

[16] Mohamed Djerlah, "Contribution à l'étude des systèmes photovoltaïques résidentiels couples au réseau électrique," Thèse de Doctorat de l'Université de Batna, 2008.

[17] Abdessalem Titraoui, Ahmed Sahroui et Mohamed Nadir, "Etude d'une chaine de conversion photovoltaïque," Mémoire d'Ingéniorat de l'Université de M'sila, 2010.

[18] Maria Carmela Di Piazza, Antonella Ragusa, Massimiliano Luna and Gianpaolo Vitale, "A dynamic model of a photovoltaic generator based on experimental data," International Conference on Renewable Energies and Power Quality, Granada, Spain, March 2010.

[19] Corinne Alonso, "Contribution à l'optimisation, la gestion et le traitement de l'énergie," Thèse Doctorat de l'Université de Paul Sabatier, Toulouse III, 2003.

[20] Mohamed Lakhdar Louazenen, "Etude technico-économique d'un système de pompage photovoltaïque sur le site de Ouargla, Mémoire de Magister de Université de Batna, 2008.

[21] Ahmed Hessien, kotaro, Hirasawa, jinglu Hu and junichi Murat, "The dynamic performance of photovoltaic supplied DC motor Fed from DC-DC converter and controller by neuronal network," International Joint Conference, Vol. 1, No. 2, Août 2002, pp. 607- 612.

[22] Anca Hansen, Poul Sørensen, Lars Hansen and Henrik Bindner, "Models for a stand-alone PV System,"Rapport de Ris National Laboratory, Denmark, 2000.

[23] S. Carbonell Daura, "Energy Management of a Fuel Cell plus Battery Powertrain," Master Thesis, Universitat Politècnica de Catalunya, 2021.

[24] D. Linden and T. B. Reddy, "Handbook of Batteries 3 Ed. Amerika Serikat: The McGraw- Hills Companies," Ed: Inc, 2002.

[25] P. Thounthong, "Control of Hybrid Renewable Energy Power Plant for Autonomous Systems," Phd Thesis, Université de Lorraine, 2020.

[26] A. M. O. Haruni, "A Stand-Alone Hybrid Power System with Energy Storage," Phd Thesis, University of Tasmania, 2013.

[27] J. Alzieu and J. Robert, "Accumulateurs au Lithium," Techniques de l'Ingénieur Accumulateurs d'Energie, 2005.

[28] K. Xu, "Nonaqueous Liquid Electrolytes for Lithium-Based Rechargeable Batteries," Chemical Reviews, vol. 104, no. 10, pp. 4303-4418, 2004.

[29] C. J. Orendorff, "The role of Separators in Lithium-ion Cell Safety," The Electrochemical society interface, vol. 21, no. 2, pp. 61-65, 2012.

[30] G. Fisher, "Pouch, Cylindrical or Prismatic: Which Battery Format Will Rule the Market," Addionics, London, UK, 14th April, 2021.

[31] D. Li, D. L. Danilov, H. J. Bergveld, R.-A. Eichel, and P. H. Notten, "Understanding Battery Aging Mechanisms," in book section of Future Lithium-Ion batteries, pp. 220-250, 2019.

[32] F. Seydali, "Contribution à l'Optimisation de la Gestion de l'Energie d'un Micro-réseau Continu," Thèse de Doctorat, Université de M'sila, 2022.

[33] A. Salamani, "Synthèse et Caractérisation de Nouveaux Matériaux de Cathode pour Générateurs Electrochimiques," Thèse de Doctorat, Université de M'sila, 2018.

[34] M. Sellali, "Commande d'un Système Multi-Sources Dédié au Véhicule Électrique," Thèse de doctorat, Université Mohamed Khider, Biskra, 2020.

[35] D. W. Gao, Energy storage for sustainable microgrid. Academic Press, 2015.

[36] R. Yazami and P. Touzain, "A Reversible Graphite-Lithium Negative Electrode for Electrochemical Generators," Journal of Power Sources, vol. 9, no. 3, pp. 365-371, 1983.

[37] L. Qian et al., "Electrochemical Synthesis of Mesoporous FePO4 Nanoparticles for Fabricating High Performance LiFePO4/C Cathode Materials," Microporous and Mesoporous Materials, vol. 152, pp. 128-133, 2012.

[38] K. Persson, V. A. Sethuraman, L. J. Hardwick, Y. Hinuma, Y. S. Meng, A. van der Ven, V. Srinivasan, R. Kostecki and G. Ceder, J. Phys. Chem. "Graphite anode",2010. Available online: https://www.chemtube3d.com/lib_graphite-2 (accessed 16 Mai, 2023).

[39] J. Asenbauer, T. Eisenmann, M. Kuenzel, A. Kazzazi, Z. Chen, and D. Bresser, "The Success Story of Graphite as a Lithium-Ion Anode Material–Fundamentals, Remaining Challenges, and Recent Developments Including Silicon (Oxide) Composites," Sustainable Energy & Fuels, vol. 4, no. 11, pp. 5387-5416, 2020.

[40] A. Manthiram and J. B. Goodenough, "Layered Lithium Cobalt Oxide Cathodes," Nature Energy, vol. 6, no. 3, pp. 323-323, 2021.

[41] C. K. Dyer, P. T. Moseley, Z. Ogumi, D. A. Rand, and B. Scrosati, Encyclopedia of Electrochemical Power Sources. Elsevier Science & Technology, 2009.

[42] H.-G. Steinrück et al., "The Nanoscale Structure of the Electrolyte–Metal Oxide Interface," Energy & Environmental Science, vol. 11, no. 3, pp. 594-602, 2018.

[43] R. Andersson, O. Borodin, and P. Johansson, "Dynamic Structure Discovery Applied to the Ion Transport in the Ubiquitous Lithium-ion Battery Electrolyte LP30," Journal of the Electrochemical Society, vol. 169, no. 10, pp. 1-10, 2022.

[44] S. S. Zhang, "A Review on the Separators of Liquid Electrolyte Li-Ion Batteries," Journal of Power Sources, vol. 164, no. 1, pp. 351-364, 2007.

[45] "Global and China Lithium Battery Electrolyte Industry Report", Available online: https://industry-research-reports.blogspot.com/2015/01/research-announces-global-and-china.html?spref=pi (accessed 31 Mai, 2023).

[46] A. Lipschultz, "Batteries in a Portable World," Biomedical Instrumentation & Technology, vol. 49, no. 2, pp. 134-134, 2015.

[47] D. Rekioua and E. Matagne, Optimization of Photovoltaic Power Systems: Modelling, Simulation and Control. Springer Science & Business Media, 2012.

[48] A. El Kharouf, N. Rees, and R. Steinberger Wilckens, "Gas Diffusion Layer Materials and Their Effect on Polymer Electrolyte Fuel Cell Performance–Ex Situ and in Situ Characterization," Fuel Cells, vol. 14, no. 5, pp. 735-741, 2014.

[49] C. Zhu, X. Li, L. Song, and L. Xiang, "Development of a Theoretically Based Thermal Model for Lithium Ion Battery Pack," Journal of Power Sources, vol. 223, pp. 155-164, 2013.

[50] R. E. Giachetti, C. J. Peterson, D. L. Van Bossuyt, and G. W. Parker, "Systems Engineering Issues in Microgrids for Military Installations," in conference proceedings of INCOSE International Symposium, 2020, vol. 30, no. 1, pp. 731-746. Location, Naval Postgraduate School.

[51] V. Benamara, "Etude et Simulation d'un Panneau Solaire Raccorde au Réseau avec Peripherique De Stockage," Thèse de Doctorat, École de Technologie Supérieure, UNIVERSITÉ DU QUÉBEC, 2012.

[52] Hassaine, L., Olivier, S., & Benhadj, A. (2014). Maximum power point tracking algorithms for photovoltaic applications. Renewable and Sustainable Energy Reviews, 19, 39–50.

[53] Elgendy, M.A., Zahawi, B., & Atkinson, D.J. (2013). Assessment of the Incremental Conductance Maximum Power Point Tracking Algorithm. IEEE Transactions on Sustainable Energy, 4(1), 108–117.

[54] Femia, N., Petrone, G., Spagnuolo, G., & Vitelli, M. (2005). Optimization of perturb and observe maximum power point tracking method. IEEE Transactions on Power Electronics, 20(4), 963–973.

[55] Kanchan, R., & Pandey, A. (2018). Design and Implementation of PI Controller in PV Based System with Battery Storage. International Journal of Engineering Research & Technology (IJERT), 7.(6)

[56] C. Wu, C. Zhu, Y. Ge, and Y. Zhao, "A Review on Fault Mechanism and Diagnosis Approach for Li-Ion Batteries," Journal of Nanomaterials, vol. 2015, pp. 8-8, 2015.

[57] N. Tudoroiu, "Battery Management Systems of Electric and Hybrid Electric Vehicles". MDPI-Multidisciplinary Digital Publishing Institute, 2021.

[58] S. Njoya Motapon, "Design and Simulation of a Fuel Cell Hybrid Emergency Power System for a More Electric Aircraft: Evaluation of Energy Management Schemes," PHD Thesis, École de Technologie Supérieure. Location, UNIVERSITÉ DU QUÉBEC ,2013.

[59] C. Wang, Modeling and Control of Hybrid Wind/Photovoltaic/Fuel Cell Distributed Generation Systems. Phd Thesis, Montana State University, 2006.

[60] K. W. Suh, Modeling, Analysis and Control of Fuel Cell Hybrid Power Systems. Phd Thesis, University of Michigan, 2006.

[61] H. Taheri Ledari, "Robust Adaptive Nonlinear Control of Microgrid Frequency and Voltage in The Presence of Renewable Energy Sources," Doctoral Thesis, École de Technologie Supérieure, UNIVERSITÉ DU QUÉBEC,2017.

[62] M. Rezkallah, "Design and control of standalone and hybrid standalone power generation systems," Doctoral thesis, École de technologie supérieure, 2016.

[63] R. L. Gour, "Small Signal Modelling of a Buck Converter using State Space Averaging for Magnet Load," vol, vol. 3, pp. 11-17.

[64] S. C. Erensoy, "Simulation and Energy Management Strategy Development for a Fuel Cell Hybrid Electric Powertrain of a Zero-Emission Boat", Master's Thesis, Instituto Superior Técnico,2018.

[65] M. Hassan and A. A. Elbaset, "Small-Signal Matlab/Simulink Model of DC-DC Buck Converter Using State-Space Averaging Method," 17th International Middle-East Power System Conferennce (MEPCON'15), 2015.

[66] 1- Ma Lu, S. "Modelling, Control and Simulation of a Microgrid based on PV System, Battery System and VSC" , Bachelor's thesis, Universitat Politècnica de Catalunya, 2018.

[67] A. Zorig, "Commandes Non Linéaires d'une Source Décentralisée Photovoltaïque à Base de Convertisseurs de Puissance Entrelacés et Parallèles," Thèse de Doctorat, Université Amar Telidji, Laghouat, 2017.

[68] V. I. Utkin, "Sliding Mode Control Design Principles and Applications to Electric Drives," IEEE Transactions on Industrial Electronics,vol. 40, no. 1, pp. 23–36, 1993.

[69] S. V. Drakunovand V. I. Utkin, ,Sliding Mode Control in Dynamic Systems,' International Journal of Control, vol. 55, no. 4, pp. 1029–1037, 1992.

[70] S. Bouafia, ,Commandes non Linéaire d'un Système VSC-HVDC Multiniveaux à Configuration Back-To-Back,' Mémoire de Magister, Université DjillaliLiabes,Sidi-Bel-Abbes, 2013.

[71] B. E. Youcefa, ,Etude de L'association d'un Filtre Actif Parallèle à des Sources d'énergie Renouvelables,' Thèse Doctorat, UniversiteDjillaliLiabes,Sidi-Bel-Abbes, 2020.

[72] H. Lee and V.I. Utkin,,Chattering Suppression Methods in Sliding Mode Control Systems,'Annual Reviews In Control, vol. 31, no. 2, pp. 179–188, 2007.

[73] K. D. Young and Ü. Özgüner, ''Variable Structure Systems, Sliding Mode And Nonlinear Control,''Springer, 2007.

[74] J.J.E. Slotine and W. Li,,Applied Nonlinear Control,' Prentice Hall Englewood Cliffs, NJ, USA, 1991.

[75] N.K Sharma and J. Sivaramakrishnan, ''Discrete-Time Higher Order Sliding Mode,''Springer, India, 2018.

[76] S. Bouafia, A. Benaissa, M. Bouzidi, and S. Barkat, ,Sliding Mode Control of Three Levels Back-to-Back VSC-HVDC System Using Space Vector Modulation,' International Journal of Power Electronics and Drive System (IJPEDS), vol. 4, no. 2, pp. 265–273, June 2014.

[77] I. Eker And Ş. A. Akinal, "Sliding Mode Control With Integral Augmented Sliding Surface: Design and Experimental Application to an Electromechanical System," Electrical Engineering, vol. 90, pp. 189–197, 2008.

[78] A. Levant, ‚Sliding Order and Sliding Accuracy in Sliding Mode Control,' Int. J. Control, vol. 58, no. 6, pp. 1247–1263, Dec. 1993.

[79] A. Levant, ‚Higher-Order Sliding Modes, Differentiation and Output-Feedback Control,' Int. J. Control, vol. 76, no. 9–10, pp. 924–941, Jan. 2003.

[80] A. Levant, ‚Principles of 2-Sliding Mode Design,' Automatica, vol. 43, no. 4, pp. 576–586,

Apr. 2007.

[81] Y. Shtessel, C. Edwards, L. Fridman, and A. Levant, ‚Sliding Mode Control And Observation,' New York, Ny, Springer, New York, 2014.

[82] G. Bartolini, A. Pisano, E. Punta, and E. Usai, ‚A Survey of Applications of Second-Order Sliding Mode Control to Mechanical Systems,' Int. J. Control, vol. 76, no. 9–10, pp. 875– 892, Jan. 2003.

[83] J. A. Moreno and M. Osorio, "A Lyapunov Approach to Second-Order Sliding Mode Controllers and Observers," 2008 47th IEEE Conference on Decision and Control, Cancun, 2008.

[84] M. Cheng, W. Su, V. Radisavljevic-Gajic, and Ü. Özguner, "A Lyapunov Approach to Second-Order Sliding-Mode Boundary Control of an Unstable Heat System With Spatiotemporal-Varying Parameters Under Boundary Disturbances," American Control Conference, Portland, 2014.

[85] Mahmoud, M. S., & El-Saadany, E. F. (2018). Advanced control strategies for DC microgrids: A comprehensive review. Electric Power Systems Research, 157, 221–231.

[86] Levant, A. (2003). Higher-order sliding modes, differentiation and output-feedback control. International Journal of Control, 76(9-10), 924–941.

[87] Bidram, A., Davoudi, A., Lewis, F. L., & Qu, Z. (2013). Secondary control of microgrids based on distributed cooperative control of multi-agent systems. IET Generation, Transmission & Distribution, 7(8), 822–831.